

Syracuse University

**SURFACE**

---

Dissertations - ALL

SURFACE

---

December 2014

## Lacustrine Turbidites from Tropical African Lakes as Indicators of Hydrologic and Climatic Changes

Xuewei Zhang  
*Syracuse University*

Follow this and additional works at: <https://surface.syr.edu/etd>



Part of the [Physical Sciences and Mathematics Commons](#)

---

### Recommended Citation

Zhang, Xuewei, "Lacustrine Turbidites from Tropical African Lakes as Indicators of Hydrologic and Climatic Changes" (2014). *Dissertations - ALL*. 182.

<https://surface.syr.edu/etd/182>

This Dissertation is brought to you for free and open access by the SURFACE at SURFACE. It has been accepted for inclusion in Dissertations - ALL by an authorized administrator of SURFACE. For more information, please contact [surface@syr.edu](mailto:surface@syr.edu).

## **Abstract**

Flood-sourced turbidites (i.e. hyperpycnites) preserved in lake basins are proven indicators of hydrologic changes, yet their usefulness as recorders of tropical paleoclimate variability has long been overlooked. The primary focus of this dissertation research is to investigate the late Quaternary hydroclimatic changes in tropical Africa, using hyperpycnites, dated sediment cores, and high-resolution seismic reflection profiles from Lake Kivu in the East African Rift and Lake Bosumtwi in equatorial West Africa. A secondary focus of this dissertation is to image ancient turbidite systems of the Lake Albert rift in East Africa, using 2-D and 3-D seismic reflection data, and to assess the structural controls on turbidite sedimentation.

Reoccurring megaturbidites (covering  $>200 \text{ km}^2$ ) over the past  $\sim 12 \text{ k.y.}$  were revealed by integrating seismic reflection data and sediment core results from Lake Kivu, which is subject to potential limnic overturns and degassing events. Sedimentological evidence and seismic and lake-floor bathymetric data suggest that the turbidites were sourced by hyperpycnal river flows during exceptional floods. Time series of turbidite bed-thickness and accumulation rate were generated and compared with regional paleohydrologic records of tropical East Africa, and it is found that the temporal occurrence of the turbidites is climatically controlled. It is also suggested that extreme floods in Lake Kivu's recent history may have triggered deep mixing events, and that potential geologic hazards associated with extraordinary turbidity currents may pose a risk to the current gas-extraction efforts in the lake.

To further evaluate the effectiveness of lacustrine hyperpycnites as indicators of tropical African hydroclimatic changes, a 65 k.y. record of extreme hydrologic events in equatorial West Africa was reconstructed, using flood-sourced turbidites, seismic and sedimentological lake-level indicators, and paleohydrologic proxies, including total organic carbon and carbon isotopes, from the Lake Bosumtwi impact crater. Peak turbidite sedimentation is found to correlate with intervals of high TOC and markedly negative  $\delta^{13}\text{C}$  values, suggesting that the turbidites were deposited during periods of high lake-levels. The multi-proxy paleohydrologic record from Lake Bosumtwi suggests that over the past 65 k.y., millennial-scale variability of hydrologic extremes in equatorial West Africa was linked to North Atlantic climate, with exceptional rainfall events linked to Dansgaard–Oeschger interstadials and megadrought events associated with slowdowns of the North Atlantic Meridional Overturning circulation during Heinrich stadials.

Finally, 2-D and 3-D seismic reflection data from the Lake Albert Rift were analyzed to assess turbidite sedimentology in tectonically active rift lakes. Large channelized turbidite systems were observed and characterized in 3-D seismic data using seismic attribute analyses. In the absence of sediment failures and related mass transport deposits from the seismic record, it is postulated that the turbidites were sourced by hyperpycnal river flows during floods, and that there was a change in the sediment source of the turbidites, caused by drainage reversals due to rift shoulder uplift. Sediment dispersal pathways, changes in depositional facies, and evolution of the sublacustrine turbidite systems are largely controlled by syndepositional tectonism in that system.

**Lacustrine Turbidites from Tropical African Lakes as Indicators of  
Hydrologic and Climatic Changes**

by

Xuewei Zhang

M.S., 2006, China University of Geosciences (Beijing), China

B.S., 2003, Northeast Petroleum University, China

DISSERTATION

Submitted in partial fulfillment of the requirements for the degree of Doctor of  
Philosophy in Earth Sciences

Syracuse University

December 2014

Copyright © Xuewei Zhang 2014  
All Rights Reserved

## **Acknowledgments**

This research was funded by the industrial associates of the Syracuse University Lacustrine Rift Basin Research Program and MacArthur Foundation. Funding for the collection of drill cores from Lake Bosumtwi was provided by the U.S. National Science Foundation (NSF) and the International Continental Scientific Drilling Program (ICDP). Seismic data analysis was completed using Landmark Graphics software provided to Syracuse University through the Landmark Graphics University Partnership Program.

Without the support and guidance of Christopher Scholz, my advisor, this work could not have been accomplished. I also thank Bruce Wilkinson, Timothy Shanahan, Peng Gao, and Gregory Hoke, members of my dissertation committee, for their guidance and review of drafts of my writing. I am grateful to our collaborators of this research, including Robert Hecky, Cynthia Ebinger, Nickolas McKay, and many others, for sharing of ideas and data. Peter Cattaneo, Jaqueline Corbett, and the rest members of Lacustrine Rift Basin research group are thanked for their contributions to the field and lab work. I am truly thankful to my family, my girlfriend, Ludi Cui, friends, and the entire Department of Earth Sciences community for their support through this challenging yet rewarding process.

## Table of Contents

<b>Abstract</b> .....	i
<b>Acknowledgements</b> .....	v
<b>Table of Contents</b> .....	vi
<b>List of Figures</b> .....	viii
<b>List of Tables</b> .....	x
<b>Preface</b> .....	xi

### CHAPTER 1:

<b>Climatic control of the late Quaternary turbidite sedimentology of Lake Kivu, East Africa: Implications for deep mixing and geologic hazards</b> .....	1
Abstract .....	2
Introduction and Geologic Setting .....	3
Data and Methods .....	5
Geochronology .....	5
Turbidite Systems .....	6
Discussion .....	7
<i>Source of Turbidite Currents</i> .....	7
<i>Climatic Control of Hyperpycnite Events</i> .....	8
<i>Implications for Deep Mixing and Geologic Hazards</i> .....	11
Acknowledgements .....	12
References Cited .....	13
Figures .....	17
Supplementary Figures .....	21
Supplementary Tables .....	30
Supplementary References .....	38

### CHAPTER 2:

<b>Millennial-scale extreme hydrologic events in equatorial West Africa linked to North Atlantic climate</b> .....	39
Abstract .....	40
Introduction .....	41
Background to Lake Bosumtwi .....	41
Paleohydrologic Proxies for Reconstruction of Exceptional Floods and Droughts .....	43
Turbidites and Source of Turbidity Flows .....	45
Exceptional Rainfall Events .....	47
Exceptional Drought Events .....	49
North Atlantic Forcing of West African Hydroclimate .....	50

Implications for Future Research .....	52
Methods .....	53
<i>Layer Identification, Time series, and Particle Size of Turbidites</i> .....	53
<i>TOC and Carbon Isotopes</i> .....	54
Acknowledgements .....	55
References .....	56
Figures .....	63
Supplementary Figures .....	67
Supplementary Tables .....	75
Supplementary References .....	86
<b>CHAPTER 3:</b>	
<b>Sublacustrine turbidite systems of the Lake Albert Rift, East Africa, from seismic reflection data</b> .....	87
Abstract .....	88
Introduction .....	89
Geological Setting .....	90
Datasets and Methodology .....	92
Results .....	93
<i>Intrabasinal Faults Observed in The Semliki 3-D Seismic Survey</i> .....	93
<i>Turbidite Systems</i> .....	94
Discussion .....	97
<i>Meander Geometry</i> .....	97
<i>Sediment Sources</i> .....	98
<i>Structural Control of Turbidite Sedimentation</i> .....	101
Conclusions .....	103
Acknowledgements .....	104
References .....	105
Figures .....	115
Tables.....	136
<b>Biographical Data</b> .....	137



## List of Figures

### CHAPTER 1:

<b>Figure 1.</b> Regional topography and structural framework of the Lake Kivu rift .....	17
<b>Figure 2.</b> Turbidite systems revealed by seismic and sediment core data .....	18
<b>Figure 3.</b> Correlation of sediment cores 12-19A, 12-16B, and 12-15A .....	19
<b>Figure 4.</b> Correlation of Lake Kivu records with regional paleohydrologic records .....	20
<b>Supplementary Figure 1.</b> Basemap of Lake Kivu .....	21
<b>Supplementary Figure 2.</b> Age model of sediment core 12-19A .....	22
<b>Supplementary Figure 3.</b> An example of core-to-core correlation over 30 km .....	23
<b>Supplementary Figure 4.</b> A seismic profile showing the development of turbidites .....	24
<b>Supplementary Figure 5.</b> Rip-up clasts in turbidite channel and lobe deposits .....	25
<b>Supplementary Figure 6.</b> Sediment texture and composition of turbidites and diatomites .....	26
<b>Supplementary Figure 7.</b> An air gun seismic profile showing the -380 m lowstand .....	27
<b>Supplementary Figure 8.</b> Transition from deltaic and ooid facies to laminated mud facies .....	28
<b>Supplementary Figure 9.</b> Correlation between sediment cores 12-16B and 13-11A .....	29

### CHAPTER 2:

<b>Figure 1.</b> Map of the Lake Bosumtwi impact crater .....	63
<b>Figure 2.</b> Correlation of L. Bosumtwi paleoclimatic records with the North Atlantic records .....	64
<b>Figure 3.</b> Megadroughts and lake-level lowstands revealed by seismic unconformities .....	65
<b>Figure 4.</b> Correlation of $\delta^{13}\text{C}$ records between cores BOS04-5B and GeoB7920-2 .....	66
<b>Supplementary Figure 1.</b> January and July monthly mean precipitation .....	67
<b>Supplementary Figure 2.</b> Turbidites–CHIRP seismic data correlation .....	68
<b>Supplementary Figure 3.</b> Thickness versus frequency of the past 65 k.y. turbidite events .....	69
<b>Supplementary Figure 4.</b> An example of turbidite identification .....	70
<b>Supplementary Figure 5:</b> Smear-slide photomicrographs of the light-gray turbidite caps .....	71
<b>Supplementary Figure 6.</b> Smear-slide photomicrographs of thick turbidite sediments .....	72

<b>Supplementary Figure 7.</b> Turbidite grain size profiles and distributions .....	73
<b>Supplementary Figure 8.</b> Possible insolation forcing of turbidite accumulation rate .....	74

**CHAPTER 3:**

<b>Figure 1.</b> Regional topography, structural framework, and drainage systems .....	115
<b>Figure 2.</b> The asymmetric full-graben structure of the Lake Albert rift .....	116
<b>Figure 3.</b> Major intrabasinal faults and inferred stratigraphic boundaries .....	117
<b>Figure 4.</b> Generalized stratigraphy of the Lake Albert rift .....	118
<b>Figure 5.</b> Isochron of the interval between the ‘Green’ and ‘Purple’ seismic surfaces .....	119
<b>Figure 6.</b> Seismic attributes extracted on the ‘Green’ seismic surface .....	122
<b>Figure 7.</b> Distribution of turbidite systems of the ‘Green’ unit .....	123
<b>Figure 8.</b> A seismic profile showing turbidite channels of the ‘Green’ unit .....	124
<b>Figure 9.</b> Seismic attributes extracted on the ‘Purple’ seismic surface .....	127
<b>Figure 10.</b> Distribution of turbidite systems of the ‘Purple’ unit .....	128
<b>Figure 11.</b> Seismic profiles showing turbidite channels of the ‘Purple’ unit .....	129
<b>Figure 12.</b> Sublacustrine fans deposited along the N. Toro Bunyoro Fault .....	130
<b>Figure 13.</b> Quantitative meander geometry of the sublacustrine turbidite channels .....	131
<b>Figure 14.</b> Correlation between the turbidite systems and onshore drainage basins .....	133
<b>Figure 15.</b> Visualization of the ‘Green’ and ‘Purple’ seismic surfaces .....	135

## List of Tables

### CHAPTER 1:

<b>Supplementary Table 1.</b> Accelerator Mass Spectrometry $^{14}\text{C}$ ages .....	30
<b>Supplementary Table 2.</b> Metadata of sediment cores .....	31
<b>Supplementary Table 3.</b> Turbidites observed in cores 12-19A, 12-16B, and 12-15A .....	32
<b>Supplementary Table 4.</b> Total inorganic carbon (TIC) record of core 13-12C .....	35

### CHAPTER 2:

<b>Supplementary Table 1.</b> Turbidites observed in core BOS04-5B .....	75
<b>Supplementary Table 2.</b> TOC and $\delta^{13}\text{C}$ data of core BOS04-5B .....	83

### CHAPTER 3:

<b>Table 1.</b> Empirically derived relationships of river meanders .....	136
---------------------------------------------------------------------------	-----

## Preface

Knowledge of long-term variations of floods and droughts in tropical Africa is of ecological, political, and socioeconomic importance, and is essential for understanding the effects of climate change on evolution and migration of prehistoric humans within and out of the Africa continent. Previous studies have established chronologies of extreme hydrologic events using records of flood-sourced turbidites from mid- and high-latitude lakes. However, lacustrine turbidites as recorders of tropical paleoclimate variability have long been overlooked. Turbidites comprise a large fraction of the sediment volume of lacustrine rift basins, yet, compared to submarine turbidite systems on passive continental margins, turbidite systems from tectonically active, lacustrine rift basins are underexplored.

This research was designed to explore the usefulness of lacustrine turbidites as indicators hydroclimatic changes in tropical Africa, and to advance understanding of turbidite sedimentology in lacustrine rift basins. This dissertation is divided into three chapters.

**Chapter 1** assesses the climatic control of late Quaternary turbidite sedimentology of Lake Kivu and the potential consequences of extraordinary turbidity currents, which may have triggered deep mixing events in Kivu's recent history, and which pose a risk to the current degassing efforts in the lake. This chapter was published as:

*Zhang, X., Scholz, C. A., Hecky, R. E., Wood, D. A., Zal, H. J., and Ebinger, C. J., 2014, Climatic control of the Late Quaternary turbidite sedimentology of Lake Kivu, East Africa: Implications for deep mixing and geologic hazards: Geology, v. 42, p. 811-814.*

**Chapter 2** further assesses the effectiveness of lacustrine turbidites for reconstruction of hydrologic and climatic changes in tropical Africa. For the first time, a record of exceptional floods and droughts in equatorial West Africa (over the past 65 k.y.) was generated, using lacustrine turbidites, total organic carbon, carbon isotopes, and high-resolution seismic reflection data from the Lake Bosumtwi impact crater. Chapter 2 provides new insight into the dynamics of the West African Monsoon system, and the teleconnection between northern high-latitude climate instability and millennial-scale hydrological extremes in equatorial West Africa. This chapter is to be submitted as:

*Zhang, X., Scholz, C. A., Mckay, N. P., Shanahan, T. M., Heil, C. W., Overpeck, J. T., King, J., and Peck, J., Millennial-scale extreme hydrologic events in equatorial West Africa linked to North Atlantic climate: Nature.*

Using commercially acquired 2-D and 3-D seismic reflection data, **Chapter 3** seeks to make quantitative comparisons of the planform morphology between sublacustrine turbidite and subaerial fluvial systems, and to determine the source of turbidity currents and the structural control of turbidite sedimentology in the Lake Albert rift. This chapter is currently in review as:

*Zhang, X. and Scholz, C. A, Sublacustrine turbidite systems of the Lake Albert Rift, East Africa, from seismic reflection data: Sedimentary Geology.*

## **CHAPTER 1:**

### **Climatic control of the late Quaternary turbidite sedimentology of Lake Kivu, East Africa:**

#### **Implications for deep mixing and geologic hazards**

Xuewei Zhang<sup>1\*</sup>, Christopher A. Scholz<sup>1</sup>, Robert E. Hecky<sup>2</sup>, Douglas A. Wood<sup>1</sup>, Hubert J. Zal<sup>3</sup>,  
and Cynthia J. Ebinger<sup>3</sup>

<sup>1</sup>Department of Earth Sciences, Syracuse University, Syracuse, New York 13203, USA

<sup>2</sup>Large Lakes Observatory, University of Minnesota, Duluth, Minnesota 55812, USA

<sup>3</sup>Department of Earth and Environmental Sciences, University of Rochester, Rochester, New  
York 14627, USA

\*E-mail: xzhang39@syr.edu

## **Abstract**

The Lake Kivu catchment in the East African Rift is subject to various geologic hazards, including frequent volcanic eruptions, earthquakes, and potential limnic overturns and degassing events. Integration of high-resolution seismic reflection data, <sup>14</sup>C-dated sediment cores, and lake-floor bathymetry reveals large axial and transverse turbidite systems in the eastern basin of the lake. The turbidites were sourced by hyperpycnal river flows during exceptional floods, and the temporal occurrence of the turbidites was climatically controlled. The turbidite record over the past ~12 k.y. is correlated with the regional paleohydrologic records from tropical East Africa. Our study suggests that flood-introduced turbidites preserved in deep lakes are indicators of hydrological changes, and that extreme floods in Lake Kivu's recent history may have triggered deep mixing events. This study also has implications for the current degassing efforts in Lake Kivu; potential geologic hazards may be triggered by extraordinary turbidity currents, and need to be considered in the design and deployment of gas extraction facilities.

## **Introduction and Geological Setting**

Turbidity currents can be initiated by sediment failures on slopes; by pyroclastic flows during volcanic eruptions; and by hyperpycnal river flows during floods (Meiburg and Kneller, 2009). Because hyperpycnal flows are related to climate through flood frequency and magnitude, their deposits record climate changes (Mulder et al., 2001). Previous investigations have established chronologies of extreme hydrologic events using records of terrigenous inwash in mid- and high-latitude lakes (e.g. Noren et al., 2002; Schillereff, et al., 2014). However, flood-triggered hyperpycnal flow deposits (i.e. hyperpycnites) as indicators of hydrological changes in tropical Africa have long been overlooked. Lake Kivu in the East African Rift provides an excellent opportunity to study how climate influences the temporal occurrence of hyperpycnite sedimentation in tropical African lakes.

Situated on the Precambrian metamorphic basement, Lake Kivu (2°S, 29°E; Fig. 1) occupies an asymmetric half-graben, and is about 100 km long, 45 km wide, and 480 m deep. Extension and volcanism in the Kivu rift began in the middle to late Miocene (Ebinger, 1989). During the Pleistocene, eruptions of the Virunga volcanoes dammed the lake's northward outflow to Lake Edward, and the water accumulated in the rift valley to form the present Lake Kivu (Beadle, 1981). Modern Lake Kivu discharges south to Lake Tanganyika through the Ruzizi River, and is the major contributor to Lake Tanganyika's hydrological and solute budget (Stoffers and Hecky, 1978).



Volcanic and hydrothermal activity has greatly influenced the chemistry and stratification of the lake water, accounting for elevated solute concentrations (Degens and Kulbicki, 1973) and enrichment of dissolved gases (Schmid et al., 2005). Vertical profiles of temperature and dissolved substances indicate the presence of hundreds of double-diffusive staircases, with the steepest density gradient occurring at 260 m depth (Schmid et al., 2010). Recent measurements of gas concentrations show that  $\sim 300 \text{ km}^3$  of  $\text{CO}_2$  (at STP, equivalent to  $\sim 0.6 \text{ GT}$ ) and  $60 \text{ km}^3$  of  $\text{CH}_4$  ( $\sim 0.04 \text{ GT}$ ) are present in the lake's permanently stratified deep water (Schmid et al., 2005). A release of these gases would have deadly consequences for the riparian population in the Democratic Republic of the Congo and Republic of Rwanda (herein Rwanda), and may have occurred in the past in Lake Kivu (Haberyan and Hecky, 1987). Despite its modern depauperate fauna, diminished due to past overturn events (Haberyan and Hecky, 1987), Lake Kivu is the ancestral reservoir and ultimate source of thousands of endemic species observed in the other Great Lakes of East Africa (Verheyen et al., 2003). A gas-extraction project is under development in the territorial waters of Rwanda, attempting to extract  $\text{CH}_4$  from the deep water for electrical power generation of as much as to 25 MW in the near term, potentially altering lake dynamics. This study assesses the late Quaternary turbidite sedimentology of Lake Kivu, and the potential consequences of extraordinary turbidity currents.

## **Data and Methods**

A dense grid of high-resolution seismic reflection profiles, including CHIRP (compressed high-intensity radar pulse; 4 - 16 kHz) and single-channel air gun (50 - 450 Hz) data, was collected in the eastern basin of Lake Kivu during 2010-2012 (Supplementary Fig. 1). Turbidite lithofacies and ages were determined from  $^{14}\text{C}$ -dated sediment cores (Supplementary Tables 1 and 2), collected using a Kullenberg piston corer during 2012-2013 and logged with a GeoTek Multi-sensor Core Logger. The spatial distribution of turbidites was determined by integration of seismic and sediment core data (Fig. 2). Grain size and smear slide analyses were performed to study the composition and texture of the turbidite sediments. A Digital Elevation Model of the Kivu rift and single-beam bathymetric data were used to delineate onshore drainage basins and their subaqueous extensions (Fig. 1), and to determine the source of turbidity currents. Time series of turbidite bed-thickness and accumulation rate were compared with regional paleohydrologic records to understand the climatic forcing of turbidite sedimentation.

## **Geochronology**

Accelerator Mass Spectrometry  $^{14}\text{C}$  dates from 14 terrestrial plant macrofossils were used to constrain the core age models (Supplementary Table 1; Supplementary Fig. 2). The presence of numerous stratigraphic markers, including volcanic ashes, turbidites, and sedimentary laminae with distinctive appearance and composition, enables core-to-core correlation at a high

confidence level (Fig. 3; Supplementary Fig. 3), and the development of age models of individual cores.

## **Turbidite Systems**

Axial and transverse channel-lobe systems were revealed by seismic reflection data from two stratigraphic intervals (Fig. 2; Supplementary Fig. 4). Integration of seismic and core data demonstrates that most thick turbidites identified in the sediment cores are clustered within these two intervals (Fig. 3). The axial turbidite systems of the two intervals display similar depositional patterns: leveed-channels developed within a major paleo-river valley and transited basinward to elongate lobes, which are >30 km long and cover >200 km<sup>2</sup> (Figs. 1, 2A, and 2B). The best example of a transverse turbidite system was found in the northern part of the Eastern Basin, where overbank sediment waves were observed on the levees of the transverse channel (Figs. 1 and 2C).

Approximately 40 unique turbidite events were identified in the sediment cores that sample the past ~12 k.y. Most turbidites deposited by individual turbidity-flow events can be correlated between cores separated more than 30 km, but vary significantly in thickness (Fig. 3). Individual turbidite thickness in the sediment cores ranges from 0.1 to >100 cm, with thick turbidites commonly capped by diatomites. Maximum sediment volume in a single event is  $\sim 4 \times 10^7$  m<sup>3</sup>. The turbidite sediments are silt- to coarse sand-sized (Supplementary Figs. 5 and 6), and moderately sorted. Rip-up clasts and centimeter-thick pieces of previously deposited mud are

abundant in proximal channel and levee deposits, as well as in distal lobe deposits. Their presence indicates the erosive and hyperpycnal nature of the turbidity currents. Interflow behavior is also expected. As turbidity flows move basinward, the upper, low-density part of the turbidity currents may become detached, and travel along the chemocline as an interflow. Both normal and reverse-to-normal grading were observed on grain size profiles of individual turbidite events (Supplementary Fig. 6). The terrigenous mineral components of the turbidite sediments include quartz, muscovite, and feldspar grains derived from onshore metamorphic basement rocks. Terrestrial plant macrofossils are common, especially in the channel deposits. Aquatic organic matter and diatom frustules, which were entrained into turbidity currents during flow processes, are also abundant in the turbidite sediments, and become dominant in the finer-grained lobe deposits.

## **Discussion**

### ***Source of Turbidity Currents***

Although the Kivu rift has been seismically and volcanically active, the majority of the turbidites observed in the sediment cores were most likely sourced by hyperpycnal river flows during extreme floods (3-4 events/k.y.), rather than by slope failures triggered by earthquakes or by pyroclastic flows during volcanic eruptions. Evidence supporting the flood origin of the turbidity currents includes: (1) the physical connection between the axial and transverse turbidite channels and the onshore drainages (Fig. 1); (2) the reverse-to-normal grading observed in the

turbidites (Supplementary Fig. 6), typical of hyperpycnal river flow deposits, that records the waxing and waning phases of a discharge (Mulder et al., 2001); (3) the correlation between the turbidite record and wet climate intervals, indicated by the regional paleohydrologic data; (4) the absence of pyroclastic materials in the turbidite sediments, indicating that the turbidity currents were not triggered by pyroclastic flows; and (5) that sediment failures and mass transport deposits, possibly triggered by seismic events, are only locally distributed and associated with isolated steep slopes (Fig. 2C), and are not observed in the southern part of the Eastern Basin where the axial turbidite systems originated. Accordingly, the turbidity currents are interpreted as primarily sourced by flood-triggered hyperpycnal flows during exceptional rainfall events.

### ***Climatic Control of Hyperpycnite Events***

The hyperpycnite record (Supplementary Table 3) of Lake Kivu is correlated with the regional paleohydrologic records from tropical East Africa. Accommodation space at most of the core sites become available at ~12.2 ka, when the water-level of Lake Kivu began to rise after a pronounced -380 m lowstand indicated by paleo-deltas (Fig. 4F; Supplementary Figs. 7 and 8). The first hyperpycnite event in sediment cores appeared at ~11 ka (Fig. 4G). This timing coincides with rapid lake-level rise of Kivu and other East African lakes, e.g. Lake Turkana (Garcin et al., 2012; Morrissey and Scholz, 2014) and Lake Challa (Tierney and deMenocal, 2013).

The recent hydrologic connection between Lakes Kivu and Tanganyika was established at ~10 ka, evidenced by both the elemental and  $^{87}\text{Sr}/^{86}\text{Sr}$  records of Lake Tanganyika (Felton, et al., 2007). Shells from a terrace 100 m above present lake-level were dated to 12.4 ka (Olson and Broecker, 1959), but Haberyan and Hecky (1987) suggested that this date is probably too old due to a carbon reservoir effect, and probably marks the hydrologic opening of Lake Kivu in the early Holocene. The hydrologic opening of Lake Kivu at ~10 ka (Felton, et al., 2007) correlates with a rapid increase in hyperpycnite accumulation rate (Fig. 4G). From ~12 - 10 ka, lake-level of Kivu had risen ~480 m (Fig. 4F); such high-magnitude lake-level changes within a short time are characteristic of steep-sided African lakes (Haberyan and Hecky, 1987; Scholz et al., 2007; Lyons et al., 2011).

The cessation of hyperpycnite sedimentation between ~8.6 and 7.6 ka (Fig. 4G) may correlate with the 8.2 ka event, a prominent cold and dry event identified in widespread proxy records in the Northern Hemisphere (Alley et al., 1997). The synchronous lake-level lowstands observed in numerous tropical East African lakes at ~8 ka, e.g. Lakes Ziway-Shala (Gillespie et al., 1983) and Turkana (Garcin et al., 2012), were linked to this short-lived event (Gasse, 2000). Following the 8.2 ka event, warm and humid conditions in tropical East Africa resumed and remained until ~5 ka, when a wet-dry transition took place, marking the end of the East African Humid Period (EAHP, 11-5 ka; Tierney and deMenocal, 2013). The  $\delta\text{D}$  data of terrestrial leaf waxes from Lakes Challa (Fig. 4A; Tierney and deMenocal, 2013), Tanganyika (Fig. 4B Tierney et al., 2008), and Victoria (Fig. 4C; Berke et al., 2012) indicate that climate in tropical East

Africa generally stayed dry from the end of EAHP until ~3.2 ka. Between ~5 and 3.2 ka, minimum rainfall (Berke et al., 2012) and widespread lake-level lowstands (Gasse, 2000) were observed. The hyperpycnite accumulation rate of Lake Kivu generally followed these changes; it first dramatically increased following the 8.2 ka event, and later ceased between ~5.5 and 4 ka. After that, hyperpycnite sedimentation resumed but accumulation rate remained low until ~3 ka (Fig. 4G). During the 8.2 ka event and between ~5 and 3.2 ka, Lake Kivu, like many other East African lakes (Gasse, 2000), probably had lake-level lowstands (Fig. 4F).

Lakes Kivu and Tanganyika were hydrologically connected during the late Holocene, based on the evidence that the Ca concentration of the Lake Tanganyika sediments (Fig. 4D) covaried with the total inorganic carbonate (TIC) record of Lake Kivu (Fig. 4E; Supplementary Table 4) between ~3.2 ka and present. This suggests that lake-levels of Kivu were close to or at the spill point during most of the late Holocene. Regional paleohydrologic records suggest a shift from the rainfall minimum to relatively wetter conditions in tropical East Africa at ~3.2 ka (Berke et al., 2012; Tierney and deMenocal, 2013). Lake-level transgressions at ~3 ka were also observed in various tropical East African lakes, e.g. Lakes Abhe (Gasse, 1977) and Ziway-Shala (Gillespie et al., 1983). During the late Holocene, the temporal occurrences of hyperpycnites, especially decimeter-thick layers, generally correlate with wet climate intervals (Fig. 4). The hyperpycnite record of Lake Kivu over the past ~12 ka demonstrates that flood-introduced turbidites preserved in deep lakes are indicators of millennial-scale hydrological changes.

### ***Implications for Deep Mixing and Geologic Hazards***

The sediment stratigraphy of Lake Kivu suggests that exceptional floods may have triggered deep mixing events in the lake's recent history. Most thick diatomites (>1 cm) in the sediment cores are associated with the centimeter- to meter-thick turbidites deposited between ~9.5 and 7 ka, and between ~3 and 1 ka (Fig. 3). The diatomite beds capping the thick turbidites (Supplementary Figs. 3, 5, and 6) are probably the result of deep mixing events, when upwelling of nutrient-rich deep waters led to intense diatom blooms. Thick diatomites are observed in cores recovered from shallower water depths in the eastern basin without any accompanying hyperpycnites (Supplementary Fig. 9), as well as from cores collected in the 1970's in the northern basin of the lake (Haberyan and Hecky, 1987). The northern basin is separated from the Eastern Basin by the Idjwi Island horst and subaqueous volcanic domes (Fig. 1; Supplementary Fig. 1). This suggests that the diatomites capping the hyperpycnites were more likely caused by lake-wide events rather than as a result of sorting during turbidity-flow processes. The diatomites are predominantly comprised of centric species, and there is a sharp decrease in grain size across the hyperpycnite-diatomite boundary (Supplementary Fig. 6). The hyperpycnite sediments contain abundant diatom frustules, indicating that the diatoms were not preferentially sorted on top. These indicate that the diatomites above the hyperpycnites were probably not a result of sorting or interflow behavior. The turbulence of extraordinary turbidity-flows may disrupt the micro- and macro-scale staircase stratification of the lake (Schmid et al., 2010), inducing deep mixing. The response of diatoms to such deep mixing events was probably heterogeneous across



the lake. The thickest diatomite beds (~9 cm) were found in core 12-16B (Fig. 3; Supplementary Fig. 3) from the central part of the Eastern Basin, where basinward-traveling turbidity flows were probably uplifted by narrowed lake-floor topography (Fig. 1), resulting in enhanced upwelling.

The turbidity currents triggered by extreme floods appear to be highly erosive, indicated by the presence of numerous large rip-up clasts (Supplementary Fig. 5), even in distal and marginal lobe deposits. Erosive channel features are also present on the axial lobes (Fig. 2B). These suggest that extraordinary turbidity currents, due to their strong erosivity, may trigger geologic hazards, which are potential risks for the current degassing efforts in Lake Kivu. Such risks need be recognized in the design and deployment of gas extraction facilities.

## **Acknowledgements**

We gratefully acknowledge the Government of the Republic of Rwanda for permission to conduct this research, for logistical support, and for providing the bathymetric data. We thank the National Lacustrine Core Facility (LacCore) for core logging and assistance in the field. Thanks to J. Corbett, P. Cattaneo, J. Greenberg, and A. Morrissey for contributions during the field campaigns; to B. Wilkinson for early reviews; and to three anonymous reviewers for constructive comments. Support for the research was provided by MacArthur Foundation, Vanoil Energy, and the Industrial Associates of the Syracuse University Lacustrine Rift Basin Research Program.

## References Cited

- Alley, R.B., Mayewski, P.A., Stuiver, M., Taylor, K.C., and Clark, P.U., 1997, Holocene climate instability: A prominent, widespread event 8200 yr ago: *Geology*, v. 25, p. 483–486, doi:10.1130/0091-7613(1997)025<0483:HCIAPW>2.3.CO;2.
- Beadle, L.C., 1981, *The inland waters of tropical Africa: An introduction to tropical limnology*: London, Longman, 475 p.
- Berke, M.A., Johnson, T.C., Werne, J.P., Grice, K., Schouten, S., and Sinninghe Damsté, J.S., 2012, Molecular records of climate variability and vegetation response since the Late Pleistocene in the Lake Victoria basin, East Africa: *Quaternary Science Reviews*, v. 55, p. 59–74, doi:10.1016/j.quascirev.2012.08.014.
- Degens, E.T., and Kulbicki, G., 1973, Hydrothermal origin of metals in some East African Rift Lakes: *Mineralium Deposita*, v. 4, p. 388–404. doi:10.1007/BF00207520.
- Ebinger, C.J., 1989, Tectonic development of the western branch of the East African rift system: *Geological Society of America Bulletin*, v. 101, p. 885–903, doi:10.1130/0016-7606(1989)101<0885:TDOTWB>2.3.CO;2.
- Felton, A.A., Russell, J.M., Cohen, A.S., Baker, M.E., Chesley, J.T., Lezzar, K.E., McGlue, M.M., Pigati, J.S., Quade, J., Stager, J.C., and Tiercelin, J.J., 2007, Paleolimnological evidence for the onset and termination of glacial aridity from Lake Tanganyika, tropical East Africa: *Palaeogeography, Palaeoclimatology, Palaeoecology*, v. 252, p. 405–423, doi:10.1016/j.palaeo.2007.04.003.

- Garcin, Y., Melnick, D., Strecker, M.R., Olago, D., and Tiercelin, J.-J., 2012, East African mid-Holocene wet–dry transition recorded in palaeo-shorelines of Lake Turkana, northern Kenya Rift: *Earth and Planetary Science Letters*, v. 331–332, p. 322–334, doi:10.1016/j.epsl.2012.03.016.
- Gasse, F., 1977, Evolution of Lake Abhe (Ethiopia and T.F.A.I.) from 70,000 B.P: *Nature*, v. 265, p. 42–45, doi:10.1038/265042a0.
- Gasse, F., 2000, Hydrological changes in the African tropics since the Last Glacial Maximum: *Quaternary Science Reviews*, v. 19, p. 189–211, doi:10.1016/S0277-3791(99)00061-X.
- Gillespie, R., Street-Perrott, F.A., and Switzer, R., 1983, Post-glacial arid episodes in Ethiopia have implications for climate prediction: *Nature*, v. 306, p. 680–683, doi:10.1038/306680a0.
- Haberyan, K.A., and Hecky, R.E., 1987, The late Pleistocene and Holocene stratigraphy and Paleolimnology of lake Kivu and Tanganyika: *Palaeogeography, Palaeoclimatology, Palaeoecology*, v. 61, p. 169–197, doi:10.1016/0031-0182(87)90048-4.
- Lyons, R.P., Scholz, C.A., Buoniconti, M.R., and Martin, M.R., 2011, Late Quaternary stratigraphic analysis of the Lake Malawi Rift, East Africa: An integration of drill-core and seismic-reflection data: *Palaeogeography, Palaeoclimatology, Palaeoecology*, v. 303, p. 20–37, doi:10.1016/j.palaeo.2009.04.014.
- Meiburg, E., and Kneller, B., 2009, Turbidity currents and their deposits: *Annual Review of Fluid Mechanics*, v. 42, p. 135–156, doi:10.1146/annurev-fluid-121108-145618.

- Morrissey, A., and Scholz, C.A., 2014, Paleohydrology of Lake Turkana and its influence on the Nile River System: *Palaeogeography, Palaeoclimatology, Palaeoecology*, v. 403, p. 88–100, doi:10.1016/j.palaeo.2014.03.029.
- Mulder, T., Migeon, S., Savoye, B., and Jouanneau, J.-M., 2001, Twentieth century floods recorded in the deep Mediterranean sediments: *Geology*, v. 29, p. 1011–1014, doi:10.1130/0091-7613(2001)029<1011:TCFRIT>2.0.CO;2.
- Noren, A.J., Bierman, P.R., Steig, E.J., Lini, A., and Southon, J., 2002, Millennial-scale storminess variability in the northeastern United States during the Holocene epoch: *Nature*, v. 419, p. 821–824, doi:10.1038/nature01132.
- Olson, E.A., and Broecker, W.S., 1959, Lamont natural radiocarbon measurements: *American Journal of Science*, v. 257, p. 1–28, doi:10.2475/ajs.257.1.1.
- Schmid, M., Halbwachs, M., Wehrli, B., and Wüest, A., 2005, Weak mixing in Lake Kivu: New insights indicate increasing risk of uncontrolled gas eruption: *Geochemistry Geophysics Geosystems*, v. 6, Q07009, doi:10.1029/2004GC000892.
- Schmid, M., Busbridge, M., and Wüest, A., 2010, Double-diffusive convection of Lake Kivu: *Limnology and Oceanography*, v. 55, p. 225–238, doi:10.4319/lo.2010.55.1.0225.
- Schillereff, D.N., Chiverrell, R.C., Macdonald, N., and Hooke, J.M., 2014, Flood stratigraphies in lake sediments: A review: *Earth-Sciences Reviews*, v. 135, p. 17–37. doi:10.1016/j.earscirev.2014.03.011.

- Scholz, C.A., Johnson, T.C., Cohen, A.S., King, J.W., Peck, J.A., Overpeck, J.T., Talbot, M.R., Brown, E.T., Kalindekaffe, L., Amoako, P.Y.O., Lyons, R.P., Shanahan, T.M., Castaneda, I.S., Heil, C.W., Forman, S.L., McHargue, L.R., Beuning, K.R., Gomez, J., and Pierson, J., 2007, East African megadroughts between 135 and 75 thousand years ago and bearing on early-modern human origins: *Proceedings of the National Academy of Sciences of the United States of America*, v. 104, p. 16416–16421, doi:10.1073/pnas.0703874104.
- Stoffers, P., and Hecky, R.E., 1978, Late Pleistocene–Holocene evolution of the Kivu-Tanganyika Basin, in Matter, A., and Tucker, M.E., eds., *Modern and ancient lake sediments: Internal Association of Sedimentologists Special Publication 2*, p. 43–45, doi:10.1002/9781444303698.ch3.
- Tierney, J.E., and deMenocal, P.B., 2013, Abrupt shifts in horn of Africa hydroclimate since the Last Glacial Maximum: *Science*, v. 342, p. 843–846. doi:10.1126/science.1240411.
- Tierney, J.E., Russell, J.M., Huang, Y., Sinninghe Damsté, J.S., Hopmans, E.H., and Cohen, A.S., 2008, Northern hemisphere controls on tropical southeast African climate during the past 60,000 Years: *Science*, v. 322, p. 252–255, doi:10.1126/science.1160485.
- Verheyen, E., Salzburger, W., Snoeks, J., and Meyer, A., 2003, Origin of the Superflock of Cichlid Fishes from Lake Victoria, East Africa: *Science*, v. 300, p. 325–329. doi:10.1126/science.1080699.

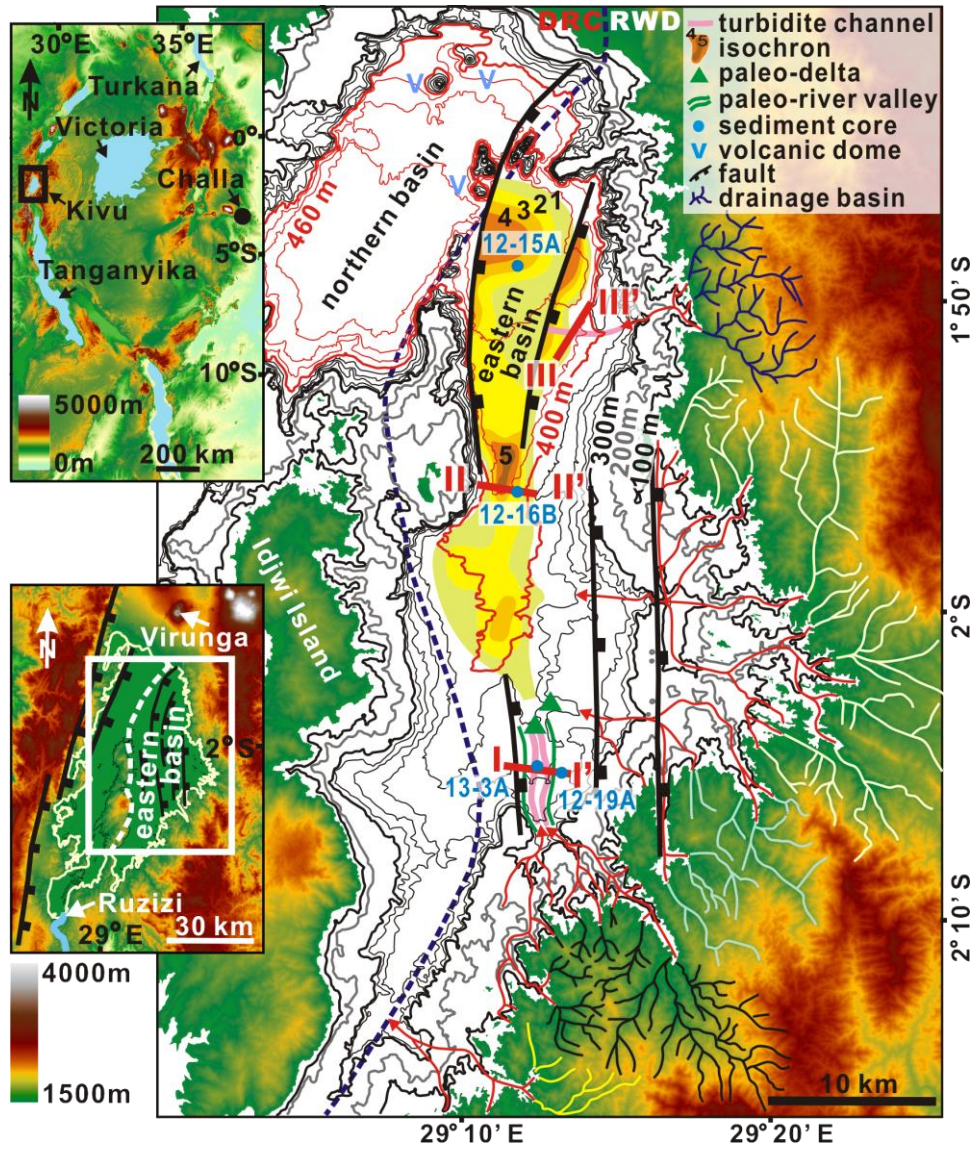


**Figure 1.** Regional topography and structural framework of the Kivu rift. Main map shows major intrabasinal structures, lake-floor bathymetry, onshore drainage basins and their subaqueous extensions, and development of axial and transverse turbidite systems in the Eastern Basin of the lake. Depositional thickness of the axial turbidite lobe (bounded by the red and yellow seismic horizons in Figure 2) is contoured in milliseconds two-way travel time (ms TWTT, 1 ms TWTT  $\approx$  0.75 m). I-I', II-II' and III-III' are CHIRP seismic profiles displayed in Figure 2. DRC = Democratic Republic of the Congo; RWD = Republic of Rwanda.

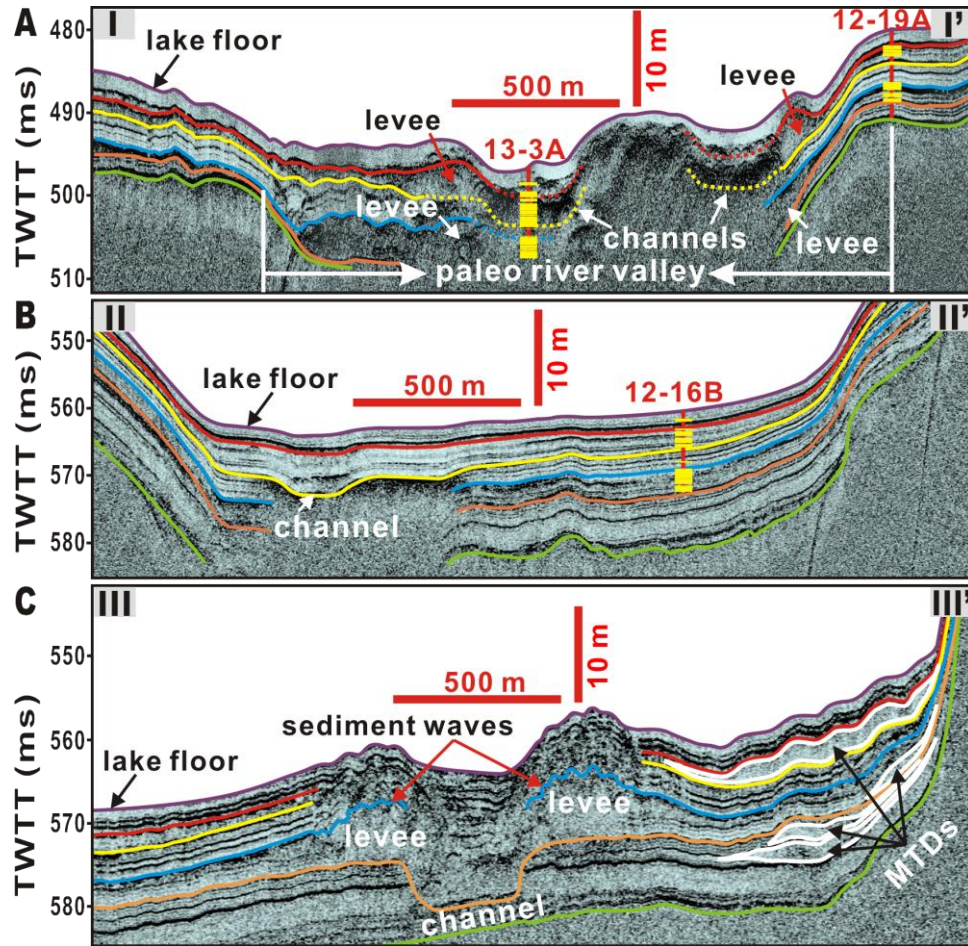


**Figure 2.** Axial and transverse channel-lobe systems were revealed by seismic and core data from two stratigraphic intervals, i.e. the intervals bounded by the red and yellow seismic horizons, and by the blue and orange horizons. The green seismic horizon shows the acoustic basement of the CHIRP seismic data. Turbidites thicker than 1 cm from cores 12-19A, 13-3A, and 12-16B are shown in yellow. TWTT = two-way travel time; MTDs = mass transport deposits. See Figure 1 for the locations of the seismic lines.

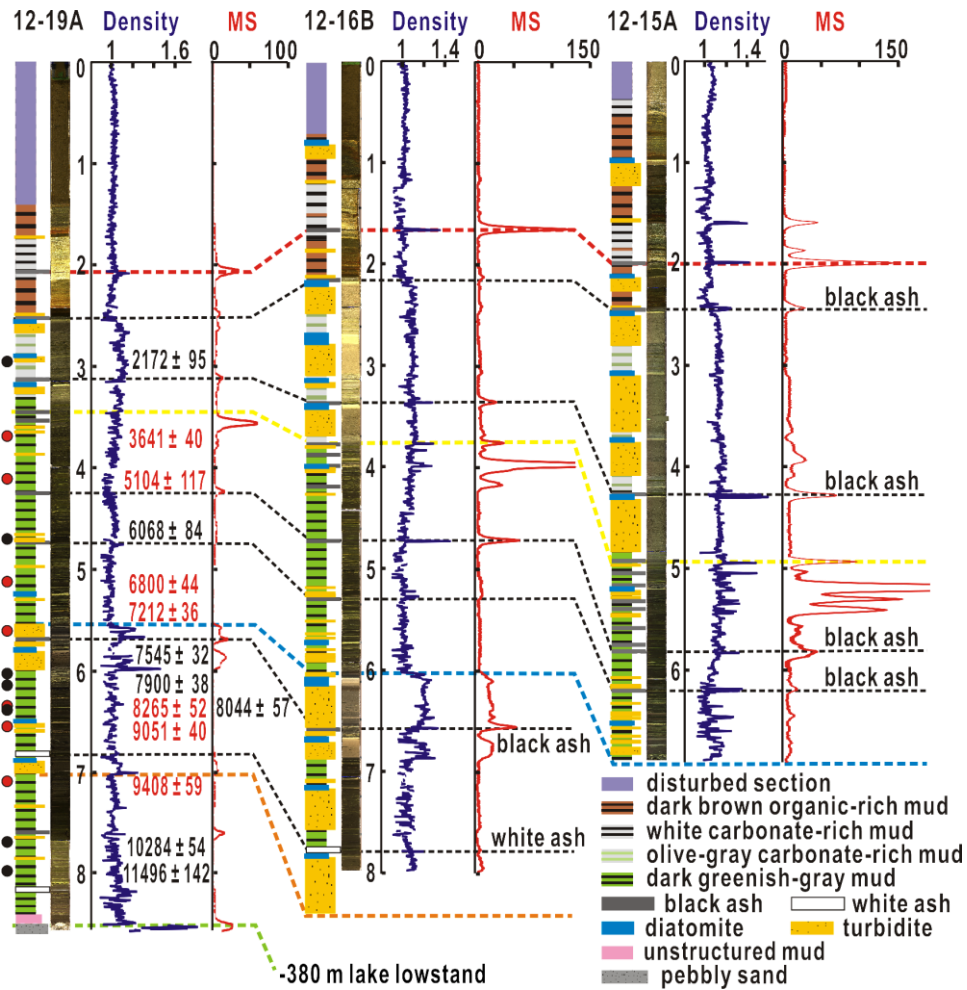


**Figure 3.** Correlation of sediment cores 12-19A, 12-16B, and 12-15A based on various stratigraphic markers. Radiocarbon samples are indicated by the solid red (dates from core 12-19A) and black (dates from other cores) circles. The blue and red curves alongside core images and lithologic columns are GeoTek measurements of gamma-ray attenuation density ( $\text{g}/\text{cm}^3$ ) and magnetic susceptibility (MS, SI units  $\times 10^{-5}$ ), respectively. The red, yellow, blue, orange, and green correlation lines correspond to the seismic horizons in Figure 2. Downcore depth scale is in meters. See the core locations in Figure 1.



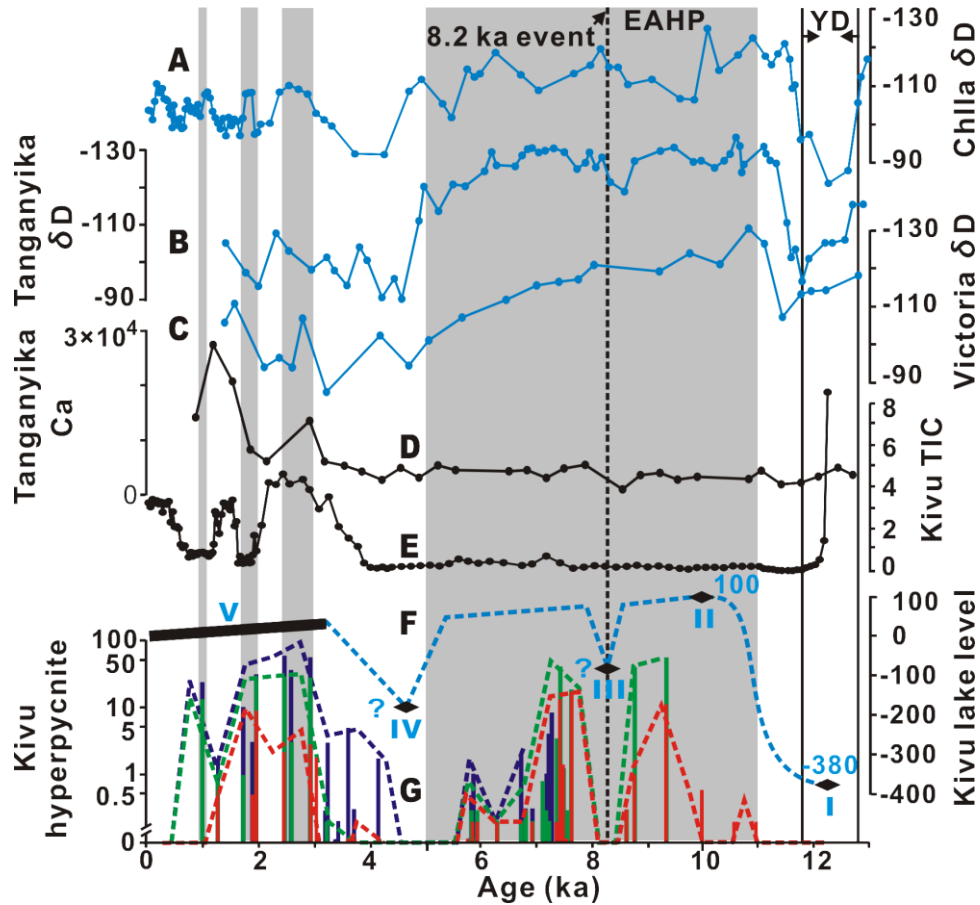
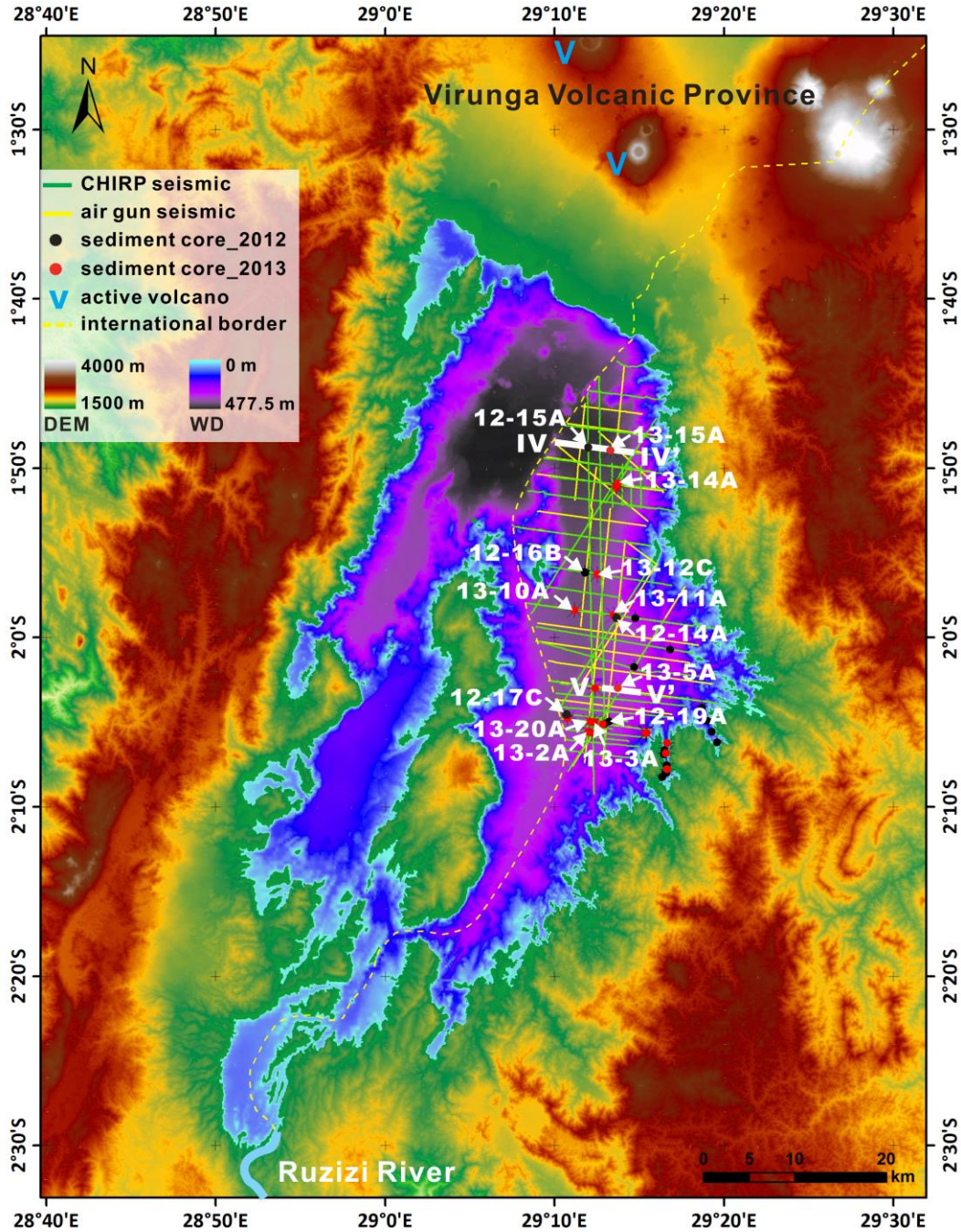
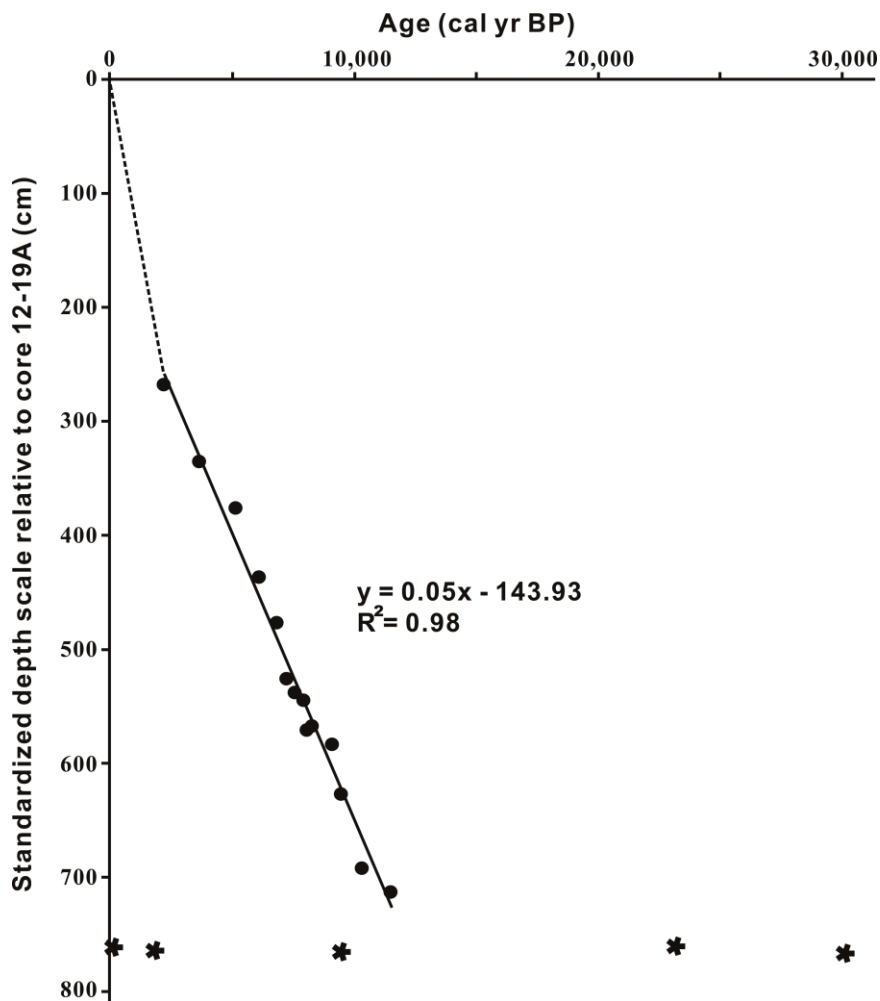


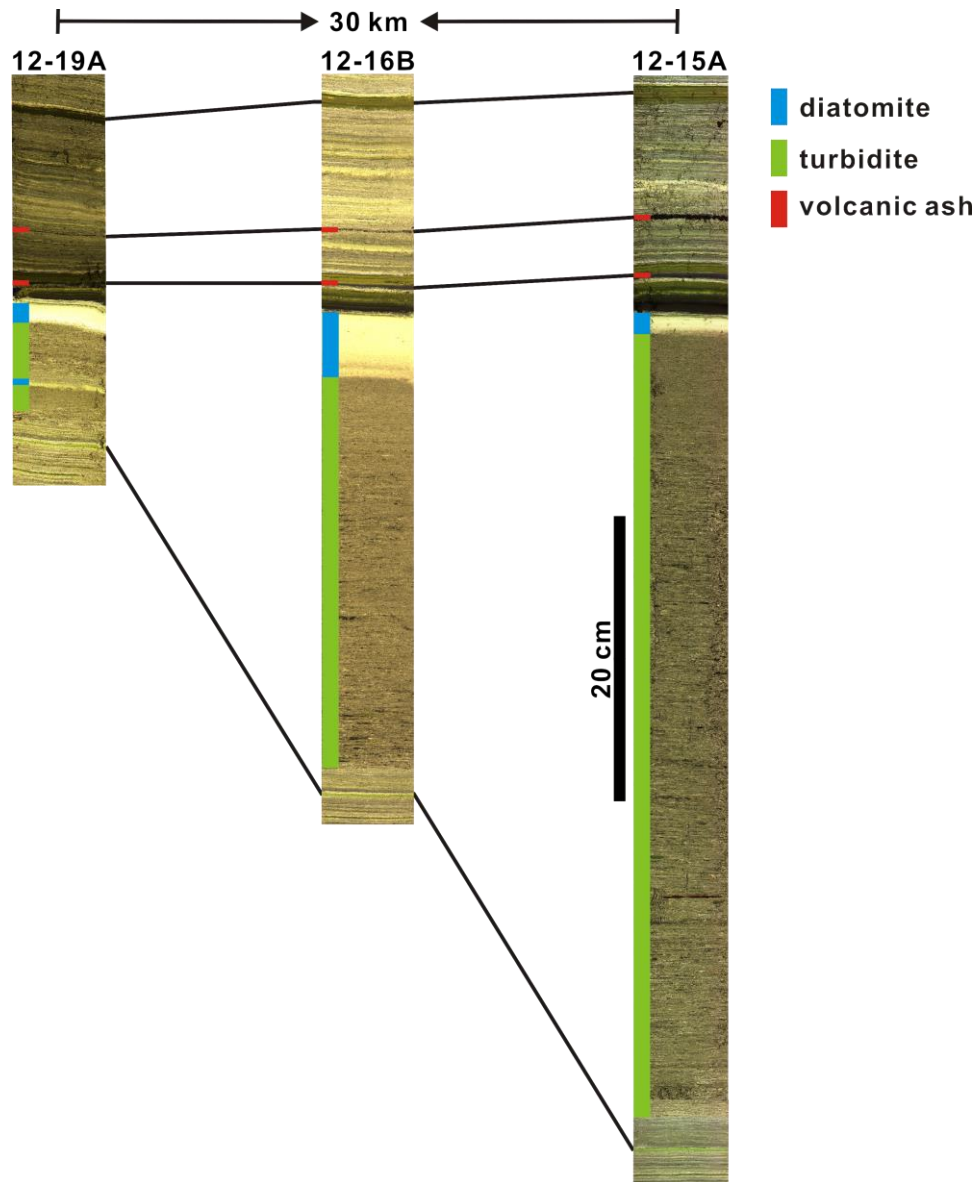
**Figure 4.** A–C:  $\delta D_{\text{leaf wax}}$  (‰) records of Lakes Challa (Tierney and deMenocal, 2013), Tanganyika (Tierney et al., 2008), and Victoria (Berke et al., 2012). D: Inductively coupled plasma–mass spectrometry (ICP-MS) Ca measurements (cps) of Lake Tanganyika sediments (Felton et al., 2007). E: Total inorganic carbon (TIC, %) record of Lake Kivu. F: Lake-level (meters above present lake-level) history of Kivu. I: -380 m lake-level lowstand at ~12.2 ka, indicated by paleodeltas (Fig. 1; Supplementary Figs. 7 and 8); II: opening of Lake Kivu at ~10 ka (Felton et al., 2007). III and IV: postulated water-level lowstands during the 8.2 ka event and at the end of EAHP; and V: the hydrologic connection between Lakes Kivu and Tanganyika during the late Holocene suggests generally high lake-levels of Kivu. G: Time series of hyperpycnite thickness and accumulation rate from cores 12-19A (red), 12-16B (green), and 12-15A (dark blue). The vertical bars indicate individual layer thickness (cm), and the dashed lines indicate accumulative thickness per 0.5 k.y. Shadings highlight the EAHP and the later occurrences of thick turbidites (>10 cm). YD = the Younger Dryas.



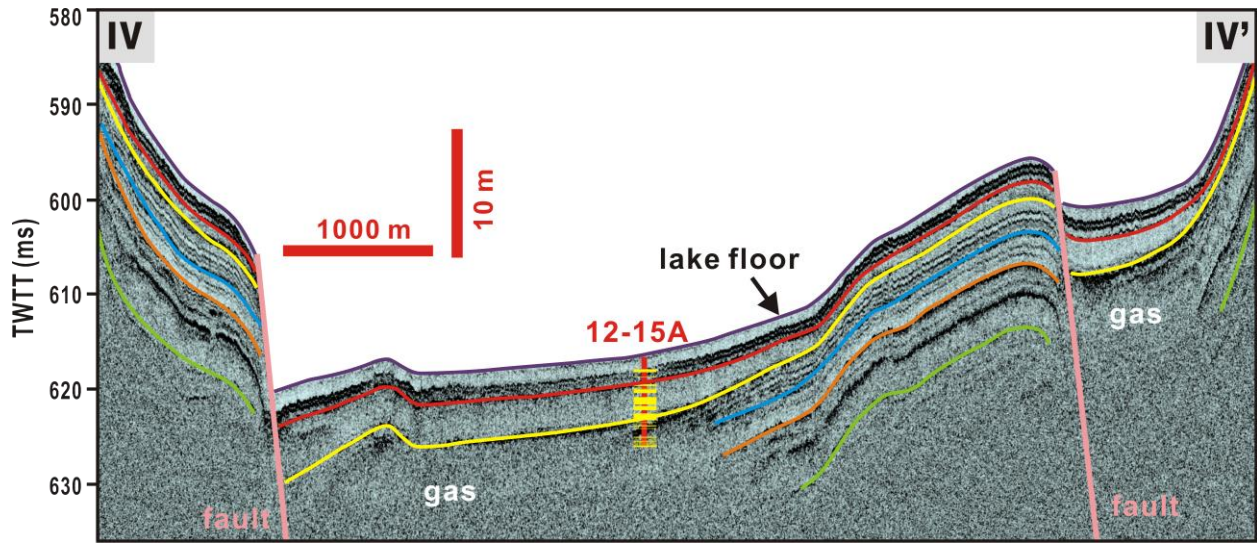
**Supplementary Figure 1.** Basemap of Lake Kivu showing regional Digital Elevation Model (ASTER GDEM, a product of METI and NASA), lake-floor bathymetry (Zal, 2014), seismic tracklines, and sediment core stations. DEM = Digital Elevation Model; and WD = water depth. IV-IV' and V-V' are seismic profiles displayed in Supplementary Figures 4 and 7.



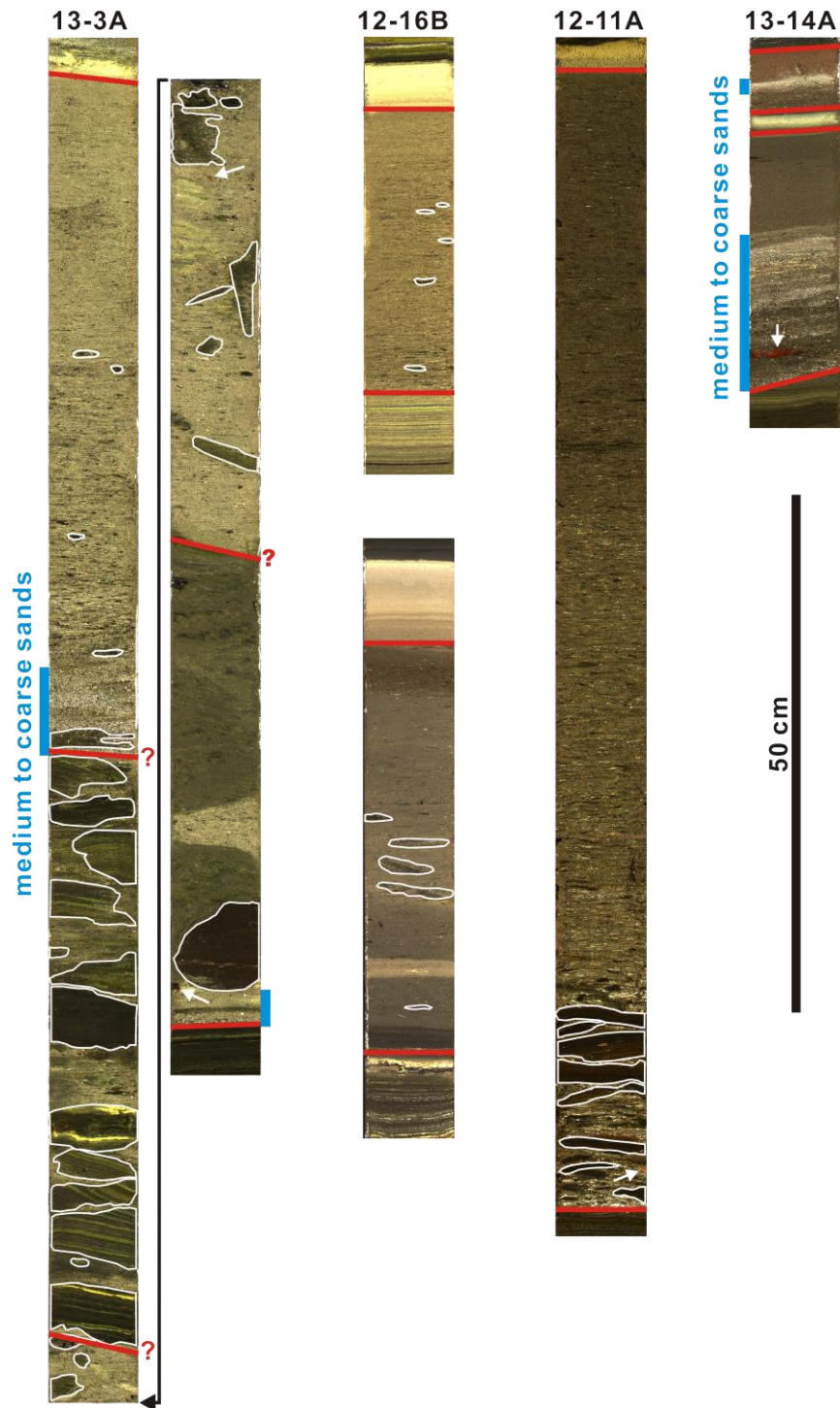
**Supplementary Figure 2.** The age model of sediment core 12-19A.  $^{14}\text{C}$  dates indicated by \* are not used (Also see Supplementary Table 1). The upper ~1.5 m sediment column of 12-19A is disturbed and saturated with water due to outgassing when the core was brought to surface.



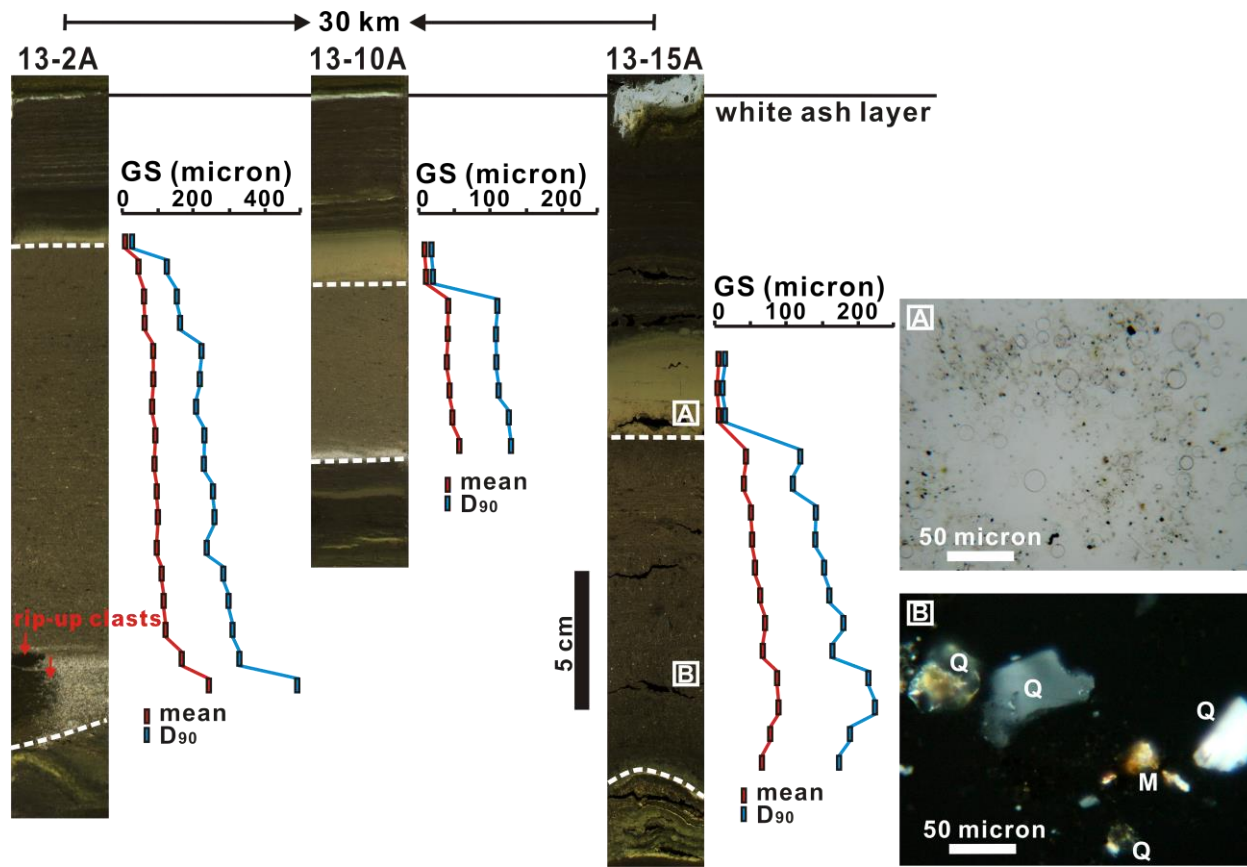
**Supplementary Figure 3.** An example of core-to-core correlation over ~30 km, using various distinctive stratigraphic markers. Note the turbidites are capped by thick diatomites. See the core locations in Supplementary Figure 1.



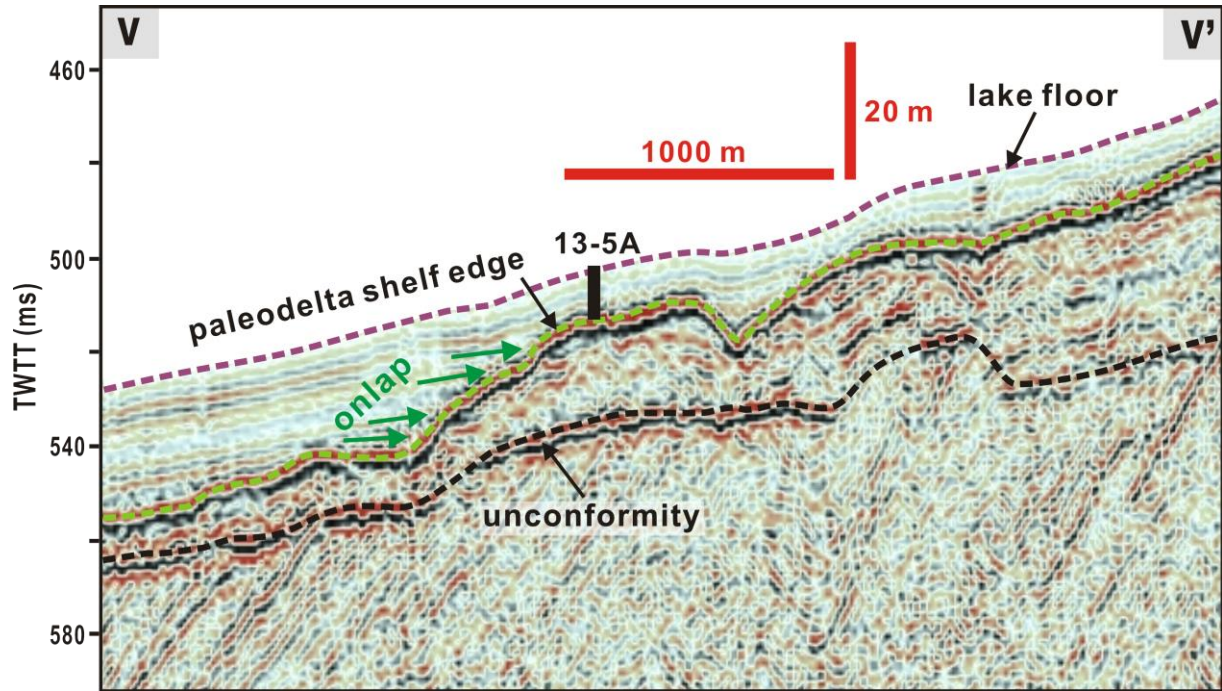
**Supplementary Figure 4.** A CHIRP seismic profile showing the development of turbidite systems in the deepest part of the Eastern Basin. Turbidites identified in core 12-15A are shown in yellow. See the location of the seismic line in Supplementary Figure 1.



**Supplementary Figure 5.** Rip-up clasts and centimeter-thick previously deposited mud (outlined in white) are abundant in thick beds (bounded by the red lines) of turbidite channel (13-3A and 13-14A) and lobe (12-16B) deposits. Terrestrial macroplants are indicated by arrows. Note the thick turbidites are commonly capped by diatomites. See the core locations in Supplementary Figure 1.

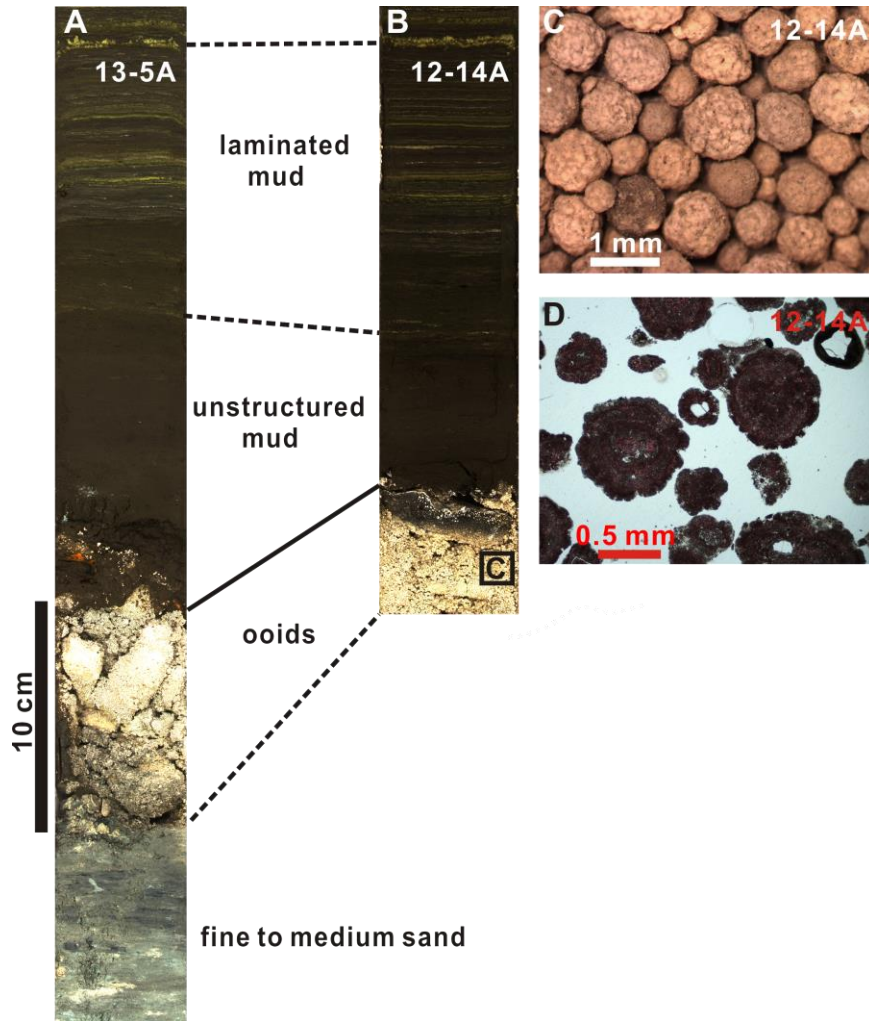


**Supplementary Figure 6.** Sediment texture and composition of correlative hyperpycnite beds (bounded by the white dash lines) and the overlying diatomites from cores 13-2A, 13-10A, and 13-15A. Note the sharp decrease in particle size (measured with a Beckman Coulter LS230 Laser Diffraction Particle Size Analyzer) across the hyperpycnite-diatomite boundary. Large rip-up clasts are present in core 13-2A. M = muscovite; Q = quartz; GS = grain size; and  $D_{90}$  = the 90<sup>th</sup> particle size percentile. See the core locations in Supplementary Figure 1.

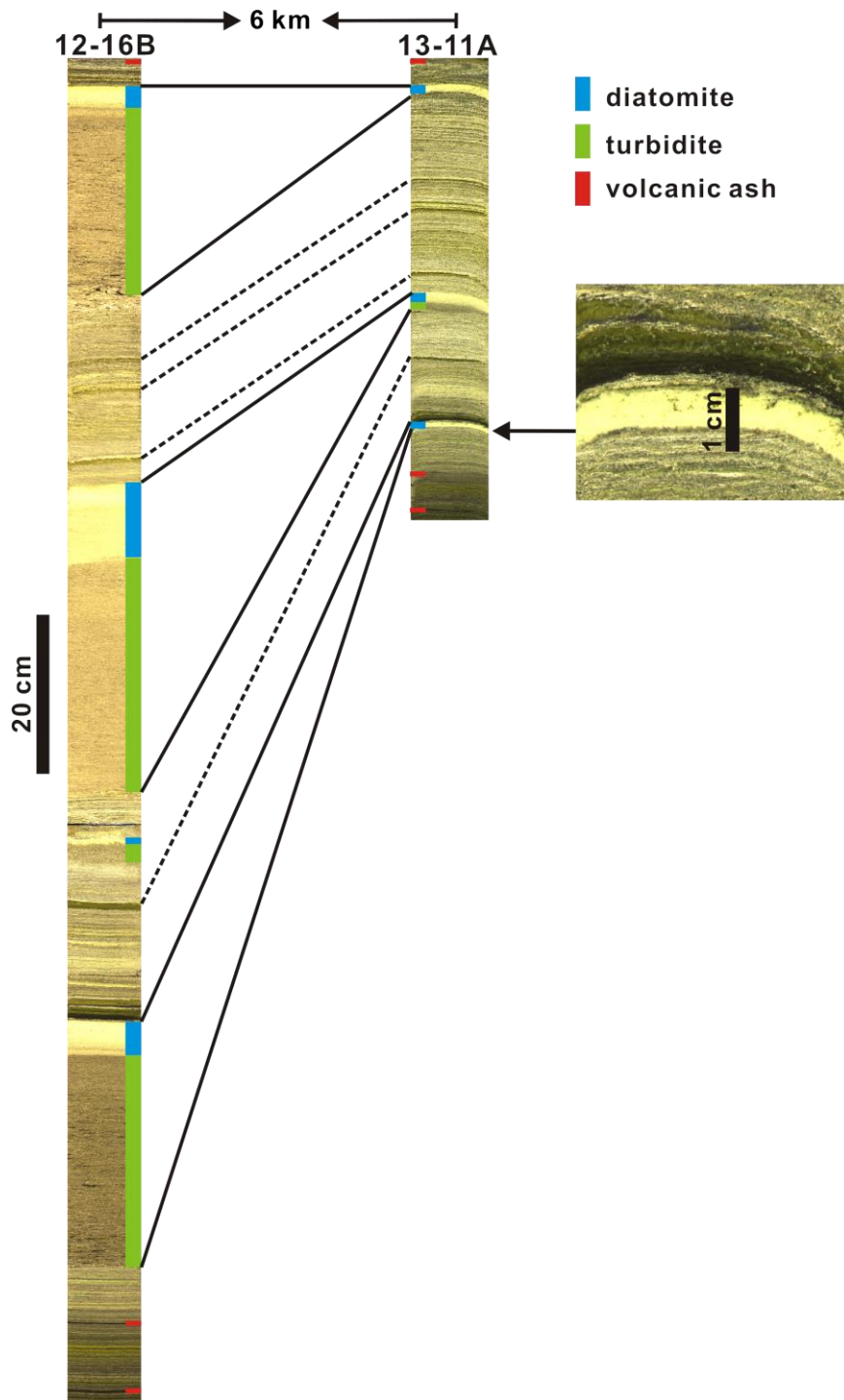


**Supplementary Figure 7.** A single-channel air gun seismic reflection profile showing the ~12.2 ka lowstand indicated by paleo-deltas that are 380 m below present lake-level. See the core image of 13-5A in Supplementary Figure 8 and the location of the seismic line in Supplementary Figure 1.





**Supplementary Figure 8.** A-B: Core images of 13-5A and 12-14A showing the transition from deltaic and ooid facies to laminated mud facies at ~12 ka. C: Ooids from core 12-14A. D: Petrographic image of the ooids with calcite stained in red. Note the nuclei of many ooids are quartz grains. See the core locations in Supplementary Figure 1.



**Supplementary Figure 9.** Correlation between sediment cores 12-16B and 13-11A showing the presence of diatomites without the presence of hyperpycnites in shallower water cores. Cores 12-16 and 13-11 were recovered in water depth of 414 m and 364 m, respectively. See the core locations in Supplementary Figure 1.

**Supplementary Table 1.** Accelerator Mass Spectrometry <sup>14</sup>C ages.

Core	Section	Section Depth (cm)	Material	SD (cm)	Age ( <sup>14</sup> C yr BP)	Age (cal yr BP)
12-19A	4	55	macroplant	371, 334	3390 ± 30	3641 ± 40
	5	12.5	macroplant	413.5, 376.4	4440 ± 30	5104 ± 117
	6	45.5	macroplant	515.5, 476.7	5960 ± 30	6800 ± 44
	6	94	macroplant	564, 524.8	6270 ± 40	7212 ± 36
	7	18	macroplant	638, 566.1	7430 ± 40	8265 ± 52
	7	35	macroplant	655, 582.8	8100 ± 40	9051 ± 40
13-12C	4	60	macroplant	473.5, 435.4	5270 ± 40	6068 ± 84
	5	51	macroplant	615, 544.1	7060 ± 40	7900 ± 38
13-15A	5	104	macroplant	608.5, 537.6	6670 ± 40	7545 ± 32
	6	39.5	macroplant	642, 570.1	7210 ± 40	8044 ± 57
13-20A	3	123	macroplant	297, 266.8	2140 ± 30	2172 ± 95
	7	59	macroplant	776.5, 691.5	9100 ± 50	10284 ± 54
13-2A	7	104	macroplant	711, 626.8	8390 ± 40	9408 ± 59
	7	135.5	gastropod	852, 766.8	25220 ± 240	30095 ± 291*
13-5A	6	49.5	macroplant	796.5, 711.3	10000 ± 40	11496 ± 142
	6	92-95	bulk	845.5, 760.3	19380 ± 80	23142 ± 272*
	6	106	macroplant	849, 763.8	160 ± 30	144 ± 114*
	6	108	macroplant	851, 765.8	1860 ± 30	1799 ± 48*
	6	108	macroplant	851, 765.8	8420 ± 40	9469 ± 28*

SD: standardized depth scale relative to core 12-19A. The SD depths before and after adjustments for core caps and turbidites are given for each radiocarbon sample. Due to the instantaneous nature of turbidite sedimentation, turbidites were removed from the depth scale before developing age models. Measured radiocarbon dates were calibrated using the calibration curve CalPal2007\_HULU (CalPal-2007<sup>online</sup>, Danzeglocke et al., 2013).

\*: <sup>14</sup>C dates that are excluded. The <sup>14</sup>C samples of bulk sediments and gastropod shells give extremely old dates due to input of geogenic old carbon from hydrothermal activity. The three macroplant samples appearing above ooids at the bottom of core 13-5A give inverted dates; these were contaminated from shallower depths during the coring process.

**Supplementary Table 2.** Metadata of sediment cores.

Core	Latitude (degree)	Longitude (degree)	Water Depth (m)	Core Length (m)
12-11A	-2.01180	29.28016	318	7.9
12-13A	-1.98098	29.24598	319	8
12-14A	-1.97789	29.22484	356	7.9
12-15A	-1.81299	29.19967	455	6.9
12-16B	-1.93542	29.19668	414	8
12-17C	-2.07861	29.17939	365	7.1
12-19A	-2.08513	29.21562	352	8.6
13-2A	-2.09288	29.19973	355	7.4
13-3A	-2.08340	29.20585	372	7.1
13-5A	-2.05102	29.22775	361	6.9
13-10A	-1.97307	29.18649	412	6.6
13-11A	-1.97778	29.22491	364	6.4
13-12C	-1.93763	29.20860	385	8.4
13-14A	-1.84836	29.22823	428	8.7
13-15A	-1.81590	29.22179	444	8.1
13-20A	-2.08260	29.20123	370	8.2

**Supplementary Table 3.** Turbidites observed in cores 12-19A, 12-16B, and 12-15A.

Core	Section	Top (cm)	Bottom (cm)	Downcore Depth (cm)	Thickness (cm)	Age (cal yr)
12-19A	2	32.5	33	173.5	0.5	1266
12-19A	3	9	9.5	252	0.5	1901
12-19A	3	15	24	258	9	1946
12-19A	3	49.3	51.5	292.3	2.2	2449
12-19A	4	4.7	7.5	320.7	2.8	2918
12-19A	4	9.2	11	325.2	1.8	2951
12-19A	4	45.5	45.6	361.5	0.1	3620
12-19A	4	50.5	50.6	366.5	0.1	3715
12-19A	4	73.6	73.7	389.6	0.1	4161
12-19A	6	6	6.1	476	0.1	5815
12-19A	6	6.7	6.9	476.7	0.2	5826
12-19A	6	7.8	8	477.8	0.2	5844
12-19A	6	30.3	30.5	500.3	0.2	6276
12-19A	6	63.3	63.5	533.3	0.2	6912
12-19A	6	88.9	89.1	558.9	0.2	7405
12-19A	6	89.3	102.5	559.3	13.2	7412
12-19A	6	102.8	104.2	572.8	1.4	7414
12-19A	6	109.4	109.5	579.4	0.1	7515
12-19A	6	114.5	131.5	584.5	17	7612
12-19A	7	34	34.3	654	0.3	8611
12-19A	7	42	43	662	1	8760
12-19A	7	72.3	83.3	692.3	11	9328
12-19A	7	116.3	116.9	736.3	0.6	9968
12-19A	7	147.4	147.6	767.4	0.2	10559
12-19A	8	18.3	18.5	788.3	0.2	10961
12-16B	1	80	93.5	80	13.5	970
12-16B	1	117	117.8	117	0.8	1266
12-16B	2	58.5	59.5	184.5	1	1709
12-16B	2	88	88.3	214	0.3	1901
	2	94.8	--			
12-16B	3	--	2.5	220.8	25.2	1946
12-16B	3	36.5	66	280	29.5	2449
12-16B	4	2.5	5.5	317	3	2579
12-16B	4	29.5	57	344	27.5	2918
12-16B	4	65.3	65.5	379.8	0.2	3203
12-16B	4	91	91.1	405.5	0.1	3715
12-16B	4	112.6	112.7	427.1	0.1	4161
12-16B	5	75.5	75.6	519	0.1	5847
12-16B	5	84.8	84.9	528.3	0.1	5815

12-16B	5	85.3	85.6	528.8	0.3	5826
12-16B	5	87.2	87.5	530.7	0.3	5844
12-16B	5	109	109.2	552.5	0.2	6276
12-16B	5	121.6	121.8	565.1	0.2	6719
12-16B	5	125.9	126.2	569.4	0.3	6798
12-16B	5	137.3	137.5	580.8	0.2	6912
12-16B	5	142.1	142.9	585.6	0.8	7204
12-16B	5	145.5	145.8	589	0.3	7152
12-16B	5	148.5	148.7	592	0.2	7204
12-16B	6	11.9	15.3	607.4	3.4	7405
12-16B	6	21	62.5	616.5	41.5	7412
12-16B	6	64.5	65.7	660	1.2	7414
12-16B	6	71.4	71.7	666.9	0.3	7515
12-16B	6	75.9	94.5	671.4	18.6	7612
12-16B	7	2.2	2.5	711.2	0.3	8611
12-16B	7	11.4	51.5	720.4	40.1	8760
12-16B	7	79.2	134	788.2	54.8	9328
	1	99	--			
12-15A	2	--	20	99	24.5	970
12-15A	2	54	55.5	157.5	1.5	1266
12-15A	2	110.7	121	214.2	10.3	1709
12-15A	3	19	22	243.5	3	1901
12-15A	3	25	55.5	249.5	30.5	1946
	3	86.5	--			
12-15A	4	--	15	311	56	2449
12-15A	4	22	57.5	376	35.5	2579
	4	78.5	--			
12-15A	5	--	1.5	432.5	55	2918
12-15A	5	10.9	11.2	496.9	0.3	3203
12-15A	5	12.5	15.5	498.5	3	3217
12-15A	5	22.2	22.3	508.2	0.1	3385
12-15A	5	23.3	23.4	509.3	0.1	3410
12-15A	5	24.6	24.8	510.6	0.2	3440
12-15A	5	38	43	524	5	3620
12-15A	5	46.2	46.5	532.2	0.3	3715
12-15A	5	62.8	64.5	548.8	1.7	4161
12-15A	5	125.5	125.7	611.5	0.2	5847
12-15A	6	5.9	6	618.9	0.1	5815
12-15A	6	6.5	7	619.5	0.5	5826
12-15A	6	8	9	621	1	5844
12-15A	6	23.6	23.8	636.6	0.2	6276
12-15A	6	33.5	35.5	646.5	2	6719

12-15A	6	38.5	38.8	651.5	0.3	6798
12-15A	6	48.1	48.4	661.1	0.3	6912
12-15A	6	52	53	665	1	7204
12-15A	6	55	55.3	668	0.3	7152
12-15A	6	56.4	56.5	669.4	0.1	7204
12-15A	6	59.5	63.5	672.5	4	7171
12-15A	6	65.5	73.5	678.5	8	7221

**Supplementary Table 4.** Total inorganic carbon (TIC) of core 13-12C.

Section	Section Depth (cm)	Downcore Depth (cm)	TIC (%)	Age (yr)
1	2	2	3.18	18
1	6	6	2.98	54
1	10	10	3.34	90
1	14	14	3.17	127
1	18	18	3.28	163
1	22	22	3.12	199
1	26	26	3.22	235
1	30	30	2.72	271
1	34	34	3.18	307
1	38	38	3.11	344
1	42	42	3.25	380
1	46	46	2.25	416
1	50	50	2.75	452
1	54	54	2.03	488
1	58	58	2.06	524
1	62	62	1.95	561
1	66	66	1.19	597
1	70	70	1.04	633
1	74	74	1.13	669
2	3	82	0.58	742
2	7	86	0.82	778
2	11	90	0.63	814
2	15	94	0.78	850
2	19	98	0.70	886
2	23	102	0.81	922
2	27	106	0.81	959
2	31	110	0.82	995
2	35	114	0.75	1031
2	39	118	0.76	1067
2	43	122	0.63	1103
2	47	126	0.73	1139
2	50	129	0.81	1167
2	52.5	131.5	1.20	1189
2	55	134	2.77	1212
2	57.5	136.5	2.61	1234
2	60	139	2.20	1257
2	63	142	1.71	1286
2	67	146	2.62	1326
2	71	150	3.18	1365
2	75	154	3.02	1405



2	79	158	3.12	1445
2	83	162	2.84	1485
2	87	166	3.33	1524
2	91	170	2.08	1564
2	94	173	2.30	1594
3	2.5	176.5	0.31	1628
3	6	180	0.63	1661
3	9	183	0.35	1689
3	11.5	185.5	0.30	1713
3	14	188	0.47	1737
3	16.5	190.5	0.33	1761
3	19	193	0.42	1784
3	22	196	0.58	1813
3	24.5	198.5	0.33	1836
3	27	201	0.35	1860
3	30	204	0.70	1889
3	32.5	206.5	1.63	1917
3	35	209	0.89	1955
3	38	212	2.12	2049
3	42	216	4.16	2175
3	46	220	4.07	2301
3	50	224	4.57	2427
3	54	228	4.10	2547
3	62	236	4.32	2784
3	66	240	3.83	2903
3	70	244	2.91	3073
3	74	248	3.49	3251
3	78	252	2.06	3429
3	82	256	1.52	3606
3	86	260	1.12	3772
3	90	264	0.33	3887
3	94	268	0.12	4002
3	98	272	0.09	4118
3	102	276	0.15	4214
3	106	280	0.07	4300
3	110	284	0.14	4385
3	118	292	0.17	4556
4	2	300	0.18	4727
4	10	308	0.21	4897
4	18	316	0.23	5068
4	26	324	0.20	5239
4	34	332	0.31	5410
4	42	340	0.53	5581

4	50	348	0.43	5752
4	58	356	0.34	5935
4	66	364	0.42	6139
4	74	372	0.36	6385
4	82	380	0.23	6719
4	90	388	0.31	6897
5	1	396.5	0.69	7154
5	9	404.5	0.37	7402
5	17	412.5	0.11	7636
5	25	420.5	0.17	7828
5	33	428.5	0.23	8020
5	41	436.5	0.21	8212
5	49	444.5	0.17	8404
5	57	452.5	0.20	8596
5	65	460.5	0.26	8779
5	73	468.5	0.18	8974
5	81	476.5	0.23	9168
5	89	484.5	0.17	9355
6	4	494.5	0.11	9548
6	12	502.5	0.08	9702
6	20	510.5	0.16	9856
6	28	518.5	0.17	10013
6	36	526.5	0.18	10176
6	44	534.5	0.16	10338
6	52	542.5	0.24	10501
6	60	550.5	0.23	10664
6	68	558.5	0.22	10827
6	76	566.5	0.22	10975
6	84	574.5	0.11	11056
6	92	582.5	0.10	11137
6	100	590.5	0.09	11217
6	108	598.5	0.04	11298
6	116	606.5	0.03	11379
7	8	617.5	0.02	11490
7	16	625.5	0.02	11571
7	24	633.5	0.07	11652
7	32	641.5	0.06	11732
7	40	649.5	0.17	11813
7	48	657.5	0.24	11894
7	56	665.5	0.31	11975
7	64	673.5	0.56	12056
7	72	681.5	1.47	12136
7	76	689.5	8.55	12192

## **Supplementary References**

Danzeglocke, U., Jöris, O., and Weninger, B., 2013, CalPal-2007<sup>online</sup>: <http://www.calpal-online.de/> (accessed June 2013).

Zal, H., 2014, Kinematics and dynamics of the Kivu rift system from seismic anisotropy, seismicity, and structural analyses [Master Thesis]: Rochester, USA, University of Rochester, 62p.

## **CHAPTER 2:**

### **Millennial-scale extreme hydrologic events in equatorial West Africa linked to North**

#### **Atlantic climate**

Xuewei Zhang<sup>1\*</sup>, Christopher A. Scholz<sup>1</sup>, Nicholas P. McKay<sup>2</sup>, Timothy M. Shanahan<sup>3</sup>

Clifford W. Heil<sup>4</sup>, Jonathan T. Overpeck<sup>5</sup>, John King<sup>4</sup>, John Peck<sup>6</sup>

<sup>1</sup>Department of Earth Sciences, Syracuse University, Syracuse, New York 13244, USA

<sup>2</sup>School of Earth Sciences and Environmental Sustainability, North Arizona University,

Flagstaff, Arizona 86011, USA

<sup>3</sup>Jackson School of Geosciences, The University of Texas at Austin, Austin, Texas 78712, USA

<sup>4</sup>Graduate School of Oceanography, University of Rhode Island, Narragansett, Rhode Island

02882, USA

<sup>5</sup>Department of Geosciences, University of Arizona, Tucson, Arizona 85721, USA

<sup>6</sup>Department of Geology and Environmental Science, University of Akron, Akron, Ohio 44325,

USA

\*E-mail: xzhang39@syr.edu

## **Abstract**

Pronounced millennial-scale air temperature oscillations recorded in Greenland ice cores referred to as Dansgaard–Oeschger events, and episodes of massive iceberg discharges into the North Atlantic ocean known as Heinrich events punctuated the last glaciation. In the low latitudes, these millennial-scale events were reflected by altered patterns of precipitation, and may have overridden orbital forcing in modulating regional hydrologic cycles. However, little is known about the relationship between hydrologic extremes and northern high-latitude climate variability. Here, we reconstructed extreme hydrologic events in equatorial West Africa over the past 65 k.y., using flood-introduced turbidites, total organic carbon, carbon isotopes, and seismic reflection data from Lake Bosumtwi, Ghana. Our data suggest that on millennial time scales, extreme rainfall events were linked to Dansgaard–Oeschger interstadials, whereas exceptional drought events were associated with North Atlantic cooling during Heinrich events.

## **Introduction**

During the last glacial period, the North Atlantic region experienced two types of millennial-scale climate events, known as Dansgaard–Oeschger (D–O) oscillations, characterized by abrupt shifts between cold stadial conditions and relatively warm interstadial conditions, and Heinrich events, characterized by periods of massive iceberg discharges<sup>1</sup>. First observed from Greenland ice cores<sup>2</sup> and North Atlantic deep-sea sediments<sup>1,3,4</sup>, D–O and Heinrich events reflect reorganizations of the ocean–atmosphere circulation<sup>5-10</sup>, and their global teleconnections have been identified in widespread proxy records<sup>11-19</sup>. In the tropics and subtropics, millennial-scale fluctuations in hydrologic cycles were linked to northern high-latitude climate variability, with enhanced monsoonal precipitation occurring during D–O interstadials and reduced rainfall associated with Greenland stadials<sup>13,15-19</sup>, some of which coincided with Heinrich events. However, whether hydrologic extremes in the low latitudes, such as exceptional floods and droughts, were linked to North Atlantic climate remains poorly constrained, because of the lack of long, continuous, and well-dated records that can capture the variability of extreme hydrologic events. In this study, we analyzed sediments from Lake Bosumtwi for reconstruction of exceptional floods and droughts in equatorial West Africa.

## **Background to Lake Bosumtwi**

Lake Bosumtwi (6°30'N, 1°25'W; Fig. 1) is ideally located for reconstructing paleohydrologic changes in the West African Monsoon (WAM) regime<sup>20</sup>. The lake occupies a

1.08 Ma meteorite impact crater in the forested tropical lowland of southern Ghana, where precipitation is primarily controlled by the seasonal migration of the Intertropical Convergence Zone (ITCZ; Extended Data Fig. 1). During Northern Hemisphere summer months, the ITCZ and associated rain belt migrate to the north of Lake Bosumtwi, and the moisture-laden southeasterly winds bring heavy monsoonal precipitation to study site; during winter months, the ITCZ is positioned to the south of the lake, and dry, dust-laden northeasterly winds dominate over southern Ghana.

With a maximum water depth of ~75 m, Lake Bosumtwi is permanently stratified with a well-mixed epilimnion and anoxic hypolimnion below 15–18 m depth<sup>21</sup>. This results in the preservation of finely-laminated sediment varves that allow for high-resolution paleoclimatic and paleohydrologic reconstructions<sup>22</sup>, including variations in the WAM. Due to the hydrologically-closed nature of the lake basin and its isolation from groundwater table<sup>21</sup>, the water budget of Lake Bosumtwi is extremely sensitive to the balance between precipitation and evaporation<sup>21,23,24</sup>. Previous investigations have demonstrated that Lake Bosumtwi experienced profound hydrologic changes during the late Pleistocene and Holocene, as recorded by seismic and sedimentological lake-level indicators<sup>25-28</sup>, magnetic dust properties<sup>22,29</sup>, elemental abundances<sup>20,29</sup>, as well as hydrogen<sup>30</sup>, carbon<sup>31,32</sup>, and oxygen<sup>20,29</sup> isotopes measured from terrestrial leaf waxes, organic matter, and authigenic carbonates. Although these proxies provide insight into the temporal occurrence and magnitude of severe drought events in equatorial West Africa, they fail to record exceptional flood events. The dynamics of both types of extreme

hydrologic events recorded in the sediments of Lake Bosumtwi reflect the degree of variability in the WAM.

### **Paleohydrologic Proxies for Reconstruction of Exceptional Floods and Droughts**

We generated a multi-proxy record of exceptional floods and droughts in Equatorial West Africa, using annually laminated<sup>20,29</sup> sediment cores BOS04-5B and BOS04-5C, both recovered from the deep water drill site 5 of the ICDP (International Continental Scientific Drilling Program) Lake Bosumtwi Drilling Project (Fig. 1). Applying a Bayesian approach, a combination of radiocarbon, optically stimulated luminescence, and U-series dating as well as paleomagnetic excursions was used to generate a geochronology for the upper 150 k.y. of sedimentation at Lake Bosumtwi<sup>33,34</sup>. This study focuses on the upper 65 k.y. (or ~34 m) of the sediment record, where relatively small uncertainties of the geochronology enable correlations between paleohydrologic records of Lake Bosumtwi and well-dated records of marine sediment cores and ice cores.

We use flood-introduced turbidites (Extended Data Table 1) observed in the sediment cores for reconstruction of exceptional precipitation events. Using a bin width of 100 yr, time series of accumulation rate and frequency of the turbidites were generated to reflect variations in magnitude and frequency of exceptional floods. Exceptional drought events were identified by the presence of unconformities on high-resolution air gun and CHIRP (compressed high-intensity radar pulse) seismic reflection profiles, or were inferred from  $\delta^{13}\text{C}$  (Extended Data



Table 2) measured from bulk organic sediments. Although macrofossil and palynological studies suggest that the relative proportions of C<sub>3</sub> and C<sub>4</sub> plants have varied considerably in tropical West Africa in the late Pleistocene and Holocene<sup>31,32,35</sup>, comparisons of carbon isotope ratios in bulk organic matter and fossil grass epidermal fragments from Lake Bosumtwi indicate that  $\delta^{13}\text{C}$  measured from bulk organic sediments is dominated by hydrologic processes within the lake<sup>32</sup>. Previous studies suggest that the dissolved inorganic carbon (DIC) reservoir of Lake Bosumtwi tends to be enriched in <sup>13</sup>C during lake-level lowstands, as indicated by the markedly positive  $\delta^{13}\text{C}$  in primary carbonates<sup>36</sup>. During low water periods when combined effects of high pH and elevated salinity reduce dissolved CO<sub>2</sub> to very low levels, HCO<sub>3</sub><sup>-</sup>-based photosynthesis in a <sup>13</sup>C-enriched DIC reservoir may have led to the production of organic matter with markedly high  $\delta^{13}\text{C}$  (ref. 31). A highly positive  $\delta^{13}\text{C}$  value (-11.9‰) in an algal crust from the littoral zone of Lake Bosumtwi indicates that HCO<sub>3</sub><sup>-</sup>-based metabolism may be occurring in the present lake<sup>31</sup>. Thus, sediment intervals having markedly positive  $\delta^{13}\text{C}$  are interpreted as deposited during pronounced lake-level lowstands under severe arid conditions in equatorial West Africa, whereas intervals showing highly enriched  $\delta^{13}\text{C}$  are interpreted as accumulated during more humid conditions. The record of total organic carbon (TOC) is interpreted to reflect lake-level; a deep lake with anoxic bottom waters favors organic carbon preservation by preventing organic matter degradation, while a shallow, well-mixed lake does the opposite. However, other variables, such as insolation-driven changes in primary productivity, may also influence the accumulation of TOC.

## **Turbidites and Source of Turbidity Flows**

Frequent occurrences of turbidites preserved in the late Quaternary sediments of Lake Bosumtwi have been described in a number of studies<sup>22,25,29,37</sup>. Here, we present a 65 k.y. record of turbidites, and discuss their origins and usefulness as indicators of past environmental changes. Intercalated with finely-laminated muds or massive, sapropelic muds, over 300 turbidite layers that are thicker than 1 mm were identified in the upper 65 k.y. of the lake sediments (Extended Data Figs. 2 & 3; Extended Data Table 1), on average approximately 1 event every 200 years; their thickness ranges from 1 to 168 mm, with an average of 5.5 mm and a median of 1.3 mm. The turbidite layers contain less organic matter, and are coarser and denser than the surrounding laminated muds (Extend Data Fig. 4). The moderately- to well-sorted millimeter-thick turbidites are fine- to medium silt-sized, consist of primarily quartz and feldspar grains, and therefore display a distinct light-gray color; centimeter- to decimeter-thick turbidites are massive, medium- to coarse silt-sized, moderately sorted, and are characterized by a light-gray cap<sup>29</sup> (Extend Data Figs. 5–7).

The centimeter- to decimeter-thick turbidites commonly display reverse-to-normal grading (Extended Data Fig. 7), typical of hyperpycnal river flow deposits during floods, that records the waxing and waning phases of discharge<sup>38</sup>. Although sediment failure on slopes, usually triggered by earthquakes, commonly initiates turbidity flows in marine and lake basins<sup>39</sup>, it is not likely a trigger of frequent turbidity currents in Lake Bosumtwi, which is situated on the tectonically stable West African craton. Due to the steep gradient of the crater wall and the small size of the

lake basin, any mass transport deposits that resulted from failed slopes would leave a depositional record in the center of the basin. However, over the interval presented here, we find no evidence of mass transport deposits even in the sediment cores recovered in deep water, nor any sediment failure-related structures on the decimeter- to meter-resolution seismic reflection profiles. We therefore interpret the turbidites as sourced by hyperpycnal river flows during exceptional floods.

The millimeter-thick turbidites are interpreted as deposited from non-erosive turbidity flows sourced by less extreme flood events. During such events, there is little entrainment of previously deposited sediments (including aquatic and terrestrial organic matter) into the turbidity flows as they travel downslope on the lake floor. This may explain why the millimeter-thick turbidites comprise predominantly siliciclastic mineral grains derived from onshore drainages, but contain little organic matter. In contrast, the centimeter- to decimeter-thick turbidites have abundant aquatic and terrestrial organic matter (Extended Data Fig.6), and some show rip-up clasts; they are interpreted as deposited by erosive turbidity currents during extremely heavy rainfall events. The thicker turbidites display a light-gray cap<sup>29</sup> that is texturally and compositionally similar to the light-colored thin turbidites (Extended Data Fig.5); the light-gray caps are interpreted as deposited during the final stage of extreme turbidity flow events, when the flows became non-erosive in response to diminishing flood discharges.

## Exceptional Rainfall Events

Over the past 65 k.y., turbidite sedimentation at Lake Bosumtwi followed the millennial-scale climate events in  $\delta^{18}\text{O}$  records of Greenland ice cores<sup>40</sup> and sea surface temperature (SST) records of the North Atlantic ocean<sup>41</sup>. Peak accumulation rate and frequency of the flood-sourced turbidites generally occurred during D–O interstadials (Fig. 2), indicating that variations in magnitude and frequency of exceptional rainfall events in equatorial West Africa were coupled to millennial-scale climate instability of the northern high latitudes. This is consistent with previous studies of the WAM. Geochemical and isotopic analyses of marine sediments from the Gulf of Guinea in the eastern equatorial Atlantic suggest that in the past ~155 k.y., centennial- to millennial-scale variations of sea surface salinity (SSS), a proxy for riverine freshwater input, were synchronous with northern high-latitude stadials and interstadials<sup>16</sup>. Low SSS in the Gulf of Guinea, due to high riverine freshwater input from enhanced precipitation over the drainage basin of the Niger and Sanaga Rivers, is linked to interstadials<sup>16</sup>. This suggests that high-magnitude and high-frequency flood events occurred in the wet phases of tropical West Africa.

The correspondence between the temporal occurrence of turbidite events at Lake Bosumtwi and wet climate intervals in equatorial West Africa is also evident in the paleohydrologic records of the lake. Peak turbidite sedimentation correlates with intervals of markedly negative  $\delta^{13}\text{C}$  values (Fig. 2), suggesting that the flood-sourced turbidites were deposited during lake-level highstands under humid conditions. A well-constrained lake-level curve<sup>25-27</sup>, which extends back to ~16.5 k.a., was reconstructed using a variety of lake-level indicators, including seismic

unconformities, root-rich exposure surfaces, as well as previous beach and near-shore deposits that are now exposed on the lake shore (Fig. 2). Between ~16.5 ka and present, the temporal occurrence of the turbidites observed in the sediment cores correlates with lake-level highstands, although their accumulation rate and frequency appear not to scale with lake elevation. This is likely due to greatly reduced drainage basin area (as a result of elevated lake-levels) and amplified vegetation feedback during the African Humid Period (AHP, 14.8–5.5 ka; [ref. 42](#)), when water-level of Lake Bosumtwi was ~20–120 m higher than present<sup>25,27</sup> and dense vegetation under the wettest climate over the past 520 k.y. ([ref. 35](#)) limited the amount of sediments available during flood events.

Insolation forcing may also have contributed to the magnitude of rainfall extremes. Although the imprints of northern high-latitude millennial-scale climate events are clearly expressed in the TOC and reconstructed water-level records<sup>25,27</sup> of Lake Bosumtwi, long-term variations of TOC and lake-level seem to followed local summer insolation (Extended Data Fig. 8). Had it not been the flooding of drainage basins on the cater wall and land surface feedback during the AHP, accumulation rate of the flood-sourced turbidites would be much higher than that is preserved in the sediment record, and its long-term variations would also generally follow orbital-scale changes in summer insolation, at least between ~50 k.a. and present (Extended Data Fig. 8). Compared to the magnitude of exceptional rainfall events, the frequency of rainfall extremes seems to be less dependent on orbital insolation.

## Exceptional Drought Events

Severe drought events lasting for periods ranging from decades to millennia have been a persistent feature in the late Pleistocene and Holocene sediment record of Lake Bosumtwi, and have been linked to northern high-latitude climate and changes in Atlantic SST<sup>20,22,29,32,33</sup>. Here, we extend the record of prominent drought events preserved in the sediments of Lake Bosumtwi to 65 k.a.

The bulk organic-based  $\delta^{13}\text{C}$  record of Lake Bosumtwi, which we interpreted as a proxy for lake-level and humidity, is remarkably similar to the alkenone-based North Atlantic sea surface temperature (SST) record from marine sediment core MD94-2042<sup>41</sup>, suggesting that over the past 65 k.y., the hydroclimatic variability in equatorial West Africa is strongly linked the North Atlantic climate. Exceptional drought events, indicated by markedly positive  $\delta^{13}\text{C}$ , low TOC, and reduced or absent turbidite sedimentation, occurred during North Atlantic cooling, especially during Heinrich stadials (Fig. 2). Some of these events caused large-scale unconformities. The most pronounced drought event over the past 65 k.y. occurred between ~65 and 62 ka, and is probably linked to Heinrich event 6 (H6). This event correlates with a lake-wide unconformity on both the CHIRP and single-channel air gun seismic reflection profiles, and in the sediment cores, it is characterized by ~1.5 m thick structureless dense clay deposits (Fig. 3; Extended Data Fig. 2). During this event, Lake Bosumtwi was ~105 m below present lake-level, and possibly dried out for brief periods.

The presence of shallow burial gases (Extended Data Fig. 2) in the lake sediments limits the use of the decimeter-resolution CHIRP seismic data for identification of lake-level lowstands. However, within the resolution of the single-channel air gun seismic data, at least another two pronounced drought events are observed. An onlap seismic surface is observed ~70 m below present lake-level. Seismic–sediment core integration suggests that this event occurred between ~48.5 and 47.5 ka, and probably correlates with H5 (Fig. 3). Another seismic unconformity indicated by stratal truncations that are ~55–70 m below present lake-level correlates with a rootlet-rich exposure surface in a piston sediment core recovered from ~60 m water depth<sup>26</sup>; this event was dated to ~16.5 ka<sup>26</sup>, and is linked to H1 (Figs. 2 & 3). Severe drought events also occurred during the Younger Dryas (YD or H0) and the 8.2 ka cold event<sup>44</sup>. These two events are registered in the lake-level record of Lake Bosumtwi<sup>25,27</sup>, and the latter correlates with period of sharply increased delivery of Sahara- and Sahel-derived dusts by strengthened NE trade wind under arid conditions<sup>22</sup>.

### **North Atlantic Forcing of West African Hydroclimate**

The strength of the North Atlantic meridional overturning (NAMO) circulation is widely believed to affect West African hydroclimate and vegetation<sup>45-48</sup>. Previous studies have suggested that millennial-scale arid conditions in tropical and subtropical West Africa are associated with slowing of the NAMO circulation during Heinrich stadials<sup>45-48</sup>, whereas relatively humid conditions with expansions of C<sub>3</sub> vegetation in the Sahara and Sahel region

correlate with strengthened NAMO circulation during D-O interstadials<sup>46,47</sup>. Geochemical proxies for deep-sea ventilation<sup>6,7,49,50</sup> and climate modeling<sup>8</sup> suggest that the NAMO circulation operates in distinctively different modes during Heinrich stadials versus during D-O interstadials. A large freshwater input due to massive iceberg discharges during Heinrich events may temporally switch off the North Atlantic Deep Water formation, leading to the collapse of the NAMO circulation<sup>8,10</sup>. Modeling simulations indicate that weakening of NAMO circulation induces surface cooling of the North Atlantic, a southward shift of the WAM trough (i.e. the ITCZ), and an intensification and southward expansion of the African Easterly Jet, leading to arid conditions in the entire West African region<sup>45</sup>, including the Guinea coast where Lake Bosumtwi is located.

Our data support the climate modeling results. The organic-based  $\delta^{13}\text{C}$  record of Lake Bosumtwi is correlated with the  $\delta^{13}\text{C}$  records of benthic foraminifera from marine sediments core MD95-2042 (refs 41,50) and GeoB7920-2 (ref. 46) in the North Atlantic. Highly positive  $\delta^{13}\text{C}$  in bulk organic matter of Lake Bosumtwi, which implies exceptional drought events in equatorial West Africa due to reduced monsoonal precipitation, correlates with markedly low  $\delta^{13}\text{C}$  in benthic foraminifera of the North Atlantic, which indicates reduced NAMO circulation<sup>41,46</sup> (Fig. 4). Conversely, over the past 65 k.y., high-magnitude and high-frequency extreme rainfall events in equatorial West Africa generally correspond to D-O interstadials when NAMO circulation was strengthened (refs 41,46,50). This implies that during the D-O interstadials of the last glaciation, the ITCZ summer position was located to the north of Lake Bosumtwi, and relatively humid



conditions prevailed in equatorial West Africa due to strengthened WAM. Simulations of abrupt millennial-scale climate changes suggest that surface air temperature in the tropical North Atlantic was 0.5 – 1 °C and 0.5 – 1.5 °C warmer during D-O interstadials than during stadial conditions and Heinrich events<sup>8</sup>. Both satellite observations and model simulations investigating the response of tropical precipitation to atmospheric warming suggest a direct link between rainfall extremes and surface air temperature, with extreme precipitation events increasing during warm periods and decreasing during cold periods<sup>51</sup>. This amplification of rainfall extremes by atmospheric warming may explain the general correspondence between exceptional rainfall events in equatorial West Africa and D-O oscillations in the northern high latitudes.

### **Implications for Future Research**

Much of West Africa has recently experienced severe droughts and floods. For example, the Sahel drought beginning in the 1960s and continuing into the 1990s endangered millions of lives, and contributed significantly to regional geopolitical instability<sup>52</sup>. Since the 1990s, catastrophic floods have frequently occurred in the Sahel and wider West African region, with those occurred in the years of 1995, 1998, and 1999 each affecting more than one million people in five, eight, and eleven countries<sup>53</sup>. Better knowledge of natural, long-term variability of floods and droughts in tropical West Africa is therefore of political and socioeconomic importance. The flood-introduced turbidites of Lake Bosumtwi, together with the bulk organic-based  $\delta^{13}\text{C}$  and seismic reflection data, provide new insights into the dynamics of the WAM, suggesting that hydrologic

extremes, more severe than the recent floods and droughts in West Africa, are characteristics of the WAM, and are linked to millennial-scale climate instability of the North Atlantic. This study and previous investigations<sup>54,55</sup> demonstrate that flood-sourced turbidites preserved in lake (and ocean) basins are valuable indicators of tropical hydrological changes.

## **Methods**

### ***Layer Identification, Time series, and Particle Size of Turbidites***

Both core images and X-ray radiographs were used for identification of turbidites in drill cores BOS04-5B and BOS04-5C. Layer identification was supplemented by smear slide and grain size analyses. Submillimeter- to millimeter-thick turbidites display distinctive light-gray color, and are denser than the surrounding laminated muds on the X-radiographs. Centimeter- to decimeter-thick turbidites can be readily distinguished from the surrounding muds by their high density and massive sedimentary structure; these thicker layers display a distinctive light-gray cap<sup>29</sup>, and commonly show reverse-to-normal grading, although normal grading is also observed.

Numerous submillimeter-thick microturbidites are present in the studied interval. Only layers thicker than 1 mm were used for times series analysis. After applying the geochronology<sup>33,34</sup> to the identified layers, time series of accumulation rate and frequency of the turbidites were generated, using a bin width of 100 yr. Core BOS04-5C was used to bridge gaps (due to sediment loss during drilling) in core BOS04-5B.

Grain size of the sampled centimeter- to decimeter-thick turbidites were analyzed with a Beckman Coulter LS230 Laser Diffraction Particle Size Analyzer, which measures sediment size ranging from 0.04 to 2000  $\mu\text{m}$ . Instrumental performance was verified by running control samples. Inorganic carbon, organic carbon, and biogenic silica were removed before running the turbidite samples for grain size analysis.

### ***TOC and Carbon Isotopes***

Wet sediments were sampled every 30 cm (~500 yr resolution) from core BOS04-5B. The samples were dried, crushed, weighed, and acidified to remove inorganic carbon using acid fumigation for 48 hours. The samples were desiccated for another 48 hours prior to analysis for TOC and  $\delta^{13}\text{C}$ . The weight percentage and  $\delta^{13}\text{C}$  values of TOC were measured at the Environmental Science Stable Isotope Laboratory (EaSSIL) at the State University of New York, College of Environmental Science and Forestry (SUNY-ESF), using a Costech ECS41010 elemental analyzer linked via a ThermoFinnigan Conflo III interface to a ThermoFinnigan Delta XL Plus stable isotope mass spectrometer (EA-IRMS). The accuracy and precision of stable isotope measurements were verified using National Institutes of Standards and Technology RM8573 ( $\delta^{13}\text{C} = -26.4 \pm 0.1\text{‰}$ ) and RM8574 ( $\delta^{13}\text{C} = 37.6 \pm 0.2\text{‰}$ ). Daily precision of the instrument was verified by repeated analyses of internal laboratory standards including acetanilide ( $\delta^{13}\text{C} = -29.9 \pm 0.2\text{‰}$ ) and peach leaves ( $\delta^{13}\text{C} = -25.2 \pm 0.2\text{‰}$ ) during the sample runs.

## **Acknowledgements**

The Lake Bosumtwi drilling project was funded by the U.S. National Science Foundation and the International Continental Scientific Drilling Project. Support for X.Z. and sediment analyses was provided by the Syracuse University Industrial Associates Program. Analysis of geophysical data was completed using software provided to Syracuse University through the Landmark Graphics University Partnership Program.

## References

1. Bond, G. et al. Correlations between climate records from North Atlantic sediments and Greenland ice. *Nature* 365, 143–147 (1993).
2. Dansgaard, W. et al. Evidence for general instability of past climate from a 250-kyr ice-core record. *Nature* 364, 218–220 (1993).
3. Heinrich, H. Origin and consequences of cyclic rafting in the Northeast Atlantic Ocean during the past 130,000 years. *Quat. Res.* 29, 142–152 (1988).
4. Bond, G. et al. Evidence for massive discharges of icebergs into the North Atlantic ocean during the last glacial period. *Nature* 360, 245–249 (1992).
5. Broecker, W. S., Bond, G., Klas, M., Bonani, G. & Wolfi, W. A salt oscillator in the glacial North Atlantic? 1. The concept. *Paleoceanography* 5, 469–477 (1990).
6. Sarnthein, M. et al. Changes in east Atlantic deepwater circulation over the last 30,000 years: eight time slice reconstructions. *Paleoceanography* 9, 209–267 (1994).
7. Alley, R. B. & Clark, P. U. The deglaciation of the Northern Hemisphere: a global perspective. *Annu. Rev. Earth Planet. Sci.* 27, 149–182 (1999).
8. Ganopolski, A. & Rahmstorf, S. Rapid changes of glacial climate simulated in a coupled climate model. *Nature* 409, 153–158 (2001).
9. Rahmstorf, S. Ocean circulation and climate during the past 120,000 years. *Nature* 419, 207–214 (2002).

10. Broecker, W. S. Does the trigger for abrupt climate change reside in the ocean or in the atmosphere?. *Science* 300, 1519–1522 (2003).
11. Behl, R. J. & Kennett, J. P., Brief interstadial events in the Santa Barbara basin, NE Pacific, during the past 60 kyr. *Nature* 379, 243–246 (1996).
12. Schulz, H., von Rad, U. & Erlenkeuser, H. Correlation between Arabian Sea and Greenland climate oscillations of the past 110,000 years. *Nature* 393, 54–57 (1998).
13. Peterson, L. C., Haug, G. H., Hughen, K. A. & Röhl, U. Rapid changes in the hydrologic cycle of the tropical Atlantic during the last glacial. *Science* 290, 1947–1951 (2000).
14. Genty, D. et al. Precise dating of Dansgaard-Oeschger oscillations in western Europe from stalagmite data. *Nature* 421, 833–837 (2003).
15. Cruz, F. W. et al. Insolation-driven changes in atmospheric circulation over the past 116,000 years in subtropical Brazil. *Nature* 434, 63–66 (2005).
16. Weldeab, S., Lea, D. W., Schneider, R. R. & Andersen, N. 155,000 years of West African Monsoon and ocean thermal evolution. *Science* 316, 13033–1307 (2007).
17. Wang, Y. et al. Millennial- and orbital-scale changes in the East Asian Monsoon over the past 224,000 years. *Nature* 451, 1090–1093 (2008).
18. Mosblech, N. A. S. et al. North Atlantic forcing of Amazonian precipitation during the last ice age. *Nature Geoscience* 5, 817–820 (2012).
19. Deplazes, G. et al. Links between tropical rainfall and North Atlantic climate during the last glacial period. *Nature Geoscience* 6, 213–217 (2013).

20. Shanahan, T. M. et al. Atlantic forcing of persistent drought in West Africa. *Science* 324, 377–380 (2009).
21. Turner, B. F., Gardner, L. R. & Sharp, W. E. The hydrology of Lake Bosumtwi, a climate-sensitive lake in Ghana, West Africa. *J. Hydrol.* 183, 243–261(1996).
22. Peck, J. A., et al. A magnetic mineral record of Late Quaternary tropical climate variability from Lake Bosumtwi, Ghana. *Palaeogeogr. Palaeoclimatol. Palaeoecol.* 215, 37–57 (2004).
23. Shanahan, T. M., Overpeck, J. T., Sharp, W. E., Scholz, C. A. & Arko, J. A. Simulating the response of a closed-basin lake to recent climate changes in tropical West Africa (Lake Bosumtwi, Ghana). *Hydrol. Process.* 21, 1678–1691 (2007).
24. Shanahan, T. M., et al. Abrupt changes in the water balance of tropical West Africa during the late Quaternary. *J. Geophys. Res.* 113, D12108, doi: 10.1029/2007JD009320 (2008a).
25. Talbot, M. R. & Delibrias, G. A new late-Holocene water-level curve for Lake Bosumtwi, Ghana. *Earth Planet. Sci. Lett.* 47, 336–344 (1980).
26. Brooks, K., et al. Late-Quaternary lowstands of lake Bosumtwi, Ghana: evidence from high-resolution seismic-reflection and sediment-core data. *Palaeogeogr. Palaeoclimatol. Palaeoecol.* 216, 235–249 (2005).
27. Shanahan, T. M. et al. Paleoclimatic variations in West Africa from a record of late Pleistocene and Holocene lake level stands of Lake Bosumtwi, Ghana. *Palaeogeogr. Palaeoclimatol. Palaeoecol.* 242, 287–302 (2006).

28. Scholz, C. A. et al. East African megadroughts between 135 and 75 thousand years ago and bearing on early-modern human origins. *Proc. Natl. Acad. Sci. U.S.A.* 104, 16416–16421 (2007).
29. McKay, N. P. A multidisciplinary approach to the late Quaternary paleoclimatology with an emphasis on sub-Saharan West Africa and the last interglacial period (Ph.D. Dissertation, The University of Arizona, Tucson, 2012).
30. Shanahan, T. M. et al. The time-transgressive demise of the African Humid Period. *Nature Geoscience*, in review.
31. Talbot, M. R. & Johannessen, T. A high resolution paleoclimatic record for the last 27,000 years in tropical West Africa from the carbon and nitrogen isotopic composition of lacustrine organic matter. *Earth Planet. Sci. Lett.* 110, 23–37 (1992).
32. Beuning, K. R. M., Talbot, M. R., Livingstone, D. A. & Schmukler, G. Sensitivity of carbon isotopic proxies to paleoclimatic forcing: A case study from Lake Bosumtwi, Ghana, over the last 32,000 years. *Global Biogeochem. Cy.* 17, doi: 10.1029/2003GB002072 (2003).
33. Shanahan, T. M. et al. Late Quaternary sedimentological and climate changes at Lake Bosumtwi Ghana: new constraints from laminae analysis and radiocarbon age modeling. *Palaeogeogr. Palaeoclimatol. Palaeoecol.* 361–362, 49–60 (2012).
34. Shanahan, T. M., et al. Age models for long lacustrine sediment records using multiple dating approaches – an example from Lake Bosumtwi, Ghana. *Quat. Geochronol.* 15, 47–60 (2013).



35. Miller, C. A. & Gosling, W. D. Quaternary forest associations in lowland West Africa. *Quat. Sci. Rev.* 84, 7–25 (2014).
36. Talbot, M. R. & Kelts, K. Primary and diagenetic carbonates in the anoxic sediments of Lake Bosumtwi. *Geology* 14, 912–916 (1986).
37. Shanahan, T. M., et al. The formation of biogeochemical laminations in Lake Bosumtwi, Ghana, and their usefulness as indicators of past environmental changes. *J. Paleolimnol.* 40, 339–355 (2008b).
38. Mulder, T., Migeon, S., Savoye, B. & Jouanneau, J. -M. Twentieth century floods recorded in the deep Mediterranean sediments: *Geology* 29, 1011–1014 (2001).
39. Meiburg, E. & Kneller, B. Turbidity currents and their deposits: *Annu. Rev. Fluid Mech.* 42, 135–157 (2009).
40. Johnsen, S. J. et al. Oxygen isotope and palaeotemperature records from six Greenland ice-core stations: Camp Century, Dye-3, GRIP, GISP2, Renland and NorthGRIP. *J. Quat. Sci.* 16, 299–307 (2001).
41. Bard, E. Climate shock: abrupt changes over millennial time scales. *Phys. Today* 55, 32–38 (2002).
42. deMenocal, P. Abrupt onset and termination of the African Humid Period: rapid climate responses to gradual insolation forcing. *Quat. Sci. Rev.* 19, 347–361 (2000).
43. Scholz, C. A. et al. Pronounced central uplift identified in the Bosumtwi impact structure, Ghana, using multichannel seismic reflection data. *Geology* 30, 939–942 (2002).

44. Alley, R. B., Mayewski, P. A., Stuiver, M., Taylor, K. C. & Clark, P. U. Holocene climate instability: A prominent, widespread event 8200 yr ago. *Geology* 25, 483–486 (1997).
45. Mulitza, S. et al. Sahel megadroughts triggered by glacial slowdowns of Atlantic meridional overturning. *Paleoceanography* 23, PA4206, doi:10.1029/2008PA001637 (2008).
46. Tjallingii, R. et al. Coherent high- and low-latitude control of the northwest African hydrologic balances. *Nature Geoscience* 1, 670–675 (2008).
47. Castañeda I. S. et al. Wet phases in the Sahara/Sahel region and human migration patterns in North Africa. *Proc. Natl. Acad. Sci. U.S.A.* 106, 20159–20163 (2009).
48. Itambi, A. C., von Dobeneck, T., Mulitza, S., Bickert, T. & Heslop, D. Millennial-scale northwest African droughts related to Heinrich events and Dansgaard-Oeschger cycles: Evidence in marine sediments from offshore Senegal. *Paleoceanography* 24, PA1205, doi: 10.1029/2007PA001570 (2009).
49. McManus, J. F., Francois, R., Gherardi, J.-M., Keigwin, L. D. & Brown-Leger, S. Collapse and rapid resumption of Atlantic meridional circulation linked to deglacial climate changes. *Nature* 428, 834–837 (2004).
50. Shackleton, N. J. & Hall, M. A., Phase relationships between millennial-scale events 64,000–24,000 years ago. *Paleoceanography* 15, 32–38 (2002).
51. Allan, R. P. & Soden, B. J. Atmospheric Warming and the Amplification of Precipitation Extremes. *Science* 321, 1481–1484 (2008);

52. Hulme, M. Climatic perspectives on Sahelian desiccation: 1973-1998. *Global Environmental Change* 11, 19–29 (2001)
53. Tschakert, P., Sagoe, R., Ofori-Darko, G. & Codjoe, S. N. Floods in the Sahel: an analysis of anomalies, memory, and anticipatory learning. *Climatic Change* 103, 471–502 (2010).
54. Noren, A. J., Bierman, P. R., Steig, E. J., Lini, A. & Southon, J. Millennial-scale storminess variability in the northeastern United States during the Holocene epoch. *Nature* 419, 821–824 (2002).
55. Zhang, X. et al. Climatic control of the late Quaternary turbidite sedimentology of Lake Kivu, East Africa: Implications for deep mixing and geologic hazards. *Geology* 42, 811–814 (2014).

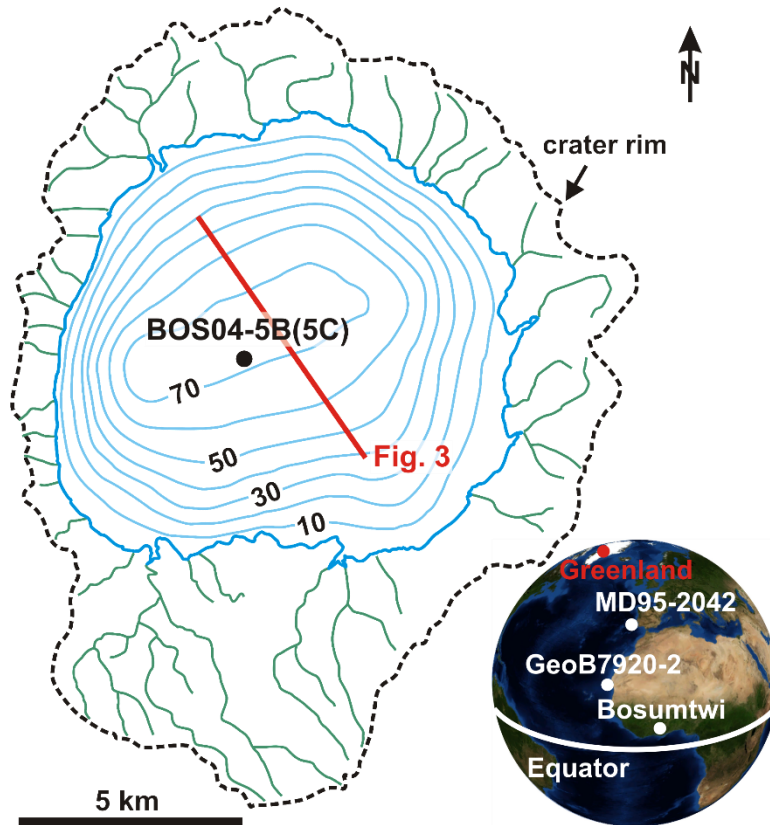


**Figure 1: Map of Lake Bosumtwi showing drainage development on the crater wall, bathymetry (contoured at 10 m interval), and core location of BOS04-5B(5C).**

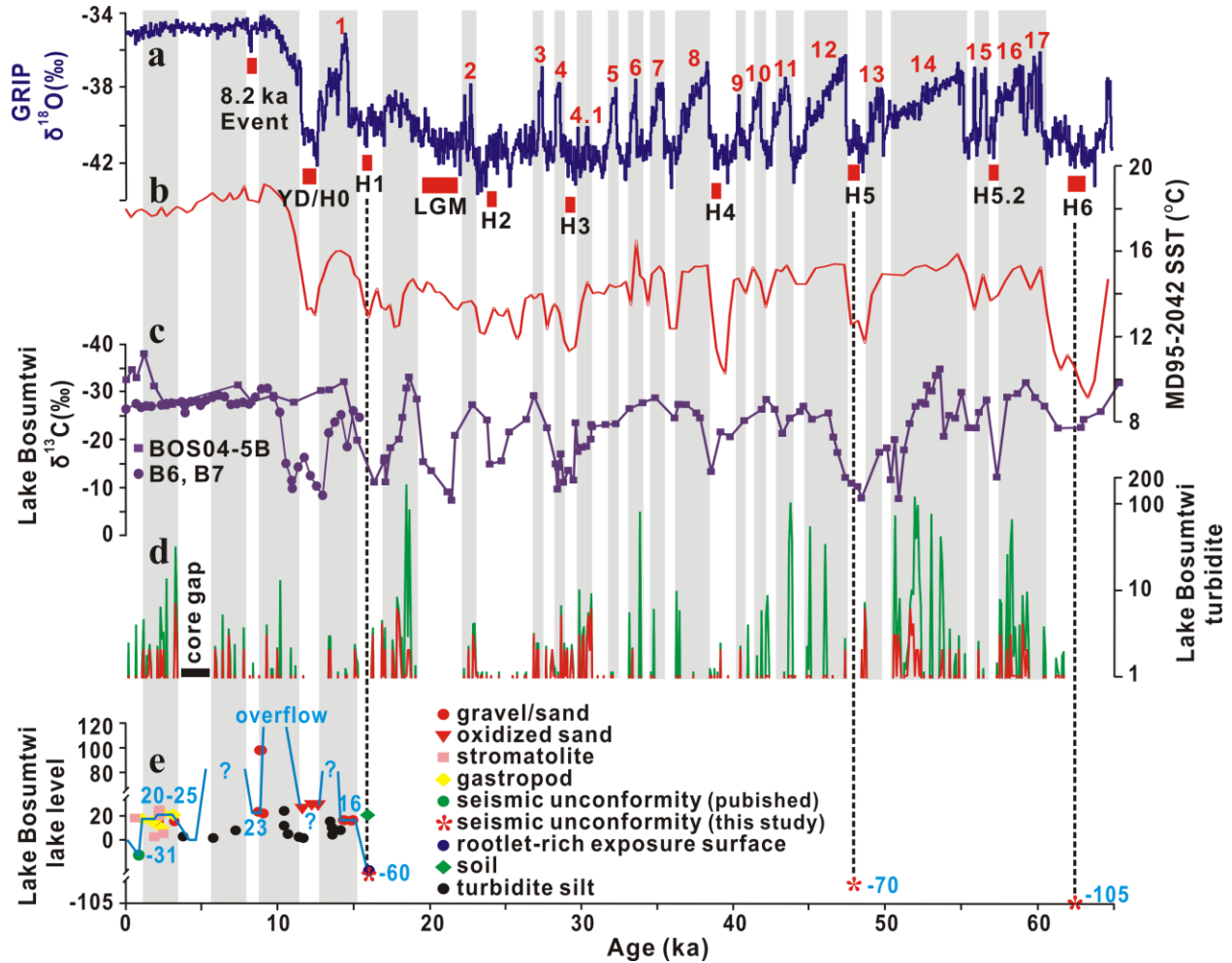


**Figure 2: Comparison of  $\delta^{13}\text{C}$  and turbidite records of Lake Bosumtwi with  $\delta^{18}\text{O}$  and SST records of the North Atlantic ocean.** **a**,  $\delta^{18}\text{O}$  record of GRIP ice core<sup>40</sup>. YD = the Younger Dryas; and LGM = the Last Glacial Maximum. **b**, Alkenone-based SST record from marine sediment core MD95-2042 (37.8°N, 10.2°W)<sup>41</sup>. **c**,  $\delta^{13}\text{C}$  in bulk organic sediments of Lake Bosumtwi drill core BOS04-5B (this study) and piston cores B6 and B7 (ref. 31). **d**, Time series (100 yr bin width) of accumulation rate (green; mm/100 yr) and frequency (red; number of events/100 yr) of turbidite events at Lake Bosumtwi. **e**, Water-level history of Lake Bosumtwi over the past ~16.5 k.y. (refs 25–27). Shadings highlight D–O interstadials and reconstructed water-level highstands of Lake Bosumtwi.

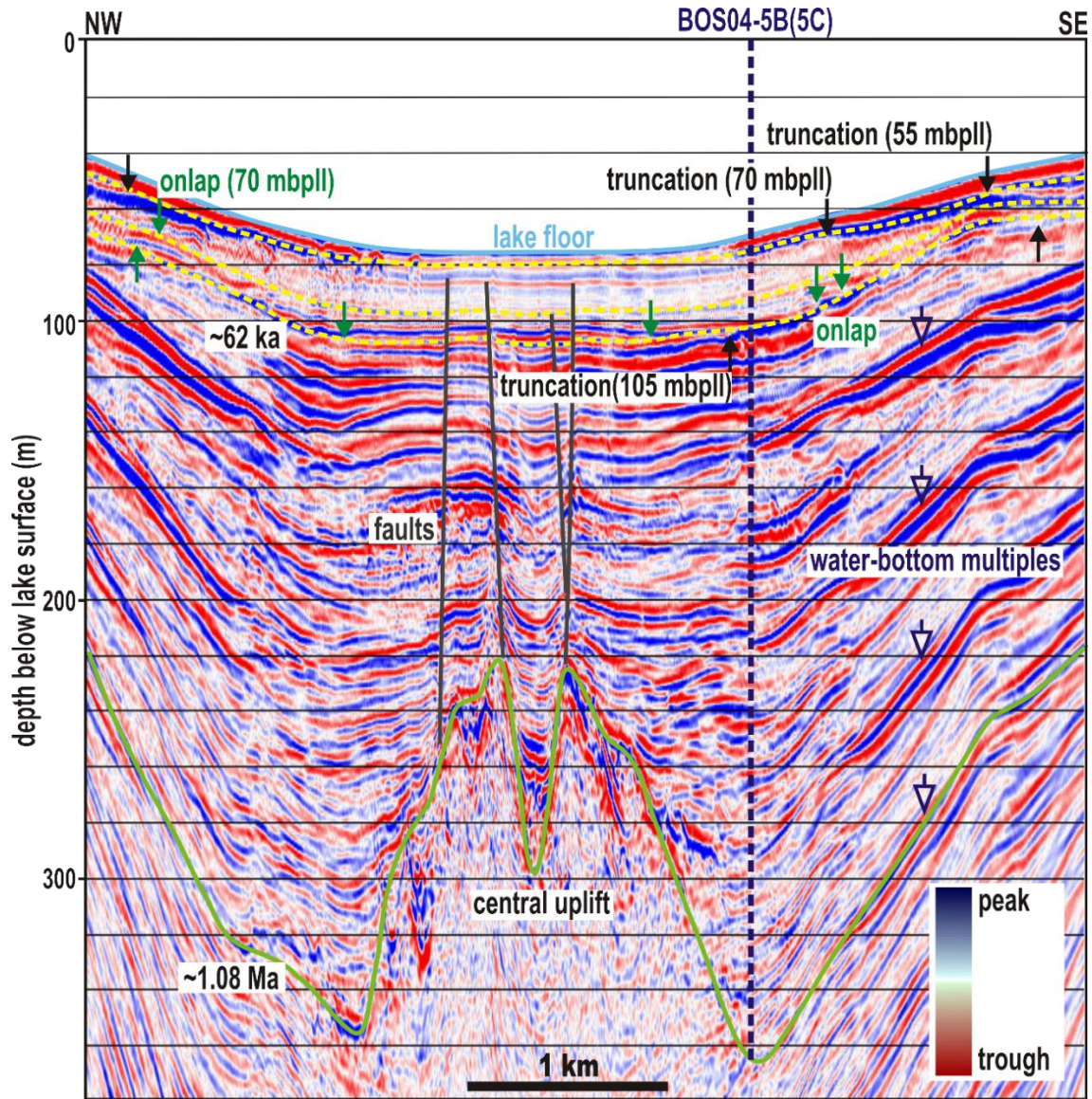


**Figure 3: Exceptional drought events and lake-level lowstands revealed by seismic unconformities.** From shallow to deep, the three unconformable surfaces indicated by dashed yellow lines represent ~55–70 m, ~70 m, and ~105 m lake-level lowstands, and correspond to Heinrich events 1, 5, and 6. The green and black arrows indicate onlap and truncation stratal termination, respectively. Interpretation of faults and the base of the sedimentary section is modified after Scholz et al.<sup>43</sup>.

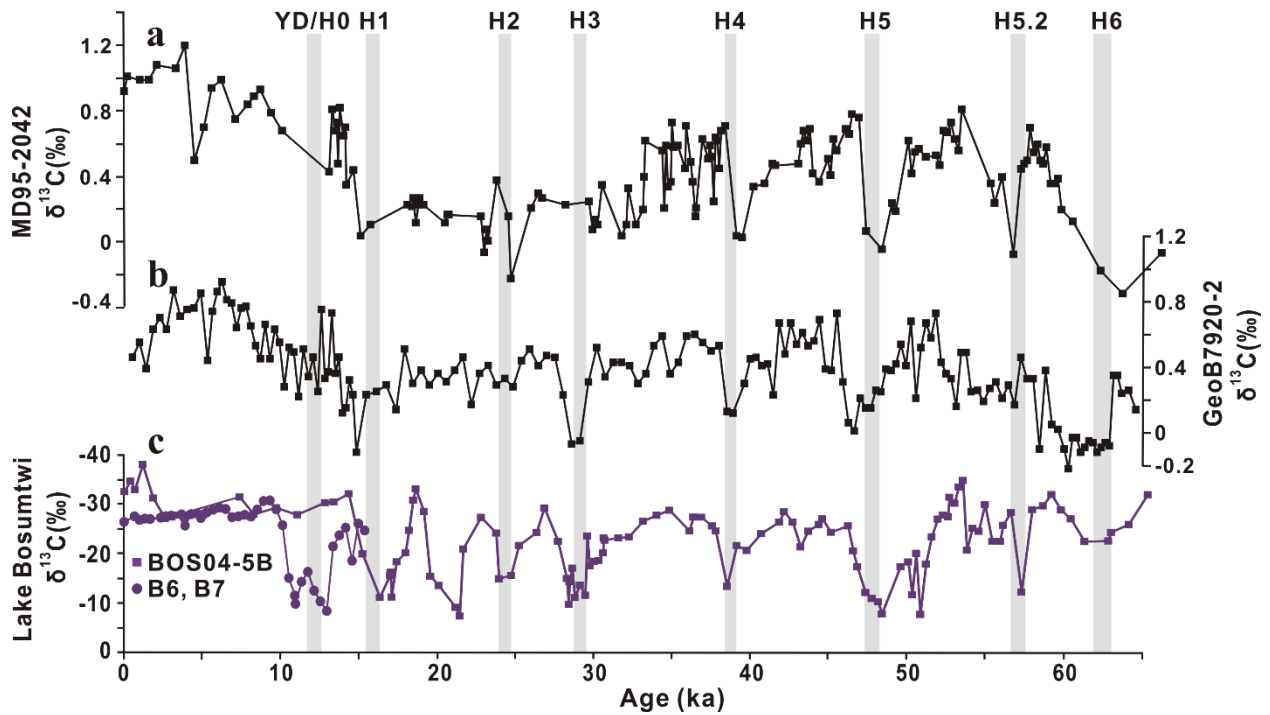
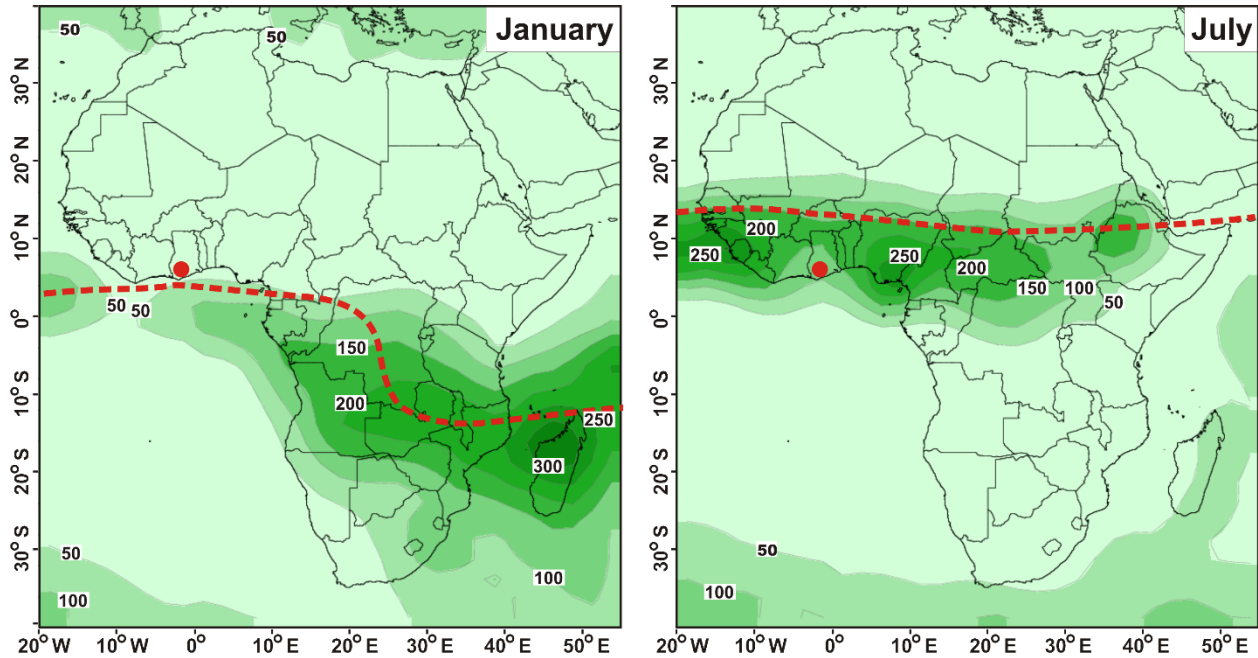
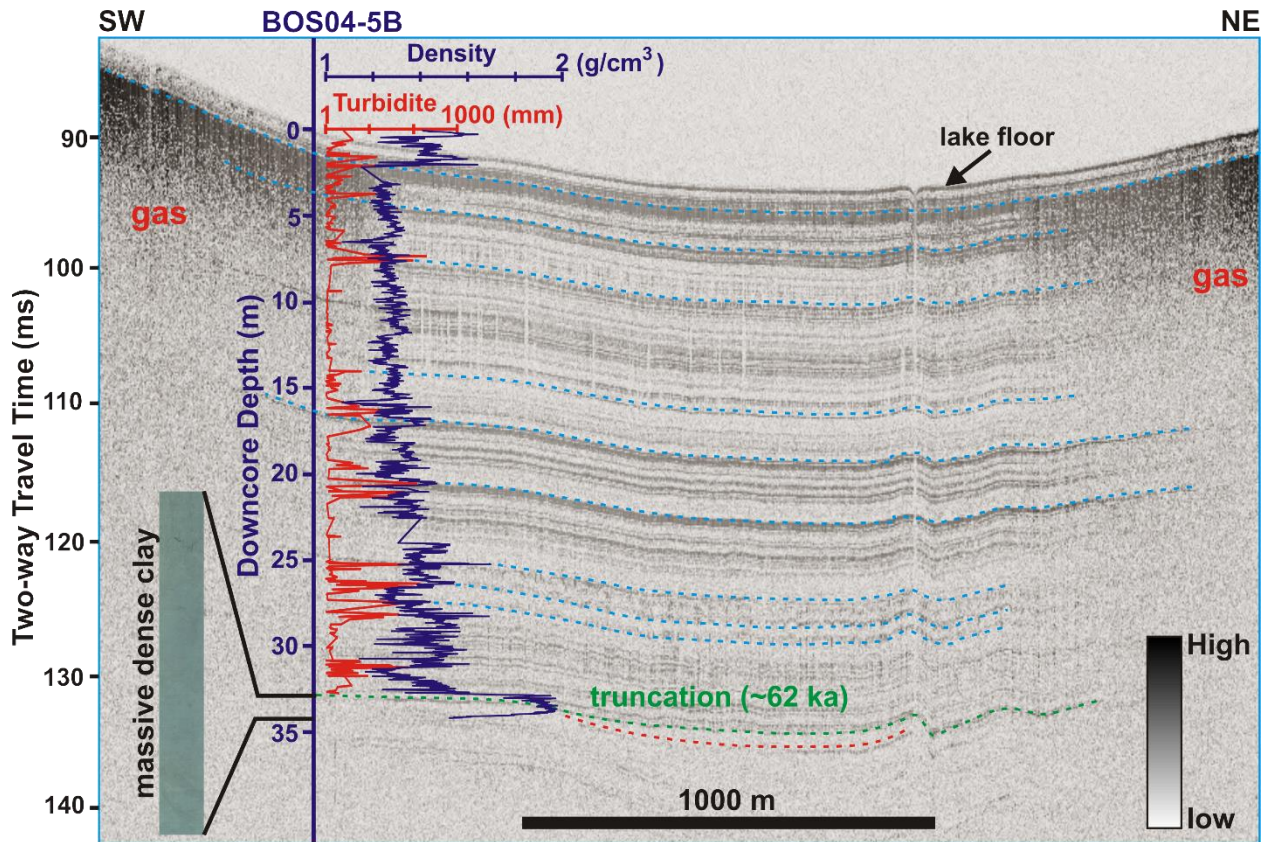


**Figure 4: Exceptional drought events recorded in the Lake Bosumtwi sediments over the past 65 k.y. were associated with slowdowns of the NAMO circulation during Heinrich events. a,  $\delta^{13}\text{C}$  in benthic foraminifera from core MD95-2042 (37.8°N, 10.2°W)<sup>41,50</sup>. b,  $\delta^{13}\text{C}$  in benthic foraminifera from core GeoB7920-2 (20.8°N, 18.6°W)<sup>46</sup>. c, Bulk-organic based  $\delta^{13}\text{C}$  records of drill core BOS04-5B (this study) and piston cores B6 and B7 (ref. 31) of Lake Bosumtwi.**

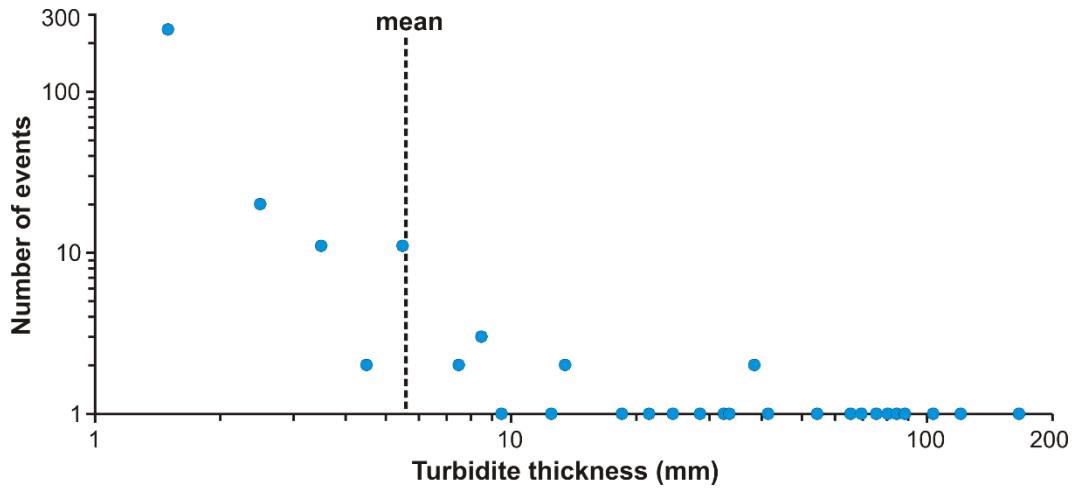


**Extended Data Figure 1:** January and July monthly mean precipitation from 1981 to 2010, calculated by the International Research Institute for Climate and Society (<http://iri.colombia.edu>) based on CAMS (Climate Anomaly Monitoring System)–OPI (Outgoing longwave radiation Precipitation Index) data. Green shading indicates the monthly precipitation contoured at 50 mm interval. The dashed red line indicates the positions of the Intertropical Convergence Zone (ITCZ) over the African continent in January and July<sup>1</sup>. The red dot denotes Lake Bosumtwi.

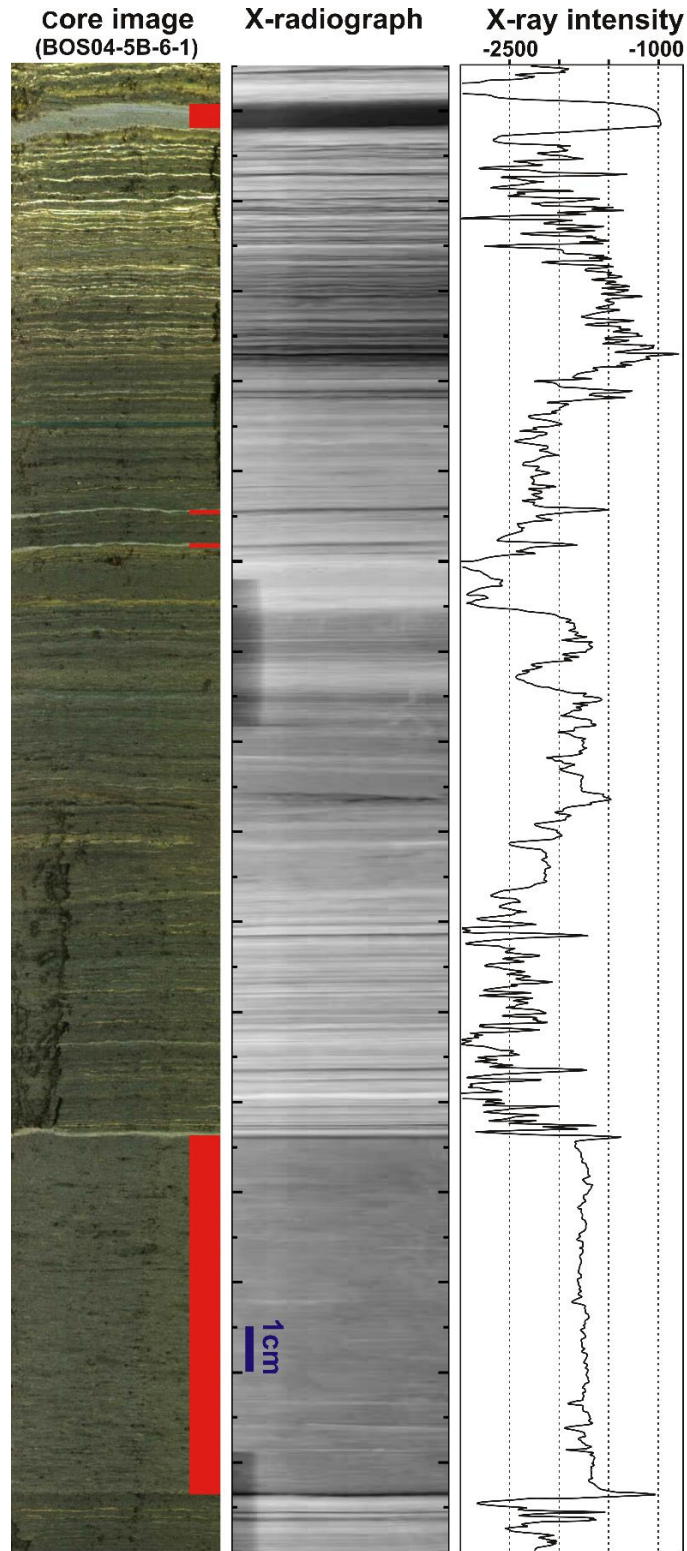




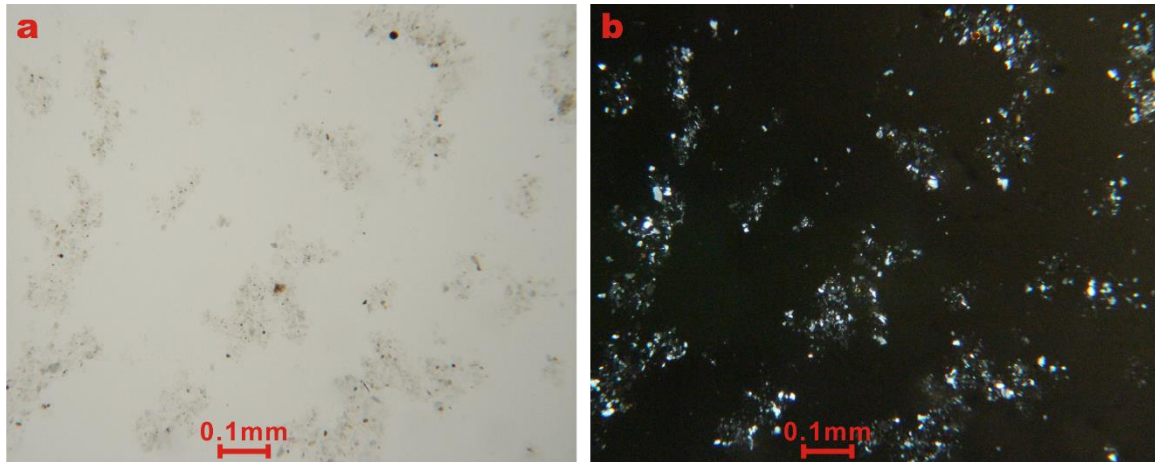
**Extended Data Figure 2:** Seismic–sediment core integration showing that many of the high-amplitude reflectors on the decimeter-resolution CHIRP seismic profiles are correlated with thick turbidites. The red and dark blue curves are turbidite thickness (mm in logarithmic scale) and gamma ray attenuation density ( $\text{g}/\text{cm}^3$ ) of core BOS04-5B, respectively.



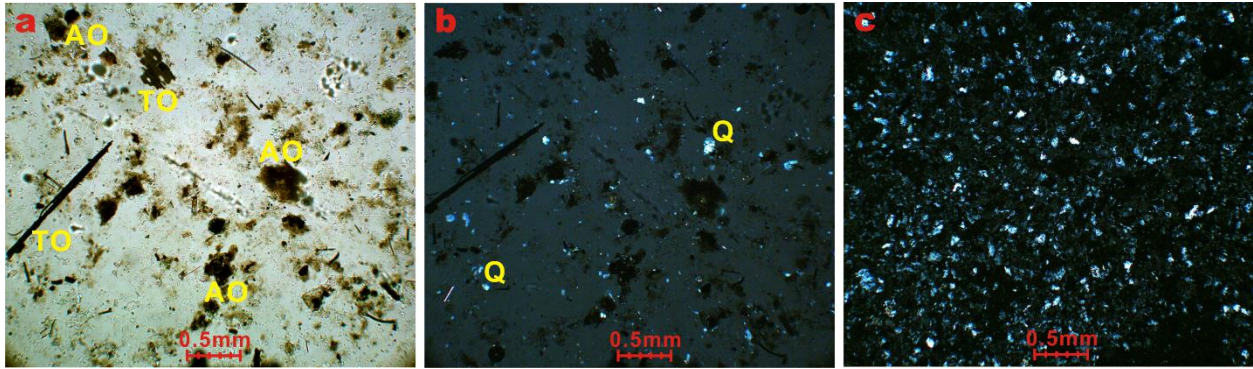
**Extended Data Figure 3: Thickness versus frequency of the past 65 k.y. turbidite events at Lake Bosumtwi.** The total 315 turbidite events (>1 mm thick) have a mean thickness of 5.5 mm. A bin width of 1 mm is used to plot the data.



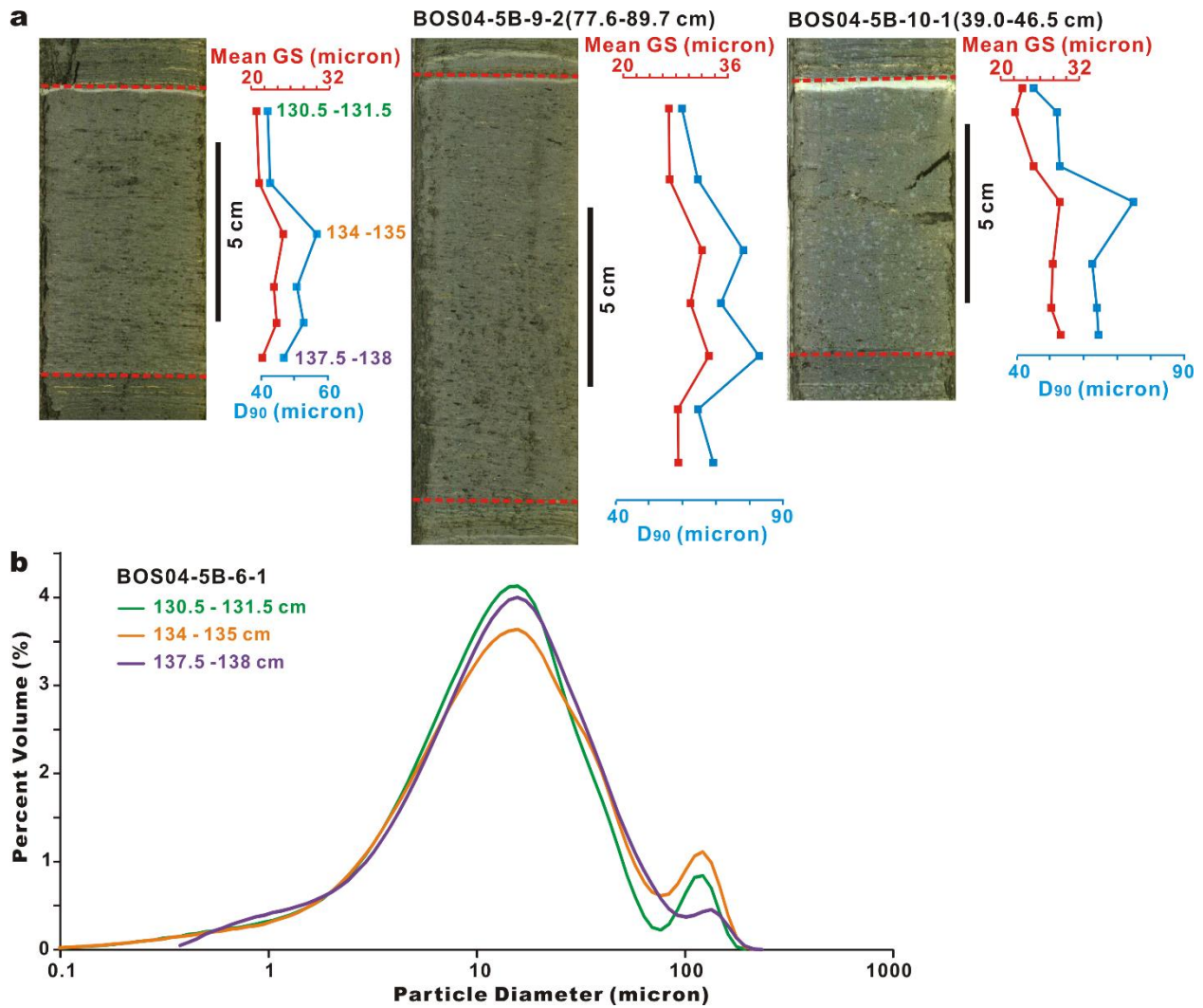
**Extended Data Figure 4:** An example of core images and x-radiographs showing the millimeter- to decimeter-thick turbidites (highlighted in red) observed in core BOS-04-5B.



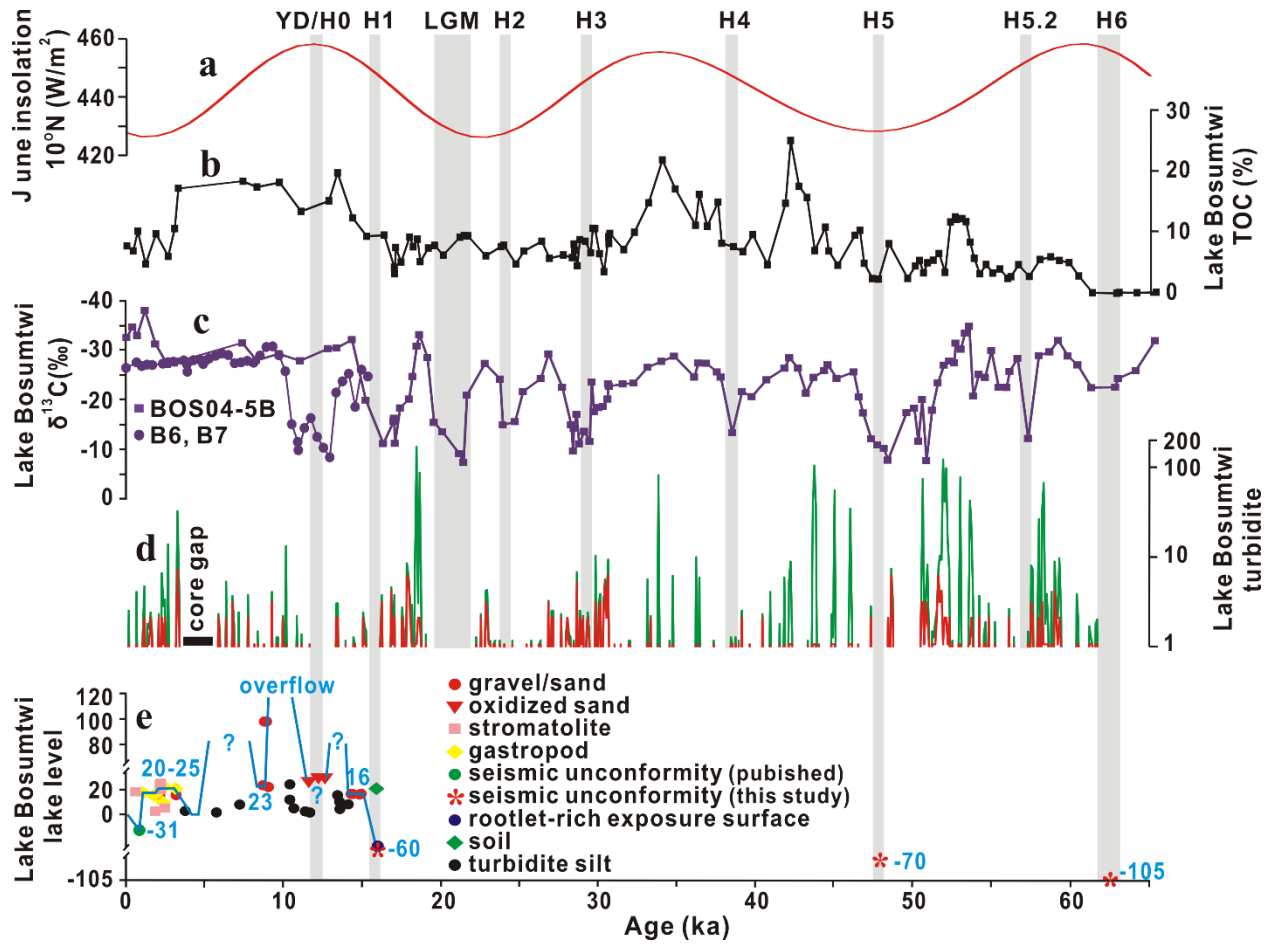
**Extended Data Figure 5: Smear-slide photomicrographs of the light-gray cap of a thick turbidite bed from core BOS04-5B-10-1 (39 - 46.5 cm; Extended Data Fig. 7).** The centimeter- to decimeter thick turbidites display a light-gray cap<sup>2</sup> that is texturally and compositionally similar to the light-colored, millimeter-thick turbidites; both comprise predominantly fine- to medium silt-sized quartz and feldspar grains, and contain little organic matter. **a**, Raw turbidite cap sediments under plane-polarized light. **b**, Raw turbidite cap sediments under cross-polarized light.



**Extended Data Figure 6: Smear-slide photomicrographs of a thick turbidite bed from core BOS04-5B-6-1 (130.3 – 138.4 cm; Extended Data Fig. 7). a–b, Raw sediments (136.5 – 137.5 cm) under plane-polarized light and cross-polarized light. Note the turbidite sediments contain abundant aquatic and terrestrial organic matter. c, Processed sediments (136.5 – 137.5 cm) under cross-polarized light. Inorganic and organic carbon and biogenic silica were removed from the turbidite sediments. TO = terrestrial organic matter; AO = aquatic organic matter; and Q = quartz.**



**Extended Data Figure 7: Examples of grain size profiles and distributions of the centimeter- to decimeter thick turbidite sediments. a,** Thick turbidites commonly display reverse-to-normal grading, typical of flood-introduced turbidites. Inorganic and organic carbon and biogenic silica were removed before running particle size analysis. GS = grain size; and D<sub>90</sub> = the 90<sup>th</sup> particle size percentile. **b,** Particle sizes of the turbidite sediments generally show bimodal, lognormal distributions.



**Extend Data Figure 8: Possible insolation forcing of turbidite accumulation rate at Lake Bosumtwi.** **a**, June insolation at 10° N (W/m<sup>2</sup>). **b**, TOC (%) of core BOS04-5B of Lake Bosumtwi. **c**, δ<sup>13</sup>C in bulk organic matter of drill core BOS04-5B (this study) and piston cores B6 and B7 (ref. 3) of Lake Bosumtwi. **d**, Time series (100 yr bin width) of accumulation rate (green; mm/100 yr) and frequency (red; number of events/100 yr) of turbidite events at Lake Bosumtwi. **e**, Water-level history of Lake Bosumtwi over the past ~16.5 k.y. (refs 4–6). Shadings highlight Heinrich interstadials and the last glacial maximum (LGM).

**Supplementary Table 1. Turbidites (>1 mm) from the upper 65 k.y. of core BOS04-5B of Lake Bosumtwi.** Core BOS04-5C from the same drill site was used to bridge gaps (due to sediment loss during drilling) in core BOS04-5B.

Section	Top (mm)	Bottom (mm)	Thickness (mm)	Downcore Depth (m)	Age (ka)
BOS04-5B-1H-1	112.8	115.2	2.4	0.114	0.18
BOS04-5B-1H-1	641.8	645.8	3.9	0.644	0.64
BOS04-5C-1H-1	117.0	118.4	1.4	0.850	1.05
BOS04-5C-1H-1	160.0	161.8	1.8	0.892	1.14
BOS04-5B-1H-2	129.8	132.5	2.7	0.911	1.18
BOS04-5B-1H-2	212.0	213.6	1.7	0.993	1.36
BOS04-5B-1H-2	251.8	253.3	1.5	1.033	1.42
BOS04-5B-1H-2	350.9	352.1	1.2	1.132	1.56
BOS04-5B-1H-2	352.4	353.4	1.1	1.133	1.56
BOS04-5B-1H-2	391.0	392.3	1.3	1.172	1.61
BOS04-5B-1H-2	590.9	592.0	1.1	1.371	2.03
BOS04-5B-1H-2	617.6	618.8	1.1	1.398	2.09
BOS04-5B-1H-2	669.6	672.9	3.2	1.451	2.23
BOS04-5B-1H-2	687.8	690.9	3.1	1.469	2.27
BOS04-5B-1H-2	728.0	730.7	2.7	1.509	2.38
BOS04-5B-1H-2	751.3	753.5	2.2	1.532	2.44
BOS04-5B-1H-2	768.1	769.1	1.0	1.549	2.48
BOS04-5B-1H-2	842.1	855.5	13.4	1.629	2.66
BOS04-5B-1H-2	1223.6	1224.6	1.1	2.004	3.15
BOS04-5B-1H-2	1309.9	1311.2	1.4	2.091	3.22
BOS04-5B-1H-2	1313.5	1314.6	1.1	2.094	3.22
BOS04-5B-1H-2	1317.6	1318.8	1.3	2.098	3.22
BOS04-5B-1H-2	1328.6	1329.6	1.0	2.109	3.23
BOS04-5B-1H-2	1338.2	1342.4	4.2	2.120	3.24
BOS04-5B-1H-2	1345.5	1346.7	1.2	2.126	3.25
BOS04-5B-1H-2	1351.0	1372.5	21.5	2.142	3.26
BOS04-5B-1H-2	1422.4	1423.4	1.1	2.203	3.33
BOS04-5B-1H-2	1427.0	1431.1	4.1	2.209	3.38
BOS04-5C-1H-2	108.9	110.0	1.2	2.657	5.81
BOS04-5C-1H-2	118.5	119.5	1.0	2.667	5.86
BOS04-5C-1H-2	126.2	127.6	1.4	2.675	5.91
BOS04-5C-1H-2	193.4	194.7	1.3	2.742	6.32
BOS04-5C-1H-2	200.4	204.2	3.8	2.750	6.37
BOS04-5C-1H-2	266.9	267.9	1.0	2.815	6.72
BOS04-5C-1H-2	273.5	274.5	1.0	2.822	6.74
BOS04-5C-1H-2	285.1	286.6	1.5	2.834	6.78
BOS04-5C-1H-2	324.1	325.8	1.7	2.873	6.90



BOS04-5C-1H-2	402.1	404.4	2.3	2.951	7.13
BOS04-5B-2H-1	161.6	163.2	1.5	3.162	7.71
BOS04-5B-2H-1	192.5	194.6	2.1	3.194	7.79
BOS04-5B-2H-1	318.5	319.5	1.0	3.319	8.16
BOS04-5B-2H-1	378.5	379.9	1.4	3.379	8.33
BOS04-5B-2H-1	494.8	495.8	1.0	3.495	8.80
BOS04-5B-2H-1	591.6	592.6	1.1	3.592	9.21
BOS04-5B-2H-1	603.8	605.5	1.6	3.605	9.26
BOS04-5B-2H-1	606.6	607.8	1.2	3.607	9.28
BOS04-5B-2H-1	649.7	650.8	1.2	3.650	9.51
BOS04-5B-2H-1	669.3	670.5	1.2	3.670	9.62
BOS04-5B-2H-1	727.6	728.6	1.0	3.728	9.93
BOS04-5B-2H-1	739.7	740.8	1.1	3.740	10.00
BOS04-5B-2H-1	762.7	775.5	12.8	3.769	10.15
BOS04-5B-2H-1	952.5	954.6	2.1	3.954	10.87
BOS04-5B-2H-1	1013.2	1014.5	1.3	4.014	11.11
BOS04-5B-2H-1	1110.1	1111.2	1.0	4.111	11.61
BOS04-5B-2H-1	1423.7	1425.3	1.6	4.424	13.31
BOS04-5B-2H-2	11.7	13.0	1.3	4.512	13.38
BOS04-5B-2H-2	68.9	70.4	1.6	4.570	13.43
BOS04-5B-2H-2	74.5	75.8	1.3	4.575	13.43
BOS04-5B-2H-2	282.7	283.8	1.1	4.783	13.98
BOS04-5B-2H-2	377.9	379.1	1.2	4.879	14.41
BOS04-5B-2H-2	408.8	409.9	1.0	4.909	14.56
BOS04-5B-2H-2	542.1	543.1	1.0	5.043	15.06
BOS04-5B-2H-2	568.7	570.0	1.3	5.069	15.10
BOS04-5B-2H-2	624.4	626.0	1.6	5.125	15.17
BOS04-5B-2H-2	693.0	694.4	1.4	5.194	15.26
BOS04-5B-2H-2	927.2	928.4	1.2	5.428	16.12
BOS04-5B-2H-2	962.1	963.3	1.1	5.463	16.22
BOS04-5B-2H-2	964.5	965.9	1.4	5.465	16.23
BOS04-5B-2H-2	986.2	987.3	1.1	5.487	16.30
BOS04-5B-2H-2	1189.0	1190.2	1.2	5.690	16.80
BOS04-5B-2H-2	1197.5	1198.5	1.0	5.698	16.82
BOS04-5B-2H-2	1210.9	1212.0	1.1	5.711	16.84
BOS04-5B-2H-2	1214.9	1216.0	1.1	5.715	16.85
BOS04-5B-2H-2	1244.6	1245.7	1.1	5.745	16.90
BOS04-5B-2H-2	1315.6	1316.7	1.1	5.816	17.01
BOS04-5B-2H-CC	19.0	21.6	2.5	5.910	17.04
BOS04-5B-3H-1	477.8	479.3	1.6	6.479	17.52
BOS04-5B-3H-1	504.4	505.4	1.0	6.505	17.60
BOS04-5B-3H-1	531.7	533.1	1.4	6.532	17.68
BOS04-5B-3H-1	597.6	598.6	1.0	6.598	17.87

BOS04-5B-3H-1	615.0	616.4	1.4	6.616	17.88
BOS04-5B-3H-1	617.0	618.1	1.1	6.618	17.88
BOS04-5B-3H-1	618.8	620.9	2.1	6.620	17.88
BOS04-5B-3H-1	621.4	623.0	1.6	6.622	17.89
BOS04-5B-3H-1	642.0	643.0	1.0	6.642	17.90
BOS04-5B-3H-1	678.6	679.8	1.2	6.679	17.93
BOS04-5B-3H-1	681.3	682.4	1.1	6.682	17.93
BOS04-5B-3H-1	750.6	751.6	1.0	6.751	17.98
BOS04-5B-3H-1	752.1	753.4	1.3	6.753	17.98
BOS04-5B-3H-1	754.8	755.8	1.1	6.755	17.98
BOS04-5B-3H-1	805.2	806.8	1.6	6.806	18.01
BOS04-5B-3H-1	833.6	834.7	1.1	6.834	18.03
BOS04-5B-3H-1	1045.6	1048.3	2.8	7.047	18.19
BOS04-5B-3H-1	1280.2	1287.5	7.3	7.284	18.37
BOS04-5B-3H-1	1297.5	1465.3	167.7	7.381	18.46
BOS04-5B-3H-1	1490.7	1492.2	1.5	7.491	18.55
BOS04-5B-3H-2	46.6	48.0	1.4	7.547	18.59
BOS04-5B-3H-2	72.2	73.2	1.1	7.573	18.61
BOS04-5B-3H-2	87.6	172.4	84.8	7.630	18.65
BOS04-5B-3H-2	276.3	279.6	3.2	7.778	18.78
BOS04-5B-3H-2	395.5	396.8	1.3	7.896	19.03
BOS04-5B-4H-1	204.6	205.7	1.2	9.205	22.30
BOS04-5B-4H-1	267.7	268.8	1.1	9.268	22.51
BOS04-5B-4H-1	276.7	277.9	1.1	9.277	22.54
BOS04-5B-4H-1	376.8	377.9	1.1	9.377	22.86
BOS04-5B-4H-1	381.2	382.7	1.5	9.382	22.88
BOS04-5B-4H-1	384.1	385.5	1.4	9.385	22.89
BOS04-5B-4H-1	391.2	393.4	2.2	9.392	22.91
BOS04-5B-4H-1	396.9	398.8	1.9	9.398	22.93
BOS04-5B-4H-1	426.0	427.1	1.1	9.427	23.04
BOS04-5B-4H-1	454.0	455.1	1.1	9.455	23.14
BOS04-5B-4H-1	499.6	500.7	1.0	9.500	23.31
BOS04-5B-4H-1	527.5	528.6	1.1	9.528	23.41
BOS04-5B-4H-1	643.3	644.4	1.1	9.644	23.73
BOS04-5B-4H-1	1031.8	1032.8	1.0	10.032	24.01
BOS04-5B-4H-1	1280.5	1281.5	1.1	10.281	24.57
BOS04-5B-4H-2	166.7	167.8	1.0	10.657	25.42
BOS04-5B-4H-2	244.4	245.5	1.1	10.735	25.77
BOS04-5B-4H-2	463.6	464.7	1.0	10.954	26.27
BOS04-5B-4H-2	521.4	522.4	1.1	11.012	26.36
BOS04-5B-4H-2	743.4	744.5	1.1	11.234	26.80
BOS04-5B-4H-2	748.5	749.5	1.0	11.239	26.81
BOS04-5B-4H-2	753.4	754.4	1.0	11.244	26.82

BOS04-5B-4H-2	869.0	870.3	1.4	11.360	27.08
BOS04-5B-4H-2	874.3	875.3	1.0	11.365	27.09
BOS04-5B-4H-2	890.6	891.9	1.3	11.381	27.13
BOS04-5B-4H-2	894.8	895.9	1.1	11.385	27.14
BOS04-5B-4H-2	1052.7	1053.7	1.1	11.543	27.63
BOS04-5B-4H-2	1066.4	1067.5	1.1	11.557	27.68
BOS04-5B-4H-2	1201.7	1203.0	1.3	11.692	27.99
BOS04-5B-4H-2	1247.1	1248.2	1.0	11.738	28.07
BOS04-5B-4H-2	1257.3	1258.4	1.0	11.748	28.09
BOS04-5B-4H-2	1288.5	1289.8	1.3	11.779	28.15
BOS04-5B-4H-2	1340.1	1341.3	1.2	11.831	28.22
BOS04-5C-4H-2	395.5	396.6	1.1	12.060	28.47
BOS04-5B-5H-1	379.4	380.5	1.1	12.380	28.64
BOS04-5B-5H-1	442.7	443.8	1.1	12.443	28.66
BOS04-5B-5H-1	460.8	462.4	1.5	12.462	28.67
BOS04-5B-5H-1	464.7	466.3	1.6	12.466	28.67
BOS04-5B-5H-1	477.6	478.7	1.2	12.478	28.67
BOS04-5B-5H-1	710.9	712.1	1.2	12.711	28.81
BOS04-5B-5H-1	730.9	732.1	1.2	12.731	28.83
BOS04-5B-5H-1	874.9	876.1	1.2	12.875	28.98
BOS04-5B-5H-1	949.3	950.4	1.1	12.950	29.06
BOS04-5B-5H-1	970.8	971.8	1.0	12.971	29.09
BOS04-5B-5H-1	1156.4	1157.5	1.1	13.157	29.26
BOS04-5B-5H-1	1231.5	1232.7	1.2	13.232	29.34
BOS04-5B-5H-1	1264.3	1265.3	1.1	13.265	29.38
BOS04-5B-5H-1	1276.2	1277.5	1.3	13.277	29.40
BOS04-5B-5H-2	508.1	509.3	1.2	14.009	29.83
BOS04-5B-5H-2	544.7	550.7	6.0	14.048	29.88
BOS04-5B-5H-2	555.4	558.2	2.8	14.057	29.89
BOS04-5B-5H-2	750.3	752.0	1.7	14.251	30.08
BOS04-5B-5H-2	761.4	762.6	1.2	14.262	30.09
BOS04-5B-5H-2	813.1	814.2	1.1	14.314	30.12
BOS04-5B-5H-2	894.7	896.1	1.5	14.395	30.17
BOS04-5B-5H-2	909.1	910.2	1.1	14.410	30.18
BOS04-5B-5H-2	1037.6	1039.2	1.6	14.538	30.35
BOS04-5B-5H-2	1063.6	1064.8	1.2	14.564	30.39
BOS04-5B-5H-2	1095.8	1096.8	1.0	14.596	30.43
BOS04-5B-5H-2	1117.8	1118.8	1.0	14.618	30.45
BOS04-5B-5H-2	1152.1	1153.2	1.1	14.653	30.48
BOS04-5B-5H-2	1158.5	1159.6	1.1	14.659	30.48
BOS04-5B-5H-2	1162.4	1163.6	1.2	14.663	30.49
BOS04-5B-5H-2	1205.2	1206.2	1.1	14.706	30.52
BOS04-5B-5H-2	1273.6	1275.7	2.1	14.775	30.58

BOS04-5B-5H-2	1372.7	1373.7	1.0	14.873	30.61
BOS04-5B-5H-2	1385.8	1387.7	1.9	14.887	30.62
BOS04-5B-5H-2	1401.6	1403.0	1.4	14.902	30.62
BOS04-5B-6H-1	21.6	22.9	1.3	15.022	30.65
BOS04-5B-6H-1	52.1	53.7	1.6	15.053	30.66
BOS04-5B-6H-1	131.2	133.0	1.8	15.132	30.69
BOS04-5B-6H-1	289.8	290.9	1.0	15.290	31.05
BOS04-5B-6H-1	412.1	413.1	1.0	15.413	31.48
BOS04-5B-6H-1	577.3	578.4	1.1	15.578	31.96
BOS04-5B-6H-1	622.4	623.5	1.1	15.623	32.05
BOS04-5B-6H-1	1074.1	1079.5	5.4	16.077	33.13
BOS04-5B-6H-1	1165.2	1166.2	1.0	16.166	33.31
BOS04-5B-6H-1	1172.7	1173.8	1.1	16.173	33.33
BOS04-5B-6H-1	1303.2	1383.8	80.6	16.344	33.83
BOS04-5B-6H-2	53.0	54.1	1.1	16.554	34.54
BOS04-5B-6H-2	113.7	119.5	5.9	16.617	34.72
BOS04-5B-6H-2	707.5	717.1	9.6	17.212	36.23
BOS04-5B-6H-2	924.9	930.6	5.7	17.428	36.45
BOS04-5B-6H-2	1330.6	1331.7	1.1	17.831	37.31
BOS04-5B-7H-1	232.9	234.1	1.2	18.233	38.46
BOS04-5B-7H-1	282.3	283.3	1.0	18.283	38.52
BOS04-5B-7H-1	429.2	430.4	1.2	18.430	38.73
BOS04-5B-7H-1	544.8	545.9	1.1	18.545	39.00
BOS04-5B-7H-1	594.5	595.7	1.2	18.595	39.11
BOS04-5B-7H-1	598.3	599.4	1.2	18.599	39.12
BOS04-5B-7H-1	853.9	854.9	1.0	18.854	39.67
BOS04-5B-7H-1	1156.9	1158.0	1.1	19.157	40.41
BOS04-5B-7H-1	1174.4	1175.5	1.1	19.175	40.48
BOS04-5B-7H-1	1349.9	1353.7	3.9	19.352	41.00
BOS04-5B-7H-1	1482.3	1484.1	1.7	19.483	41.54
BOS04-5B-7H-2	36.4	42.0	5.7	19.539	41.81
BOS04-5B-7H-2	139.0	144.1	5.1	19.642	42.20
BOS04-5B-7H-2	150.1	158.7	8.6	19.654	42.23
BOS04-5B-7H-2	197.8	199.0	1.2	19.698	42.33
BOS04-5B-7H-2	757.2	758.3	1.1	20.258	43.34
BOS04-5B-7H-2	953.8	986.8	33.0	20.470	43.67
BOS04-5B-7H-2	1006.4	1109.6	103.2	20.558	43.73
BOS04-5B-7H-2	1111.8	1150.0	38.2	20.631	43.84
BOS04-5B-7H-2	1223.5	1224.5	1.0	20.724	44.08
BOS04-5C-7H-2	448.4	450.6	2.2	20.967	44.84
BOS04-5C-7H-2	475.2	476.4	1.2	20.993	44.93
BOS04-5B-8H-1	5.9	60.4	54.6	21.033	45.10
BOS04-5B-8H-1	259.1	260.5	1.4	21.260	45.97

BOS04-5B-8H-1	290.8	324.7	33.8	21.308	46.09
BOS04-5B-8H-1	343.7	345.8	2.1	21.345	46.18
BOS04-5B-8H-1	720.7	721.8	1.0	21.721	46.59
BOS04-5B-8H-2	45.1	46.3	1.2	22.546	47.35
BOS04-5B-8H-2	49.4	50.9	1.5	22.550	47.36
BOS04-5C-8H-1	1272.7	1273.7	1.0	23.426	48.45
BOS04-5C-8H-1	1283.7	1284.7	1.0	23.437	48.46
BOS04-5C-8H-1	1391.2	1392.2	1.0	23.544	48.64
BOS04-5C-8H-1	1394.4	1395.5	1.1	23.547	48.64
BOS04-5C-8H-1	1415.6	1416.7	1.1	23.569	48.68
BOS04-5C-8H-1	1418.4	1419.8	1.3	23.571	48.68
BOS04-5C-8H-1	1421.1	1422.6	1.5	23.574	48.69
BOS04-5C-8H-1	1425.3	1426.5	1.2	23.578	48.70
BOS04-5C-8H-1	1459.0	1461.0	2.1	23.612	48.75
BOS04-5C-8H-1	1464.6	1465.8	1.2	23.618	48.76
BOS04-5B-9H-1	1006.3	1007.5	1.2	25.007	50.52
BOS04-5B-9H-1	1042.0	1043.1	1.0	25.043	50.55
BOS04-5B-9H-1	1071.5	1072.5	1.0	25.072	50.57
BOS04-5B-9H-1	1119.1	1121.0	1.8	25.120	50.61
BOS04-5B-9H-1	1133.5	1134.7	1.2	25.134	50.62
BOS04-5B-9H-1	1192.7	1262.7	70.0	25.228	50.70
BOS04-5B-9H-1	1322.9	1324.1	1.2	25.323	50.78
BOS04-5B-9H-1	1365.3	1366.7	1.4	25.366	50.81
BOS04-5B-9H-1	1379.0	1380.2	1.1	25.380	50.82
BOS04-5B-9H-1	1448.1	1449.2	1.0	25.449	50.90
BOS04-5B-9H-1	1487.2	1493.1	5.8	25.490	50.95
BOS04-5B-9H-2	13.3	15.4	2.1	25.514	50.97
BOS04-5B-9H-2	40.1	41.3	1.2	25.541	51.01
BOS04-5B-9H-2	212.8	214.2	1.4	25.713	51.21
BOS04-5B-9H-2	306.3	307.5	1.2	25.807	51.32
BOS04-5B-9H-2	457.2	459.0	1.8	25.958	51.50
BOS04-5B-9H-2	539.8	541.0	1.2	26.040	51.60
BOS04-5B-9H-2	542.0	543.2	1.2	26.043	51.60
BOS04-5B-9H-2	547.1	548.3	1.1	26.048	51.60
BOS04-5B-9H-2	548.5	549.6	1.1	26.049	51.61
BOS04-5B-9H-2	560.6	561.6	1.0	26.061	51.62
BOS04-5B-9H-2	603.6	604.8	1.2	26.104	51.67
BOS04-5B-9H-2	617.2	618.4	1.2	26.118	51.69
BOS04-5B-9H-2	620.6	622.2	1.6	26.121	51.69
BOS04-5B-9H-2	672.9	674.1	1.1	26.174	51.75
BOS04-5B-9H-2	687.8	695.5	7.7	26.192	51.78
BOS04-5B-9H-2	708.2	709.3	1.2	26.209	51.80
BOS04-5B-9H-2	717.1	718.6	1.5	26.218	51.81

BOS04-5B-9H-2	718.6	720.5	1.9	26.220	51.81
BOS04-5B-9H-2	761.9	764.1	2.2	26.263	51.86
BOS04-5B-9H-2	769.6	773.0	3.4	26.271	51.87
BOS04-5B-9H-2	776.0	897.0	121.0	26.337	51.95
BOS04-5B-9H-2	905.2	907.0	1.8	26.406	52.03
BOS04-5B-9H-2	924.4	963.1	38.6	26.444	52.07
BOS04-5B-9H-2	973.5	981.7	8.2	26.478	52.10
BOS04-5B-9H-2	985.3	1073.5	88.3	26.529	52.16
BOS04-5B-9H-2	1095.8	1109.7	13.9	26.603	52.23
BOS04-5B-9H-2	1176.4	1177.8	1.4	26.677	52.31
BOS04-5B-9H-2	1247.2	1252.5	5.3	26.750	52.39
BOS04-5B-9H-CC	6.0	7.0	1.1	26.937	52.58
BOS04-5B-10H-1	280.1	281.2	1.1	27.281	52.94
BOS04-5B-10H-1	389.6	465.4	75.8	27.427	53.09
BOS04-5B-10H-1	966.7	967.7	1.0	27.967	53.52
BOS04-5B-10H-1	1094.2	1135.8	41.6	28.115	53.64
BOS04-5B-10H-1	1261.7	1263.7	1.9	28.263	53.76
BOS04-5B-10H-1	1266.3	1284.9	18.6	28.276	53.77
BOS04-5B-10H-1	1408.9	1412.2	3.3	28.411	53.88
BOS04-5B-10H-2	187.0	189.1	2.2	28.698	54.25
BOS04-5B-10H-2	191.5	192.7	1.3	28.702	54.25
BOS04-5B-10H-2	411.7	412.9	1.3	28.922	54.53
BOS04-5B-10H-2	504.8	506.5	1.8	29.016	54.65
BOS04-5B-10H-2	678.1	679.7	1.6	29.189	54.87
BOS04-5B-10H-2	686.9	688.1	1.3	29.197	54.88
BOS04-5B-10H-2	953.8	955.6	1.8	29.465	55.23
BOS04-5B-11H-1	35.4	36.4	1.1	30.036	56.12
BOS04-5B-11H-1	37.6	39.0	1.4	30.038	56.12
BOS04-5B-11H-1	221.7	222.9	1.2	30.222	56.41
BOS04-5B-11H-1	698.6	700.0	1.4	30.699	57.33
BOS04-5B-11H-1	793.1	794.5	1.4	30.794	57.53
BOS04-5B-11H-1	794.8	795.8	1.0	30.795	57.53
BOS04-5B-11H-1	801.1	806.4	5.3	30.804	57.55
BOS04-5B-11H-1	843.2	844.5	1.3	30.844	57.64
BOS04-5B-11H-1	859.1	864.8	5.6	30.862	57.67
BOS04-5B-11H-1	1003.4	1005.3	2.0	31.004	57.98
BOS04-5B-11H-1	1027.9	1028.9	1.0	31.028	58.03
BOS04-5B-11H-1	1033.3	1058.0	24.7	31.046	58.07
BOS04-5B-11H-1	1093.5	1122.4	28.9	31.108	58.20
BOS04-5B-11H-1	1124.6	1126.5	1.9	31.126	58.24
BOS04-5B-11H-1	1148.0	1149.1	1.2	31.149	58.29
BOS04-5B-11H-1	1154.4	1220.1	65.7	31.187	58.37
BOS04-5B-11H-1	1234.4	1236.1	1.7	31.235	58.47

BOS04-5B-11H-1	1266.8	1270.5	3.7	31.269	58.55
BOS04-5B-11H-1	1305.6	1306.9	1.3	31.306	58.63
BOS04-5B-11H-1	1416.3	1420.2	3.9	31.418	58.86
BOS04-5B-11H-1	1492.5	1493.5	1.1	31.493	59.01
BOS04-5B-11H-2	16.3	17.7	1.4	31.497	59.01
BOS04-5B-11H-2	27.8	28.8	1.0	31.508	59.03
BOS04-5B-11H-2	31.7	36.8	5.1	31.514	59.05
BOS04-5B-11H-2	74.1	75.5	1.4	31.555	59.12
BOS04-5B-11H-2	105.3	106.9	1.7	31.586	59.18
BOS04-5B-11H-2	139.9	141.9	2.0	31.621	59.25
BOS04-5B-11H-2	195.8	196.9	1.1	31.676	59.35
BOS04-5B-11H-2	197.3	205.6	8.3	31.681	59.36
BOS04-5B-11H-2	222.4	224.9	2.6	31.704	59.41
BOS04-5B-11H-2	754.6	758.3	3.7	32.236	60.42
BOS04-5B-11H-2	843.2	845.0	1.8	32.324	60.59
BOS04-5B-11H-2	1057.4	1059.0	1.6	32.538	61.22
BOS04-5B-11H-2	1087.0	1088.1	1.2	32.568	61.33
BOS04-5B-11H-2	1128.2	1129.2	1.0	32.609	61.47
BOS04-5B-11H-2	1183.5	1185.1	1.7	32.664	61.67
BOS04-5B-11H-2	1208.9	1210.8	1.9	32.690	61.76

**Supplementary Table 2. TOC and  $\delta^{13}\text{C}$  measurements of core BOS04-5B.**

Section	Section Depth (cm)	Downcore Depth (m)	Age (ka)	TOC (%)	$\delta^{13}\text{C}$ (‰)
BOS04-5B-1H-1	4-6	0.05	0.05	8.1	-32.9
BOS04-5B-1H-1	36-38	0.37	0.44	7.2	-34.8
BOS04-5B-1H-1	68-70	0.69	0.73	10.5	-33.1
BOS04-5B-1H-2	12-19	0.94	1.23	5.1	-38.1
BOS04-5B-1H-2	52-54	1.31	1.89	10.1	-31.3
BOS04-5B-1H-2	84-86	1.63	2.66	6.3	-27.1
BOS04-5B-1H-2	116-118	1.95	3.08	10.9	-27.5
BOS04-5B-1H-CC	0-3	2.20	3.31	17.6	-27.9
BOS04-5B-2H-1	4-6	3.05	7.41	18.7	-31.6
BOS04-5B-2H-1	36-38	3.37	8.31	17.7	-28.1
BOS04-5B-2H-1	68-70	3.69	9.72	18.5	-29.4
BOS04-5B-2H-1	100-102	4.01	11.09	13.7	-27.9
BOS04-5B-2H-1	132-134	4.33	12.87	15.5	-30.4
BOS04-5B-2H-2	4-6	4.55	13.41	20.1	-30.6
BOS04-5B-2H-2	36-38	4.87	14.37	12.7	-32.2
BOS04-5B-2H-2	68-70	5.19	15.25	9.7	-20.0
BOS04-5B-2H-2	100-102	5.51	16.37	9.9	-11.2
BOS04-5B-2H-2	132-134	5.83	17.01	4.6	-15.7
BOS04-5B-2H-CC	0-6	5.92	17.05	3.5	-16.3
BOS04-5B-3H-1	12-14	6.13	17.10	7.8	-11.3
BOS04-5B-3H-1	44-46	6.45	17.44	5.4	-18.4
BOS04-5B-3H-1	76-78	6.77	17.99	9.5	-20.2
BOS04-5B-3H-1	108-110	7.09	18.22	7.9	-24.8
BOS04-5B-3H-1	140-142	7.41	18.49	9.2	-30.9
BOS04-5B-3H-2	12-14	7.63	18.65	5.5	-33.2
BOS04-5B-3H-2	44-46	7.95	19.17	7.7	-28.6
BOS04-5B-3H-2	76-78	8.27	19.58	8.2	-15.5
BOS04-5B-3H-2	108-110	8.59	20.11	6.5	-13.6
BOS04-5B-3H-2	140-142	8.91	21.18	9.5	-9.1
BOS04-5B-2H-CC	0-6	8.98	21.45	9.8	-7.4
BOS04-5B-4H-1	3-4	9.04	21.68	9.7	-21.0
BOS04-5B-4H-1	36-37	9.37	22.82	6.5	-27.4
BOS04-5B-4H-1	68-69	9.69	23.78	8.0	-24.2
BOS04-5B-4H-1	100-101	10.01	23.96	8.2	-15.0
BOS04-5B-4H-1	132-133	10.33	24.73	5.1	-15.7
BOS04-5B-4H-2	12-13	10.62	25.24	7.2	-21.7
BOS04-5B-4H-2	52-53	11.02	26.37	8.8	-24.4
BOS04-5B-4H-2	76-77	11.26	26.85	6.0	-29.3
BOS04-5B-4H-2	108-109	11.58	27.73	6.6	-22.6



BOS04-5B-4H-2	140-141	11.90	28.30	6.2	-15.0
BOS04-5B-4H-CC	0-10	11.99	28.41	8.4	-9.7
BOS04-5B-5H-1	4-5	12.05	28.46	7.4	-14.3
BOS04-5B-5H-1	36-37	12.37	28.64	4.9	-17.1
BOS04-5B-5H-1	68-69	12.69	28.79	9.1	-11.2
BOS04-5B-5H-1	100-101	13.01	29.13	8.8	-13.7
BOS04-5B-5H-1	132-133	13.33	29.47	7.0	-11.6
BOS04-5B-5H-2	4-5	13.55	29.60	10.9	-23.7
BOS04-5B-5H-2	36-37	13.87	29.74	10.9	-17.6
BOS04-5B-5H-2	68-69	14.19	30.03	6.8	-18.5
BOS04-5B-5H-2	100-101	14.51	30.31	3.9	-18.7
BOS04-5B-5H-2	132-133	14.83	30.60	9.6	-20.2
BOS04-5B-5H-CC	0-7	14.96	30.63	8.5	-23.3
BOS04-5B-6H-1	12-13	15.13	30.69	10.1	-22.8
BOS04-5B-6H-1	44-45	15.45	31.58	7.4	-23.3
BOS04-5B-6H-1	76-77	15.77	32.25	10.3	-23.5
BOS04-5B-6H-1	108-109	16.09	33.14	15.1	-26.6
BOS04-5B-6H-1	140-141	16.41	34.02	22.2	-27.8
BOS04-5B-6H-2	20-21	16.71	34.84	17.4	-28.9
BOS04-5B-6H-2	52-53	17.03	36.12	11.4	-24.7
BOS04-5B-6H-2	84-85	17.35	36.36	16.5	-27.5
BOS04-5B-6H-2	116-117	17.67	36.86	11.3	-27.4
BOS04-5B-6H-2	140-141	17.91	37.55	15.3	-25.7
BOS04-5B-6H-CC	0-8	17.98	37.78	8.5	-24.7
BOS04-5B-7H-1	28-29	18.29	38.52	8.0	-13.4
BOS04-5B-7H-1	60-61	18.61	39.13	7.2	-21.7
BOS04-5B-7H-1	92-93	18.93	39.76	10.0	-20.7
BOS04-5B-7H-1	124-125	19.25	40.69	5.0	-24.1
BOS04-5B-7H-2	4-5	19.55	41.83	15.1	-26.4
BOS04-5B-7H-2	12-13	19.63	42.16	25.4	-28.5
BOS04-5B-7H-2	36-37	19.87	42.69	17.8	-26.5
BOS04-5B-7H-2	68-69	20.19	43.20	16.0	-21.4
BOS04-5B-7H-2	100-101	20.51	43.70	7.3	-24.6
BOS04-5B-7H-2	132-133	20.83	44.36	11.2	-26.0
BOS04-5B-7H-CC	0-6	20.89	44.58	7.2	-27.1
BOS04-5B-8H-1	4-5	21.05	45.15	4.9	-24.4
BOS04-5B-8H-1	36-37	21.37	46.23	9.8	-25.7
BOS04-5B-8H-1	68-69	21.69	46.55	10.6	-20.6
BOS04-5B-8H-1	100-101	22.01	46.83	5.2	-17.4
BOS04-5B-8H-2	4-5	22.55	47.35	2.7	-12.2
BOS04-5B-8H-2	36-37	22.87	47.74	2.6	-10.9
BOS04-5B-8H-2	68-69	23.19	48.14		-10.3
BOS04-5B-8H-CC	0-8	23.39	48.39	8.5	-7.9

BOS04-5B-9H-1	12-13	24.13	49.58	2.8	-17.4
BOS04-5B-9H-1	44-45	24.45	50.07	4.8	-18.4
BOS04-5B-9H-1	76-77	24.77	50.33	5.7	-11.7
BOS04-5B-9H-1	108-109	25.09	50.58	3.6	-20.1
BOS04-5B-9H-1	140-141	25.41	50.84	5.3	-7.7
BOS04-5B-9H-2	20-21	25.71	51.20	5.7	-18.0
BOS04-5B-9H-2	52-53	26.03	51.58	6.8	-23.5
BOS04-5B-9H-2	84-85	26.35	51.96	3.7	-27.1
BOS04-5B-9H-2	116-117	26.67	52.30	12.0	-27.9
BOS04-5B-9H-CC	0-6	26.96	52.61	12.8	-27.5
BOS04-5B-10H-1	4-5	27.05	52.70	12.4	-31.5
BOS04-5B-10H-1	36-37	27.37	53.03	12.6	-30.3
BOS04-5B-10H-1	67-68	27.68	53.29	12.1	-33.6
BOS04-5B-10H-1	100-101	28.01	53.55	8.7	-34.9
BOS04-5B-10H-1	132-133	28.33	53.81	6.0	-20.8
BOS04-5B-10H-2	12-13	28.64	54.17	3.5	-25.2
BOS04-5B-10H-2	44-45	28.96	54.57	5.0	-24.6
BOS04-5B-10H-2	76-77	29.28	54.98	3.6	-30.0
BOS04-5B-10H-2	108-109	29.60	55.44	4.3	-22.6
BOS04-5B-10H-CC	0-6	29.92	55.94	2.8	-22.6
BOS04-5B-11H-1	4-5	30.05	56.13	3.0	-25.8
BOS04-5B-11H-1	36-37	30.37	56.63	5.0	-28.4
BOS04-5B-11H-1	68-69	30.69	57.30	3.1	-12.3
BOS04-5B-11H-1	100-101	31.01	57.98	5.8	-29.0
BOS04-5B-11H-1	132-133	31.33	58.67	6.3	-29.7
BOS04-5B-11H-2	12-13	31.61	59.22	5.7	-32.1
BOS04-5B-11H-2	44-45	31.93	59.83	5.3	-28.9
BOS04-5B-11H-2	76-77	32.25	60.44	3.1	-27.1
BOS04-5B-11H-2	108-109	32.57	61.32	0.4	-22.5
BOS04-5B-11H-CC	0-6	33.00	62.84	0.3	-22.6
BOS04-5B-12H-1	4-5	33.05	63.01	0.4	-24.4
BOS04-5B-12H-1	36-37	33.37	64.13	0.4	-26.0
BOS04-5B-12H-1	68-69	33.69	65.36	0.5	-32.0

## Supplementary References

1. Nicholson, S. E. in *The Limnology, Climatology and Paleoclimatology of the East African Lakes* (eds Johnson, T. C. & Odada, E. O.) 25–56 (Gordon and Breach, New York, 1996).
2. McKay, N. P. A multidisciplinary approach to the late Quaternary paleoclimatology with an emphasis on sub-Saharan West Africa and the last interglacial period (Ph.D. Dissertation, The University of Arizona, Tucson, 2012).
3. Talbot, M. R. & Johannessen, T. A high resolution paleoclimatic record for the last 27,000 years in tropical West Africa from the carbon and nitrogen isotopic composition of lacustrine organic matter. *Earth Planet. Sci. Lett.* 110, 23–37 (1992).
4. Talbot, M. R. & Delibrias, G. A new late-Holocene water-level curve for Lake Bosumtwi, Ghana. *Earth Planet. Sci. Lett.* 47, 336–344 (1980).
5. Brooks, K., et al. Late-Quaternary lowstands of lake Bosumtwi, Ghana: evidence from high-resolution seismic-reflection and sediment-core data. *Palaeogeogr. Palaeoclimatol. Palaeoecol.* 216, 235–249 (2005).
6. Shanahan, T. M. et al. Paleoclimatic variations in West Africa from a record of late Pleistocene and Holocene lake level stands of Lake Bosumtwi, Ghana. *Palaeogeogr. Palaeoclimatol. Palaeoecol.* 242, 287–302 (2006).

## **CHAPTER 3:**

### **Sublacustrine turbidite systems of the Lake Albert Rift, East Africa, from seismic reflection data**

Xuewei Zhang\* and Christopher A. Scholz

Department of Earth Sciences, Syracuse University, Syracuse, New York 13244, USA

\*E-mail: xzhang39@syr.edu

## **Abstract**

Analyses of 2-D and 3-D seismic reflection data from the Lake Albert Rift, East Africa reveal the presence of large channelized turbidite systems, which accumulated during late Pliocene to early Pleistocene when Lake Albert is a deep lake system. Geomorphic parameters of imaged channels were measured and compared with data from river and submarine channels, and it is found that the meander geometry of the sublacustrine turbidite channels is morphologically close to river and submarine channels. In the Semliki River plain area to the southwest of the present lake, turbidite systems from two depositional units connect updip to two different fluvial catchments on the eastern rift shoulder. It is postulated that the turbidites were sourced by hyperpycnal river flows during floods, and there was a change in the sediment source during the accumulation of the two units, caused by drainage reversals due to rift shoulder uplift. Sediment dispersal pathways, changes in depositional facies, and evolution of the sublacustrine turbidite systems appear to be greatly influenced by syndepositional tectonism.

**Keywords:** turbidite; 3-D seismic; meander geometry; Lake Albert; East Africa Rift

## **Introduction**

Deep-water depositional processes have been the focus of many recent studies, and much has been learned about the morphology, architecture, and evolution of turbidite systems, especially those developed along passive continental margins (Kneller, 2003; Peakall et al., 2003; Posamentier, 2003; Posamentier and Kolla, 2003; Pirmez and Imran, 2003; Deptuck et al., 2007; Gee et al., 2007; Gee and Gawthorpe, 2007; Kolla et al., 2007; Posamentier et al., 2007; Wynn et al., 2007; Babonneau et al., 2010; McHargue et al., 2011). However, turbidite systems from non-marine, tectonically active basins, such as lacustrine rift basins, are underexplored and less understood. Compared to passive continental margin submarine environments, lacustrine rift basins are characterized by rapid and spatially variable extensional tectonics (Ebinger, 1989; Gawthorpe and Hurst, 1993; Contreras et al., 2000; Gawthorpe and Leeder, 2000; Lezzar et al., 2002) and high-frequency and high-amplitude lake-level changes (Scholz et al., 2007; McGlue et al., 2008; Lyons et al., 2011), all of which play important roles in controlling the sedimentation of rift lake turbidites.

Quantitative relationships of various planform geomorphic parameters of river channels have been empirically derived (Table 1), including channel width, meander wavelength, amplitude, and mean radius of curvature (Leopold and Wolman, 1957, 1960; Dury, 1965; Ritter et al., 2002). Previous studies have suggested that the meander geometry of submarine channels on passive continental margins is close to that of fluvial channels (Flood and Damuth, 1987;

Clark et al., 1992; Pirmez and Imran, 2003). However, no studies have considered the meander geometry of sublacustrine turbidite channels.

Sublacustrine turbidite systems comprise a large fraction of the sediment volume of lacustrine rift basins, and have been observed from modern deep-water rift valleys, e.g. Lake Baikal (Nelson et al., 1999), Lake Malawi (Soreghan et al., 1999), and Lake Kivu (Zhang et al., 2014), as well as from ancient lacustrine rift basins (Feng et al., 2010). Using 2-D and 3-D seismic reflection data from the Lake Albert rift, East Africa, this paper: 1) makes quantitative comparisons of the planform geometry between sublacustrine turbidite and subaerial fluvial channels; and 2) assesses the source of turbidity currents and the structural controls on the deposition of turbidite systems in this extensional basin.

## **Geological Setting**

The East African Rift System (EARS) is a north-south alignment of rift basins forming a plate boundary on the east side of Africa, and is divided into two structural branches (Ebinger, 1989; Corti, 2009). The western branch of the EARS (i.e. the Western Rift Valley), initiated about 25 million years ago in the late Oligocene (Roberts et al., 2012), is composed of a series of half-graben and full-graben basins, which are occupied by large lake systems. Lake Albert, located at the northern end of the Western Rift Valley, is ~150 km long and ~40 km wide (Fig. 1). The lake occupies an asymmetric full-graben bordered on the northwest by the Bunia Border Fault accommodating most of the extension, and on the southeast by a complex of steeply

dipping faults (Karp et al., 2012; Figs. 1, 2). The boundary faults on either side of the basin have been continuously active throughout the late Cenozoic (Karp et al., 2012). Analyses of seismic reflection data suggest that the main depocenter, with a maximum thickness of ~5 km in the sedimentary section, is located on the northwest side of the basin adjacent to the Bunia Border Fault (Karp et al., 2012). The sedimentary section observed in seismic data extends from the present lake into the Semliki River plain to the southwest (Fig. 1). With a maximum displacement of >1000 m on the sediment-crystalline basement interface, the Semliki Fault (Fig. 3), which is antithetic to the Bunia Border Fault, is the largest intrabasinal fault in the Semliki River plain area, and is probably the northeastward extension of the West Ruwenzori Fault (Fig. 1).

Evidence from mollusk fossils suggests that Lake Albert and Lake Edward/Lake George may have existed as a single large lake, i.e. the paleolake Obweruka, during the late-Miocene to mid-Pliocene times (Van Damme and Pickford, 2003). At ~2.5 Ma in the early Pleistocene, paleolake Obweruka is postulated to have broken up into the southern and northern basins by uplift of the Ruwenzori Mountains (Van Damme and Pickford, 2003). Large drainage systems at the northern end of the Western Rift Valley, including the Kafu, Katonga, and Kagera Rivers (Fig. 1), were once westward flowing during the Miocene, Pliocene and part of the Pleistocene (Beadle, 1981). Today, these rivers are much diminished and flow bidirectionally, divided by a broad upwarp in western Uganda (McGlue et al., 2006). The drainage reversals which gave birth



to Lakes Kyoga and Victoria (Beadle, 1981) were caused by rift-related flank uplift beginning in the Miocene and continuing into the Pleistocene (Kendall, 1969).

The Lake Albert Rift has experienced long-term environmental changes, from a continuously open-lacustrine, deep lake system in the Miocene and Pliocene, to an alternating shallow-lacustrine and fluvial system in the mid- and late-Pleistocene (Karp et al., 2012; Fig. 4). Modern-day Lake Albert has an average depth of ~25 m, and is an open hydrologic system that outflows northward through the Albert Nile, and receives its major input from the Semliki River in the southwest and the Victoria Nile in the northeast (Fig. 1).

This study focuses on the stratigraphic interval accumulated during late Pliocene to early Pleistocene (by correlation with Karp et al., 2012; Figs. 3, 4). By correlation with drill core data (Sserubiri, 2011; Karp et al., 2012), the studied interval is composed of organic-rich shales interbedded moderately-sorted quartz sandstones containing pyrites (Fig. 4), indicating reducing, deep lacustrine depositional conditions.

## **Datasets and Methodology**

The data sets used in this study include the Semliki 3-D seismic survey on the southern coast of Lake Albert and a dense grid of offshore 2-D seismic reflection profiles covering the entire lake (Fig. 1). The commercially-acquired 3-D and 2-D seismic data are zero-phase and normal polarity, following SEG conventions. The Semliki 3-D seismic data were acquired in 2004 using a dynamite source, and have a line spacing of 25 m and a dominant frequency of ~25

Hz. The offshore 2-D seismic data acquired in 2002 used a 120 c.i. air gun array as a seismic source, and have a line spacing of 1.5–3.5 km and a dominant frequency of ~55 Hz.

Using 3-D seismic data, a variety of seismic attributes can be used to image and visualize ancient depositional systems in the subsurface (Posamentier, 2002; Posamentier and Kolla, 2003; Posamentier et al., 2007). Seismic attributes extracted on stratal slices and reflection configurations within the studied interval were analyzed to assess turbidite systems of the Lake Albert rift. To better characterize the turbidite systems, interpretations of various seismic attributes were integrated. These attributes include instantaneous amplitude, RMS amplitude, instantaneous phase, coherence, and ‘edge detection’ (a seismic attribute for the detection of geologic boundaries).

To quantitatively compare channel geometry between sublacustrine turbidite and subaerial fluvial systems, measurements of meander wavelength, amplitude, radius of curvature, channel width, and sinuosity were made at the individual meander level on seismic attribute slices. Because the widths of the channels in some cases display large variations, five evenly-spaced measurements were taken to estimate the mean width of each channel meander. Intrabasinal faults were interpreted from the Semliki 3-D seismic volume in order to assess the structural control of turbidite sedimentation in the Semliki River plain area.

## **Results**

### ***Intrabasinal Faults Observed in The Semliki 3-D Seismic Survey***

A number of intrabasinal faults were interpreted from the Semliki 3-D seismic volume, with some showing surface expressions. Digital elevation models indicate that the surface scarp of the Semliki Fault has relief of ~0.5 m in the northeast and >100 m in the southwest part of the Semliki 3-D seismic survey, indicating its recent activity. Surface scarps are also associated with the arcuate faults striking subparallel or at low-angle to the Semliki Fault in the eastern and northeastern part of the Semliki 3-D seismic survey (Fig. 5). The Semliki Fault and those described are syndepositional to the studied interval, as indicated by isochron mapping (Fig. 5). A fault-related fold, also syndepositional to the studied interval, developed on the hanging wall of the Semliki Fault (Figs. 3, 5). The approximately SW-NE and NW-SE striking faults in the western and southwestern part of the Semliki 3-D seismic survey appear to be postdepositional to the studied interval (Fig. 5); there are no apparent changes in sedimentary thickness across these faults.

### ***Turbidite Systems***

Turbidite systems that developed during different episodes were observed from the Semliki 3-D and offshore 2-D seismic data. In the Semliki River plain area, channelized turbidite systems were observed on a number of seismic surfaces, with the most extensively distributed ones associated with the 'Green' and 'Purple' seismic surfaces (Fig. 3). The 'Green' seismic surface was characterized by a highly continuous, high-amplitude seismic reflection event; the 'Purple' seismic surface, which is ~50 m above the 'Green' surface, is associated with a continuous,

medium- to high-amplitude seismic reflection event. Depositional thickness between the ‘Green’ and ‘Purple’ surfaces is largely correlated with syndepositional faulting and fault-related folding, and varies from ~30 ms TWTT (Two-way Travel Time; ~25 m) in the southeast to ~80 ms TWTT (~70 m) in the northwest of the Semliki 3-D seismic survey (Fig. 5).

Turbidity-flow channel and lobe elements were imaged by various seismic attributes extracted on the ‘Green’ seismic surface, including but not limited to instantaneous amplitude (Fig. 6A), RMS amplitude (Fig. 6B), and ‘edge detection’ (Fig. 6C). Characterized by a coupled flat channel-top and concave-up channel-base seismic reflection configuration, the sublacustrine channels of the ‘Green’ depositional unit (Figs. 7, 8) are ~5–25 km long and ~120–250 m wide within the Semliki 3-D seismic survey. The widths of the channels may vary significantly, due to meander growth (Fig. 6A). The channels are low to moderately sinuous, with sinuosity varying from 1.01 to 1.28. Some channels exhibit bifurcation, with the angle of bifurcation about 30°–45° (Figs. 6A, 7). At least one of these channels has an attached lobe (Fig. 6A), and the channel-to-lobe transition is associated with an intrabasinal fault. The channels are oriented approximately E-W, with an exception of a SW-NE running channel, which may connect up-dip to a sublacustrine fan on the footwall of the Semliki Fault (Fig. 7). The fan is characterized by high-amplitude anomalies on seismic attribute images (Fig. 6B), and shows channel-like features in cross-sectional views.

Later development of sublacustrine channel and fan systems in the Semliki River plain area can be observed on horizon slices between 44 ms TWTT (Fig. 9A) and 60 ms TWTT (Fig. 9B)

above the 'Green' seismic surface (Fig. 10); the bases of all imaged channels correspond to the same reflection event, i.e. the 'Purple' seismic surface (Fig. 11). These channels are better imaged on the stratal slice generated by amplitude extraction on the 'Purple' surface (Fig. 9C); more channels are observed on the stratal slice that represents a geological-time surface (Zeng and Hentz, 2004), compared to the horizon slices that are less chronologically significant. The turbidite channels of the 'Purple' depositional unit show lengths, widths, and depths comparable to those of the channels of the 'Green' depositional unit. Channel width of the 'Purple' unit shows variations of as much as ~70 %. The channels are of low to moderate sinuosity, with values ranging from 1.02 to 1.34. Orientated SE-NW, these channels are probably secondary and connected updip to the sublacustrine fan on the footwall of the Semliki Fault (Figs. 9, 10). Although it was also observed on seismic amplitude images of the 'Green' seismic surface (Fig. 6B), sedimentation of the fan was probably more active during accumulation of the 'Purple' unit, where a higher degree of channelization of the fan was observed. Compared to the turbidite systems of the 'Green' unit, a distributary channel network and complex crosscutting fabric characterize the turbidite systems of the 'Purple' unit (Fig. 10).

Large turbidite systems were also observed in the northern part of the Lake Albert rift. Sublacustrine fans that are ~300–350 m below the 'Green' and 'Purple' depositional units were revealed from offshore 2-D seismic profiles (Fig. 12). Deposited against the N. Toro Bunyoro Fault, the mounded sublacustrine fans show bidirectional downlap on seismic profiles in the strike direction (Fig. 12A), similar to the seismic reflection configuration of submarine basin-

floor fans (e.g. Mitchum, 1985), and are progradational on seismic profiles in the dip direction (Fig. 12B). One of these fans appears to be channelized (Fig. 12A); the channels on the fan, also characterized by coupled flat channel-top and concave-up channel-base reflections, probably form a distributary pattern like its submarine counterparts (e.g. the Amazon Fan, Pirmez and Imran, 2003).

## **Discussion**

### ***Meander Geometry***

Channel width ( $W$ ), meander wavelength ( $\lambda$ ), amplitude ( $A$ ), and mean radius of curvature ( $R_m$ ) of river channels have all been observed to scale with  $W$  as linear or power-law functions with exponents close to unity (Leopold and Wolman, 1957, 1960; Dury, 1965; Ritter et al., 2002). Previous work demonstrates that the empirical relationships derived from river channels apply to sinuous submarine channels as well (Flood and Damuth, 1987; Clark et al., 1992; Pirmez and Imran, 2003).

Compared to submarine channels, the sublacustrine channels of the Lake Albert rift are much smaller in scale; values of  $\lambda$ ,  $A$ ,  $R_m$ , and  $W$  are only about 1/10 to 1/5 of those observed from the submarine channels studied by Clark et al. (1992) and Pirmez and Imran (2003). The values of  $\lambda$ ,  $A$ , and  $R_m$  for all measured meanders are plotted versus  $W$  (Fig. 13A, 13B, 13C). The regressions derived from measurements of the sublacustrine channels are similar to submarine channels (Flood and Damuth, 1987; Clark et al., 1992; Pirmez and Imran, 2003), and

correspond closely with those derived from river data by Leopold and Wolman (1957, 1960) and Ritter et al. (2002). The linear best-fit between  $\lambda$  and  $R_m$  (Fig. 13D) is also similar to that observed in river channels (Leopold and Wolman, 1957).

Sinuosity ( $S_i$ ) also scales with channel width, but as a negative power-law function (Fig. 13E). A negative power-law relationship between sinuosity and channel width was also demonstrated by Hickson and Lowe (2002), based on data of numerous modern submarine channels from Clark and Pickering (1996). Accordingly, the planform morphology of turbidite channels, including both submarine and sublacustrine channels, and that of fluvial channels are not significantly different.

### ***Sediment Sources***

Turbidity currents can be initiated by slope failures triggered by earthquakes, meteorite impacts, storms, and sea/lake level changes (Normark and Piper, 1991; Piper et al., 1991; Bralower et al., 1998; Canals et al., 2004; Puig et al., 2004; Gee et al., 2006; Girardclos et al., 2007), and by hyperpycnal river flows during floods (Mulder et al., 2003; Plink-Björklund and Steel, 2004; Dadson et al., 2005; Khripounoff et al., 2009; Osleger et al., 2009; Bourget et al., 2010). Hyperpycnal flows form in marine environments when rivers discharge into the oceans with suspended concentrations in excess of  $36 \text{ kg/m}^3$ ; they are more frequent in lakes where only small sediment concentrations are necessary to induce plunging behavior (Mulder et al., 2003).

Within the studied interval of the Lake Albert basin, there is no evidence of large-scale sediment failures and related mass transport deposits that can be observed from the 3-D and 2-D seismic data. Sediment failure on slopes is therefore not likely the trigger of turbidity currents over the studied interval. We postulate that the turbidite systems are connected to onshore drainage basins (Fig. 14), and that hyperpycnal river flows during floods are the most likely mechanism for the initiation of turbidity currents.

In the Semliki River plain area, turbidite systems of the 'Green' and 'Purple' depositional units can be traced landward to two of the largest drainage basins on the eastern rift shoulder, marking a possible change in the sediment source between accumulation of the two units. The turbidite channels of the 'Green' unit are mainly orientated E-W. They were probably primarily fed by the Kafu River catchment from northeast (Fig. 14; Fig. 15A), which drained an area of  $\sim 50,000 \text{ km}^2$  over a distance of  $\sim 500 \text{ km}$  prior to the drainage reversal (Beadle, 1981). The later turbidite systems of the 'Purple' unit are oriented approximately SE-NW, and were probably sourced by the Muzizi River (Fig. 15B). The Muzizi River catchment is located to the west of the axis of upwarp (Figs. 1, 14), and therefore was not reversed when the rift shoulder was uplifted. Also oriented SE-NW, the Muzizi River drains an area of  $\sim 4,000 \text{ km}^2$  over a distance of  $\sim 100 \text{ km}$ . Sourced by the Muzizi River catchment from southeast, the turbidite fan on the footwall of the Semliki Fault was more active during the accumulation of the 'Purple' unit than during the deposition of the 'Green' unit, and it probably served as a secondary sediment source feeding the turbidite channels of the 'Purple' unit (Figs. 10, 14B, 15B) and the SW-NE running channel of



the 'Green' unit (Figs. 7, 15A). The sublacustrine fans deposited along the N. Toro Bunyoro Fault in the northern part of the lake were also most likely sourced by hyperpycnal river flows (Figs. 12, 14). The Tonya River drainage basin, which has a drainage area of ~ 800 km<sup>2</sup>, was probably the source of the sublacustrine fans.

The change in the sediment source of the turbidites in the Semliki River plain area between accumulation of the 'Green' and 'Purple' units was probably a consequence of tectonic activity. We postulate that such change in the sediment source is due to a drainage reversal (Beadle, 1981) as a result of complex rift-shoulder uplift. Analysis of the Semliki 3-D seismic data suggests that during the accumulation of the studied interval, Lake Albert was a much larger and deeper lake. It occupied the northern basin of the paleolake Obweruka (Van Damme and Pickford, 2003), and covered the Semliki River plain area. Seismic stratigraphic evidence, including orientation and distribution of sublacustrine channels (e.g. these from the 'Green' unit and other older units) and dip direction of shingled clinofolds (~100–300 m beneath the 'Green' unit), suggests that the Kafu River drainage system had been actively delivering terrigenous sediments to the Semliki River plain area prior to the accumulation of the 'Purple' depositional unit. We postulate that during the accumulation of the 'Purple' unit, the Kafu River had already reversed as a result of rift-flank uplift, thereby limiting sediments inputs. The exact timing of these drainage changes awaits further detailed geochronological analyses and additional subsurface data.

Axial turbidite systems typical of confined, linear rift-lake basins (Scholz et al., 1998; Nelson et al., 1999; Soreghan et al., 1999) were not observed in the Semliki River plain area. However, Lake Albert was a much larger and deeper lake system during the accumulation of the studied interval in the late Pliocene to early Pleistocene, and axial turbidite systems, if present, were likely located farther southwest beyond the coverage of the Semliki 3-D seismic survey. Since the middle Pleistocene, Lake Albert has been much shallower, characterized by alternating shallow-lacustrine and fluvial-deltaic depositional environments (Karp et al., 2012).

### ***Structural Control of Turbidite Sedimentation***

Syndepositional tectonism influences rift topography, evolution of drainage systems, and the sedimentary patterns of extensional basins (Gawthorpe and Hurst, 1993; Ravnas and Steel, 1998; Gupta et al., 1999; Gawthorpe and Leeder, 2000). Sediment dispersal pathways, changes in depositional facies, and evolution of the sublacustrine turbidite systems of the Lake Albert Rift are largely controlled by syndepositional tectonism.

The sediment dispersal pathways of the 'Purple' depositional unit are structurally controlled. In the Semliki River plain area, the channels of the 'Purple' unit are connected updip through relay ramps to the sublacustrine fan on the footwall of the Semliki Fault. The fault-controlled relay ramp played an important role in directing turbidity currents downbasin (Figs. 10 and 15B), similar to the modern turbidite systems observed in the south Rukuru area of the Lake Malawi rift (Soreghan et al., 1999).

The transition between different turbidity-flow depositional elements is also structurally controlled. In the Semliki River plain area, one of the turbidite channels of the ‘Green’ depositional unit has an attached lobe, and the channel-to-lobe transition is associated with an intrabasinal fault (Figs. 6B, 7), which was active during deposition. A channel-to-lobe transition associated with syndepositional faulting has also been documented by Adeogba et al. (2005) in their study of submarine turbidite systems on the Niger Delta continental slope.

The turbidite channels of the ‘Green’ and ‘Purple’ units are transient systems. Neither significant lateral accretion nor apparent vertical aggradation is observed, although some channels do show evidence of meander growth. The channels are only minimally to moderately sinuous, with the highest sinuosity of ~1.4, which is significantly lower than that of high-sinuosity submarine channels (e.g. Gee et al., 2007). It is, therefore, suggested that the turbidite channels discussed here only correspond to the first stage of the 3-stage evolution model (i.e. initiation and meander growth, equilibrium-phase aggradation, and abandonment) for submarine channels proposed by Peakall et al (2003).

Sublacustrine channels in tectonically active rift basins, such as the Lake Albert Rift, are less likely to undergo all the three evolutionary stages. Spatially variable basin subsidence (Ebinger, 1989; Gawthorpe and Hurst, 1993; Gawthorpe and Leeder, 2000), complex rift shoulder uplift (Contreras et al., 2000; Lezzar et al., 2002), and high-frequency and high-amplitude lake-level changes (Scholz et al., 2007; McGlue et al., 2008; Lyons et al., 2011) are typical of lacustrine rift basins, and these factors, alone or combined, may switch off

channelization processes shortly after channel initiation in rift lakes, preventing sublacustrine channels from further evolution.

## **Conclusions**

The Semliki 3-D seismic survey covering the southern coast of Lake Albert combined with offshore 2-D seismic data reveal the existence of large sublacustrine channels and fans, which accumulated during late Pliocene to early Pleistocene. The turbidite channels are minimally to moderately sinuous, and commonly present themselves by coupled flat channel-top and concave-up channel-base reflections. The channels are ~5 to 25 km long and ~100 to 300 m wide. Bifurcation, channel-to-lobe transition, complex cross-cutting, and distributary channel networks are observed.

Width, sinuosity, meander wavelength, amplitude, and radius of curvature of the sublacustrine turbidite channels were measured and compared with the empirically derived relationships from river data. The meander geometry of the sublacustrine channels is morphologically close to fluvial channels, as in the case of submarine channels.

In the Semliki River Plain area, turbidite systems from two depositional units can be traced landward toward two of the largest drainage basins on the eastern shoulder of the Lake Albert Rift, suggesting hyperpycnal river flow origin of the turbidity currents and a change in the sediment source, probably caused by regional catchment adjustments due to rift shoulder uplift.

Sediment dispersal pathways, channel-to-lobe transitions, and evolution of the sublacustrine turbidite systems are greatly influenced by syndepositional tectonism.

### **Acknowledgements**

We are very thankful to the reviewers for their constructive comments. Special thanks go to Bruce Wilkinson and Peng Gao for their substantial review of the early versions of this paper. We gratefully acknowledge Tullow Oil plc and the Uganda Government for providing the 3-D seismic data for this research. Support for the research is provided by Anadarko, BP, Chevron, ExxonMobil, Petrobras, Shell, Statoil, and Tullow.

## References

- Adeogba, A.A., McHargue, T.R., Graham, S.A., 2005. Transient fan architecture and depositional controls from near-surface 3-D seismic data, Niger Delta continental slope. AAPG Bulletin 89, 627–643.
- Beadle, L.C., 1981. The inland waters of tropical Africa: an introduction to tropical limnology. Longman, London.
- Babonneau, N., Savoye, B., Cremer, M., Bez, M., 2010. Sedimentary architecture in meanders of a submarine channel: detailed study of the present Congo turbidite channel (zaiango project). Journal of Sedimentary Research 80, 852–866.
- Bourget, J., Zaragosi, S., Mulder, T., Schneider, J.-L., Garlan, T., Van Toer, A., 2010. Hyperpycnal-fed turbidite lobe architecture and recent sedimentary processes: a case study from the Al Batha turbidite system, Oman margin. Sedimentary Geology 229, 144–159.
- Bralower, T.J., Paul, C.K., Leckie, P.M., 1998. The Cretaceous–Tertiary boundary cocktail: Chicxulub impact triggers margin collapse and extensive sediment gravity flows. Geology 26, 331–334.
- Canals, M., Lastras, G., Urgeles, R., Casamor, J.L., Mienert, J., Cattaneo, A., De Batist, M., Haflidason, H., Imbo, Y., Laberg, J.S., Locat, J., Long, D., Longva, O., Massoni, D.G., Sultan, N., Trincardi, F., Bryn, P., 2004. Slope failure dynamics and impacts from seafloor and shallow sub-seafloor geophysical data: case studies from the COSTA project. Marine Geology 213, 9–72.

- Clark, J.D., Kenyon, N.H., Pickering, K.T., 1992. Quantitative analysis of the geometry of submarine channels: implications for the classification of submarine fan. *Geology* 20, 633–636.
- Clark, J.D., Pickering, K.T., 1996. Submarine channels processes and architecture. Vallis Press, London.
- Contreras, J., Anders, M.H., Scholz, C.H., 2000. Growth of a normal fault system: observations from the Lake Malawi basin of the east African rift. *Journal of Structural Geology* 22, 159–168.
- Corti, G., 2009. Continental rift evolution: from rift initiation to incipient break-up in the Main Ethiopian Rift, East Africa. *Earth-Science Reviews* 96, 1–53.
- Dadson, S., Hovius, N., Pegg, S., Dade, W.B., Horng, M.J., Chen, H., 2005. Hyperpycnal river flows from an active mountain belt. *Journal of Geophysical Research* 110, F04016, doi: 0.1029/2004JF000244.
- Deptuck, M.E., Sylvester, Z., Pirmez, C., O’Byrne, C., 2007. Migration-aggradation history and 3-D seismic geomorphology of submarine channels in the Pleistocene Benin-major Canyon, western Niger Delta slope. *Marine and Petroleum Geology* 24, 406–433.
- Dury, G.H., 1965. Theoretical implications of underfit streams. USGS Professional Paper, 452-C.
- Ebinger, C.J., 1989. Tectonic development of the western branch of the East African rift system. *GSA Bulletin* 101, 885–903.

- Feng, Z., Zhang, S., Cross, T.A., Feng, Z., Xie, X., Zhao, B., Fu, X., Wang, C., 2010. Lacustrine turbidite channels and fans in the Mesozoic Songliao basin, China. *Basin Research* 22, 96–107.
- Flood, R.D., Damuth, J. E., 1987. Quantitative characteristics of sinuous distributary channels on the Amazon deep-sea fan. *GSA Bulletin* 98, 728–738.
- Gawthorpe, R.L., Hurst, J.M., 1993. Transfer zones in extensional basins: their structural style and influence on drainage development and stratigraphy. *Journal of Geological Society London* 150, 1137–1152.
- Gawthorpe, R.L., Leeder, M.R., 2000. Tectono-sedimentary evolution of active extensional basins. *Basin Research* 12, 195–218.
- Gee, M.J.R., Gawthorpe, R.L., Friedmann, S.J., 2006. Triggering and evolution of a giant submarine landslide, offshore Angola, revealed by 3D seismic stratigraphy and geomorphology. *Journal of Sedimentary Research* 76, 9–19.
- Gee, M.J.R. Gawthorpe, R.L., 2007. Early evolution of submarine channels offshore Angola revealed by three-dimensional seismic data. In: Davies, R.J., Posamentier, H.W., Wood, L.S., Cartwright, J.A. (Eds.), *Seismic geomorphology: applications to hydrocarbon exploration and production*. Geological Society of London, Special Publication 277, pp. 223–235.



- Gee, M.J.R., Gawthorpe, R.L., Bakke, K., Friedmann, S.J., 2007. Seismic geomorphology and evolution of submarine channels from the Angolan continental margin. *Journal of Sedimentary Research* 77, 433–446.
- Girardclos, S., Schmidt, O.T., Sturm, M., Ariztegui, D., Pugin, A., Anselmetti, F.S., 2007. The 1996 AD delta collapse and large turbidite in Lake Brienz. *Marine Geology* 241, 137–154.
- Gupta, S., Underhill, J.R., Sharp, I.R., Gawthorpe, R.L., 1999. Role of fault interactions in controlling synrift sediment dispersal patterns: Miocene, Abu Alaqa Group, Suez Rift, Sinai, Egypt. *Basin Research* 11, 167–189.
- Hickson, T.A., Lowe, D.R., 2002. Facies architecture of a submarine fan channel-levee complex: the Juniper Ridge Conglomerate, Coalinga, California. *Sedimentology* 49, 335–342.
- Karp, T., Scholz, C.A., McGlue, M.M., 2012. Structure and stratigraphy of the Lake Albert Rift, East Africa: observations from seismic reflection and gravity data. In: Nummedal, D., Bartov, Y. (Eds.), *Lacustrine Sandstone Reservoirs and Hydrocarbon Systems*. AAPG Memoir 95, pp. 299–318.
- Kendall, R.L., 1969. An ecological history of the Lake Victoria basin. *Ecological Monographs* 39, 121–176.
- Khripounoff, A., Vangriesheim, A., Crassous, P., Etoubleau, J., 2009. High frequency of sediment gravity flow events in the Var submarine canyon (Mediterranean Sea). *Marine Geology* 263, 1–6.

- Kneller, B., 2003. The influence of flow parameters on turbidite slope channel architecture. *Marine and Petroleum Geology* 20, 901–910.
- Kolla, V., Posamentier, H.W., Wood, L.J., 2007. Deep-water and fluvial sinuous channels-characteristics, similarities and dissimilarities, and modes of formation. *Marine and Petroleum Geology* 24, 388–405.
- Lardal, T., Talbot, M.R., 2002. Basin neotectonics of Lakes Edward and George, East African Rift. *Palaeogeography, Palaeoclimatology, Palaeoecology* 187, 213–232.
- Leopold, L.B., Wolman, M.G., 1957. River channel patterns: braided, meandering and straight. *USGS Professional Papers*, 282-B.
- Leopold, L.B., Wolman, M.G., 1960. River meanders. *GSA Bulletin* 71, 769–794.
- Lezzar, K.E., Tiercelin, J.-J., Le Turdu, C., Cohen, A.S., Reynolds, D.J., Le Gall, B., Scholz, C.A., 2002. Control of normal fault interaction on the distribution of major Neogene sedimentary depocenters, Lake Tanganyika, East African Rift. *AAPG Bulletin* 86, 1027–1059.
- Lyons, R.P., Scholz, C.A., Buoniconti, M.R., Martin, M.R., 2011. Late Quaternary stratigraphic analysis of the Lake Malawi Rift, East Africa: an integration of drill-core and seismic-reflection data. *Palaeogeography, Palaeoclimatology, Palaeoecology* 303, 20–37.
- McGlue, M.M., Scholz, C.A., Karp, T., Ongodia, B., Lezzar, K., 2006. Facies architecture of flexural margin lowstand delta deposits in Lake Edward, East African Rift: constraints from seismic reflection imaging. *Journal of Sedimentary Research* 76, 942–958.

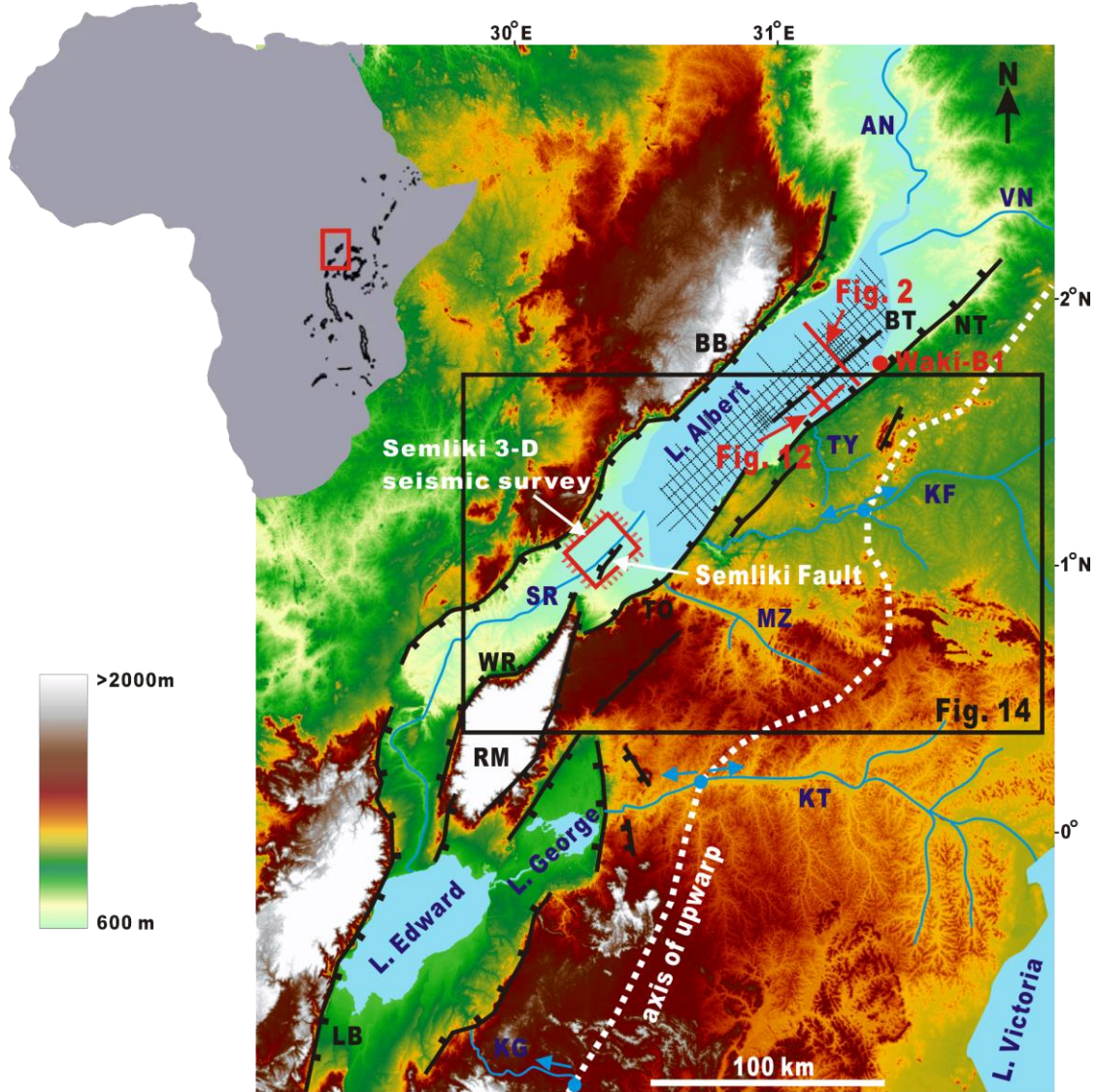
- McGlue, M.M., Lezzar, K.E., Cohen, A.S., Russell, J.M., Tiercelin, J.-J., Felton, A.A., Mbede, E., Nkotagu, H.H., 2008. Seismic records of late Pleistocene aridity in Lake Tanganyika, tropical East Africa. *Journal of Paleolimnology* 40, 635–653.
- McHargue, T., Pyrcz, M.J., Sullivan, M.D., Clark, J., Fildani, A., Romans, B., Covault, J., Levy, M., Posamentier, H.W., Drinkwater, N., 2011. Architecture of turbidite channel systems on the continental slope: patterns and predictions. *Marine and Petroleum Geology* 28, 728–743.
- Mitchum, R. M., 1985. Seismic stratigraphic expression of submarine fans. *AAPG Memoir* 39, pp.117–138.
- Mulder, T., Syvitski, J.P.M., Migeon, S., Faugeres, J.C., Savoye, B., 2003. Marine hyperpycnal flows: initiation, behavior and related deposits. A review. *Marine and Petroleum Geology* 20, 861–882.
- Nelson, C.H., Karabanov, E.B., Colman, S.M., Escutia, C., 1999. Tectonic and sediment supply control of deep rift lake turbidite system, Lake Baikal, Russia. *Geology* 27, 163–166.
- Normark, W.R., Piper, D.J.W., 1991. Initiation processes and flow evolution of turbidity currents: implications for the depositional record. In Osboren, R.H. (Ed.), *From shoreline to abyss*. SPEM Special Publication, 46, pp. 207–230.
- Osleger, D.A., Heyvaert, AC., Stoner, J.S., Verosub, K.L., 2009. Lacustrine turbidites as indicators of Holocene storminess and climate: Lake Tahoe, California and Nevada. *Journal of Paleolimnology* 42, 103–122.

- Peakall, J., McCaffrey, B., Kneller, B., 2003. A process model for the evolution, morphology and architecture of sinuous submarine channels. *Journal of Sedimentary Research* 70, 434–448.
- Piper, D.J.W., Cochonat, P., Morrison, M.L., 1991. The sequence of events around the epicentre of the 1929 Grand Banks earthquake: initiation of debris flows and turbidity current inferred from sidescan sonar. *Sedimentology* 46, 79–97.
- Pirmez, C., Imran, J., 2003. Reconstruction of turbidity currents in Amazon Channels. *Marine and Petroleum Geology* 20, 823–849.
- Plink-Björklund, P., Steel, R.J., 2004. Initiation of turbidity currents: outcrop evidence for Eocene hyperpycnal flow turbidites. *Sedimentary Geology* 165, 29–52.
- Posamentier, H.W., 2002. Sequence stratigraphy past, present and future, and the role of 3-D seismic data. In Armentrout, J.M., Rosen, N.C. (Eds.), *Sequence stratigraphic models for exploration and production: evolving methodology, emerging models, and application histories*. 22nd Annual GCSSEPM Foundation Bob F. Perkins Research Conference, pp. 37–54.
- Posamentier, H.W., 2003. Depositional elements associated with a basin floor channel-levee system: case study from the Gulf of Mexico. *Marine and Petroleum Geology* 20, 677–690.
- Posamentier, H.W., Kolla, V., 2003. Seismic geomorphology and stratigraphy of depositional elements in deep-water settings. *Journal of Sedimentary Research* 73, 367–388.

- Posamentier, H.W., Davies, R.J., Cartwright, J.A., Wood, L.J., 2007. Seismic geomorphology: an overview. In: Davies, R.J., Posamentier, H.W., Wood, L.S., Cartwright, J.A. (Eds.), Seismic geomorphology: applications to hydrocarbon exploration and production. Geological Society of London, Special Publication 277, pp. 1–14.
- Puig, P., Ogston, A.S., Mullenbach, B.L., Nittrouer, C.A., Parsons, J.D., Sternberg, R.W., 2004. Storm-induced sediment gravity flows at the head of the Eel submarine canyon, northern California margin. *Journal of Geophysical Research* 109, C03019m doi: 10.1029/2003JC001918.
- Ritter, D.F., Kochel, R.C., Miller, J.R., 2002. *Process Geomorphology*, 4th Edition. McGraw-Hill Higher Education, New York.
- Ravnas, R., Steel, R.J., 1998. Architecture of marine rift-basin successions. *AAPG Bulletin* 82, 110–146.
- Roberts, E.M., Stevens, N.J., O'Connor, P.M., Dirks, P.H. G.M., Gottfried, M.D., Clyde, W.C., Armstrong, R.A., Kemp, A.I.S., Hemming, S., 2012. Initiation of the western branch of the East African Rift coeval with the eastern branch. *Nature Geoscience* 5, 289–294.
- Scholz, C.A., Moore, T.C., Jr., Hutchinson, D.R., Golmshtok, A.J., Klitgord, K.D., Kurotchkin, A.G., 1998. Comparative sequence stratigraphy of low-latitude versus high-latitude lacustrine rift basins: seismic data examples from the East African and Baikal rifts. *Palaeogeography, Palaeoclimatology, Palaeoecology* 140, 201–420.

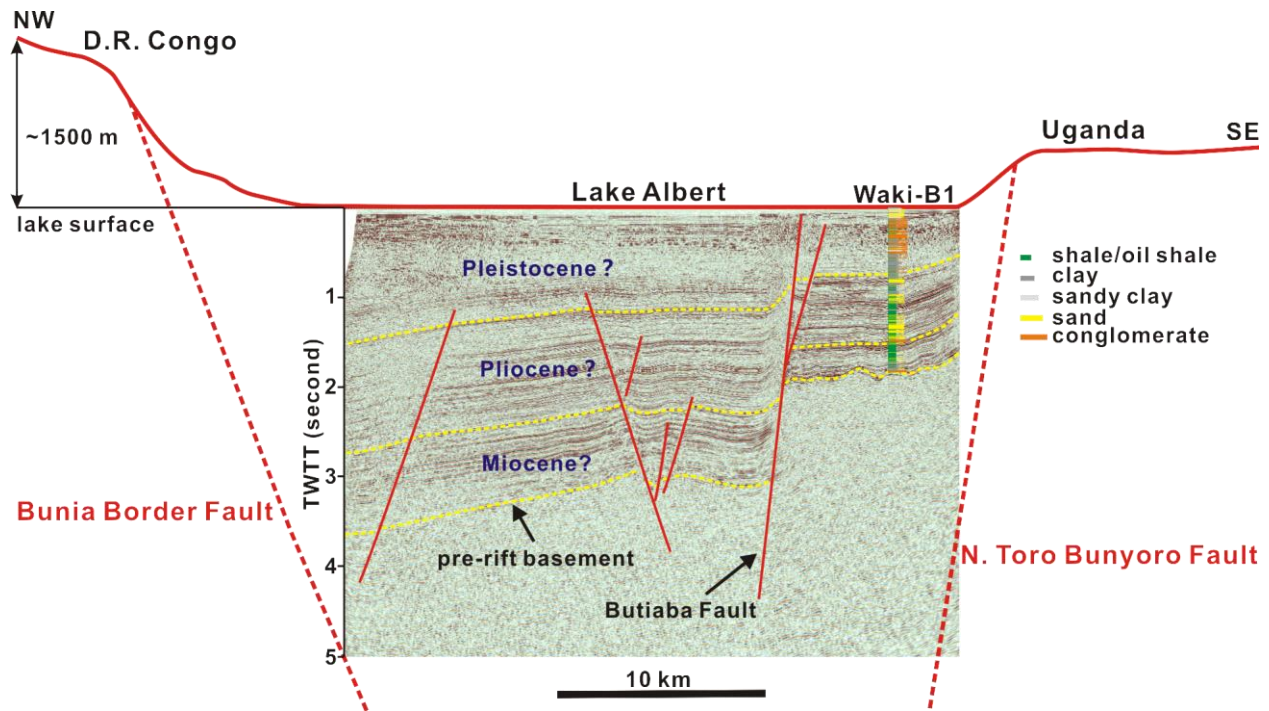
- Scholz, C.A., Johnson, T.C., Cohen, A.S., King, J.W., Peck, J.A., Overpeck, J.T., Talbot, M.R., Brown, E.T., Kalindekaffe, L., Amoako, P.Y.O., Lyons, R.P., Shanahan, T.M., Castaneda, I.S., Heil, C.W., Forman, S.L., McHargue, L.R., Beuning, K.R., Gomez, J., Pierson, J., 2007. East African megadroughts between 135 and 75 thousand years ago and bearing on early-modern human origins. *Proceedings of the National Academy of Sciences* 104, 16416–16421.
- Soreghan, M.J., Scholz, C.A., Wells, J., 1999. Coarse-grained, deep-water sedimentation along a border fault margin of Lake Malawi, Africa: seismic stratigraphic analysis. *Journal of Sedimentary Research* 69, 832–846.
- Sserubiri, T., 2011. A stratigraphic and paleoenvironmental assessment of the central Lake Albert rift basin—Uganda from exploration well geochemical data. Master Thesis, Syracuse University, New York, U.S.A.
- Van Damme, D., Pickford, M., 2003. The late Cenozoic Thiaridae (Mollusca, Gastropoda, Cerithioidea) of the Albertine Rift Valley (Uganda-Congo) and their bearing on the origin and evolution of the Tanganyikan thalassoid malacofauna. *Hydrobiologia* 498, 1–83.
- Wynn, R.B., Cronin, B.T., Peakall, J., 2007. Sinuous deep-water channels: genesis, geometry and architecture. *Marine and Petroleum Geology* 24, 341–387.
- Zeng, H., Hentz, T.F., 2004. High-frequency sequence stratigraphy from seismic sedimentology: Applied to Miocene, Vermilion Block 50, Tiger Shoal area, offshore Louisiana. *AAPG Bulletin* 88, 153–174.

Zhang, X., Scholz, C.A., Hecky, R.E., Wood, D.A., Zal, H.J., Ebinger, C.J., 2014. Climatic control of the late Quaternary turbidite sedimentology of Lake Kivu, East Africa: Implications for deep mixing and geologic hazards. *Geology* 42, 811–114.

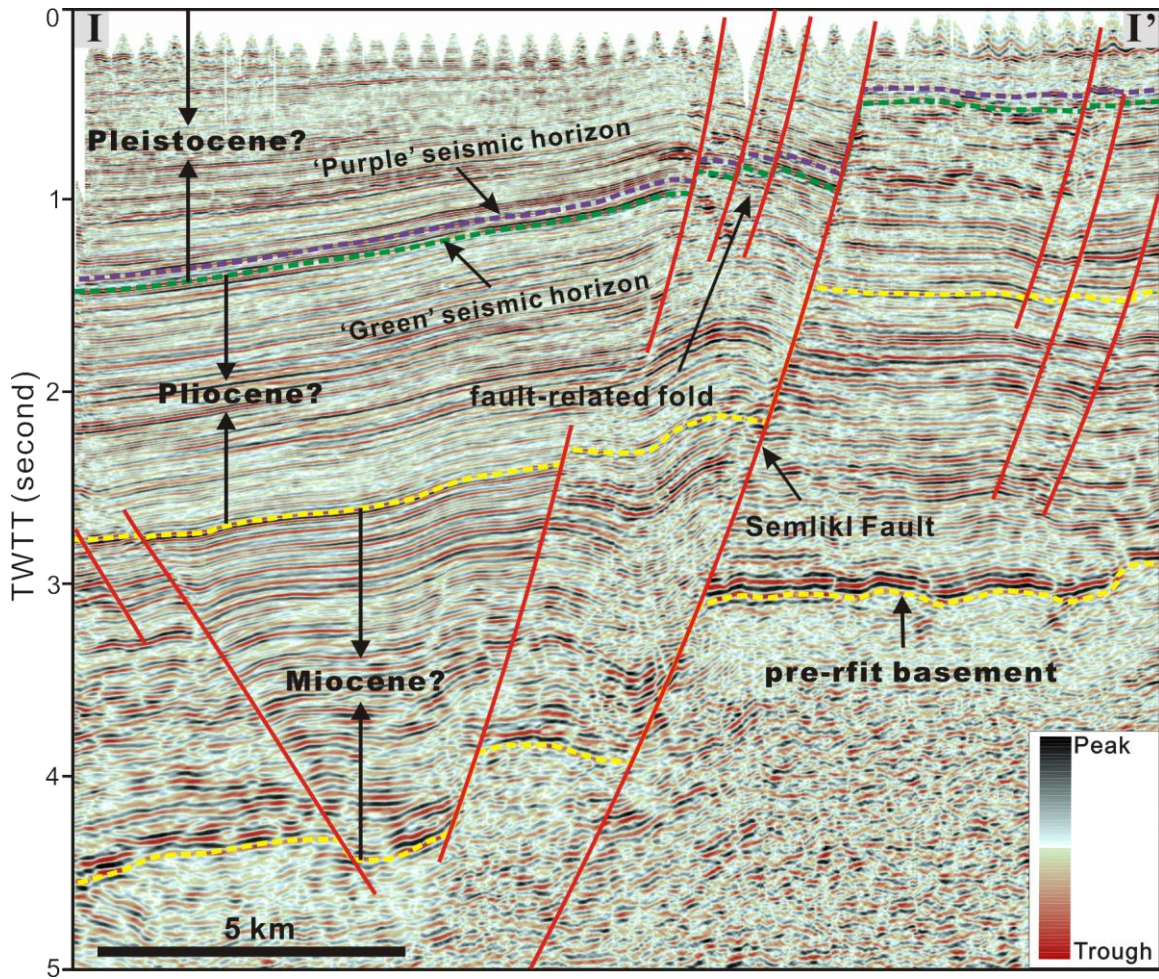


**Figure 1.** Regional topography, structural framework, and drainage systems at the northern end of the Western Rift Valley (modified after McGlue et al., 2006). Fault interpretations are modified from Ebinger (1989), Lardal and Talbot (2002), McGlue et al. (2006), and Karp et al. (2012). The Semliki 3-D seismic survey is located on the southern coast of Lake Albert. Waki-B1 is an exploration well on the northeastern coast of the lake. Offshore 2-D seismic lines are shown in black. The dashed white line on the eastern rift shoulders of Lakes Albert and Edward marks the axis of surface upwarp due to rift-related flank uplift. The blue circles indicate the locations of drainage reversals (Beadle, 1981). KF = Kafu River; KG = Kagera River; KT = Katonga River; MZ = Muzizi River; SR = Semliki River; TY = Tonya River; VN = Victoria Nile; BB = Bunia Border Fault of Lake Albert; BT = Butiaba Fault of Lake Albert; LB = Lubero Border Fault of Lake Edward; NT = N. Toro Bunyoro Fault of Lake Albert; TO = Tonya Fault of Lake Albert; WR = West Ruwenzori Fault; and RM = Ruwenzori Mountains.

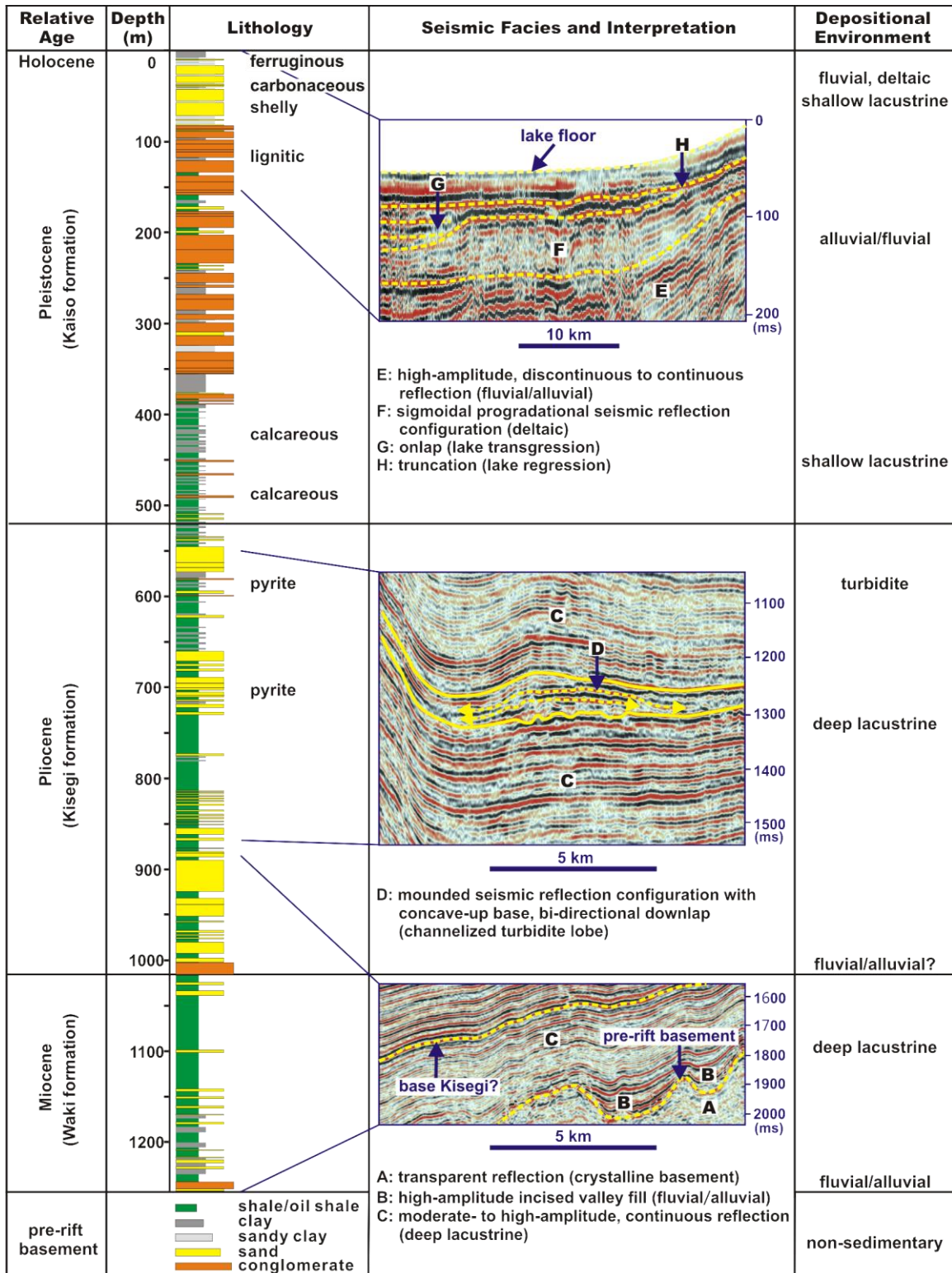




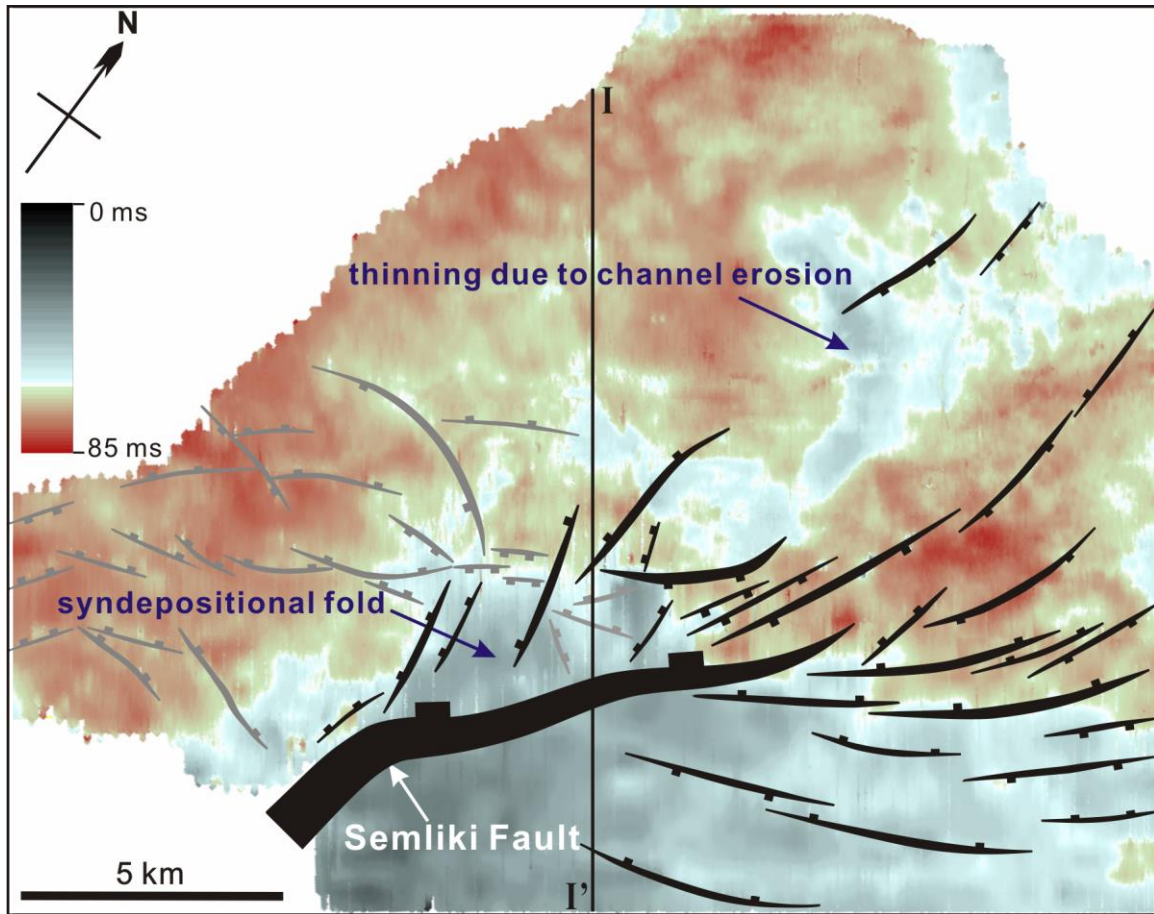
**Figure 2.** A multichannel 2-D seismic profile showing the asymmetric full-graben structure of the Lake Albert Rift and inferred stratigraphic boundaries (after Karp et al., 2012). The red line at surface of the profile indicates regional topography. See the location of the seismic line in Fig.1.



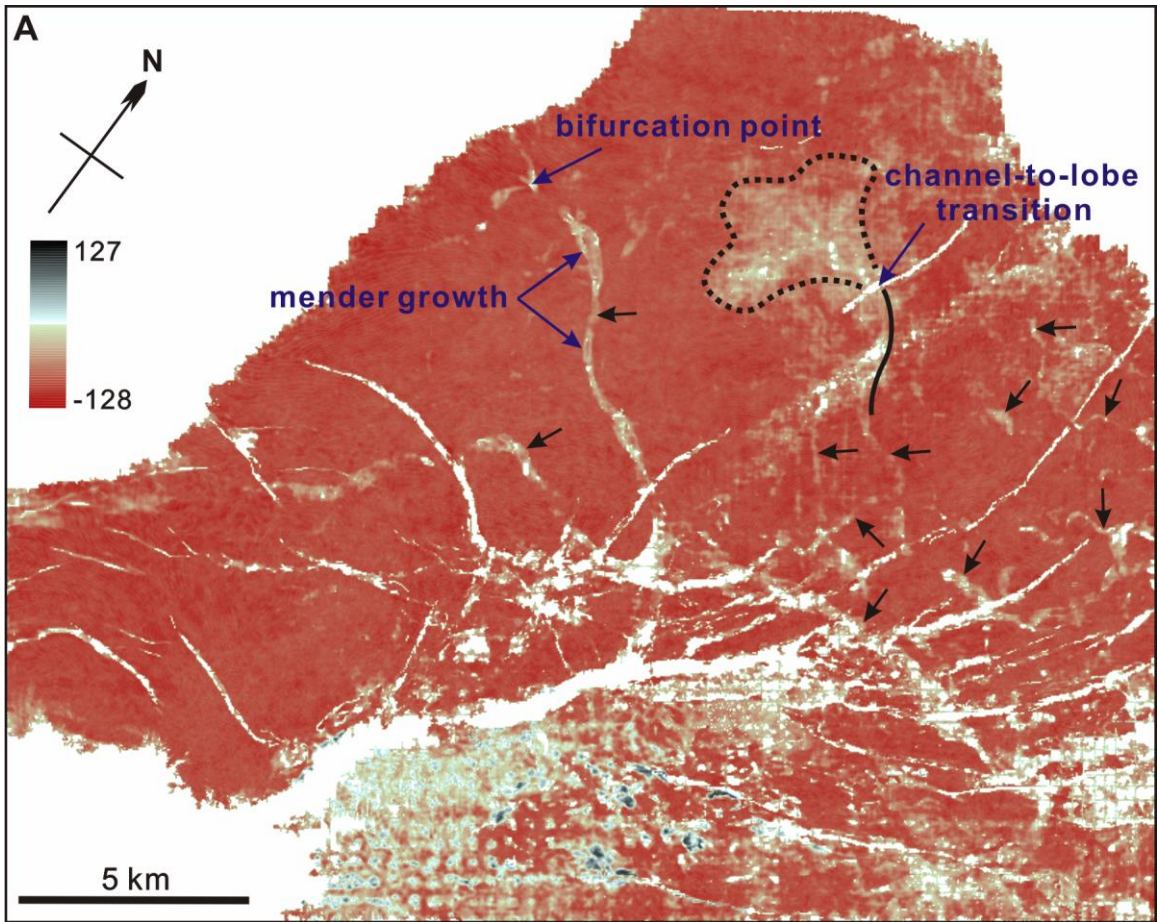
**Figure 3.** Seismic profile I-I' from the Semliki 3-D seismic survey showing major intrabasinal faults and inferred stratigraphic boundaries (by correlation with Karp et al., 2012). Channelized turbidite systems developed during different episodes were observed, and the most extensively distributed ones are associated with the 'Green' and 'Purple' seismic surfaces. See the location of the seismic line in Fig. 5.

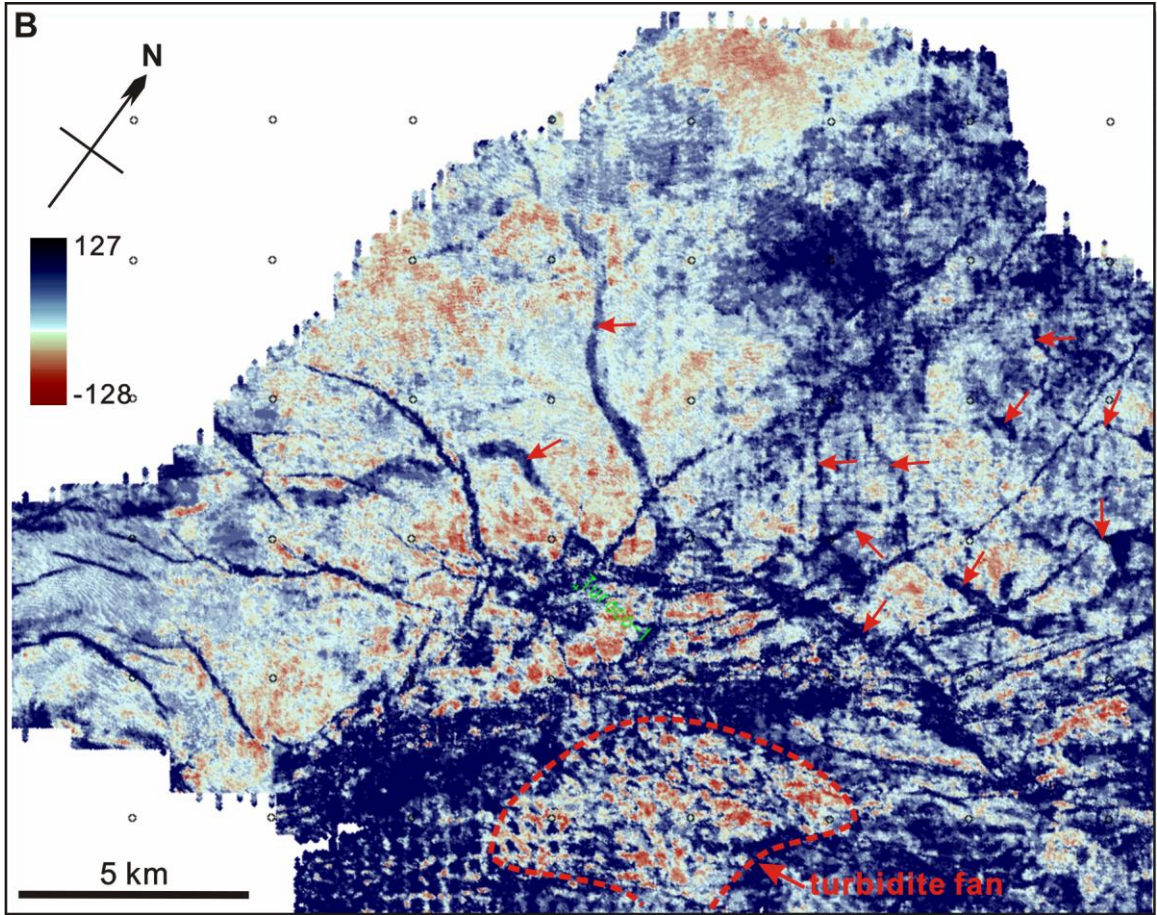


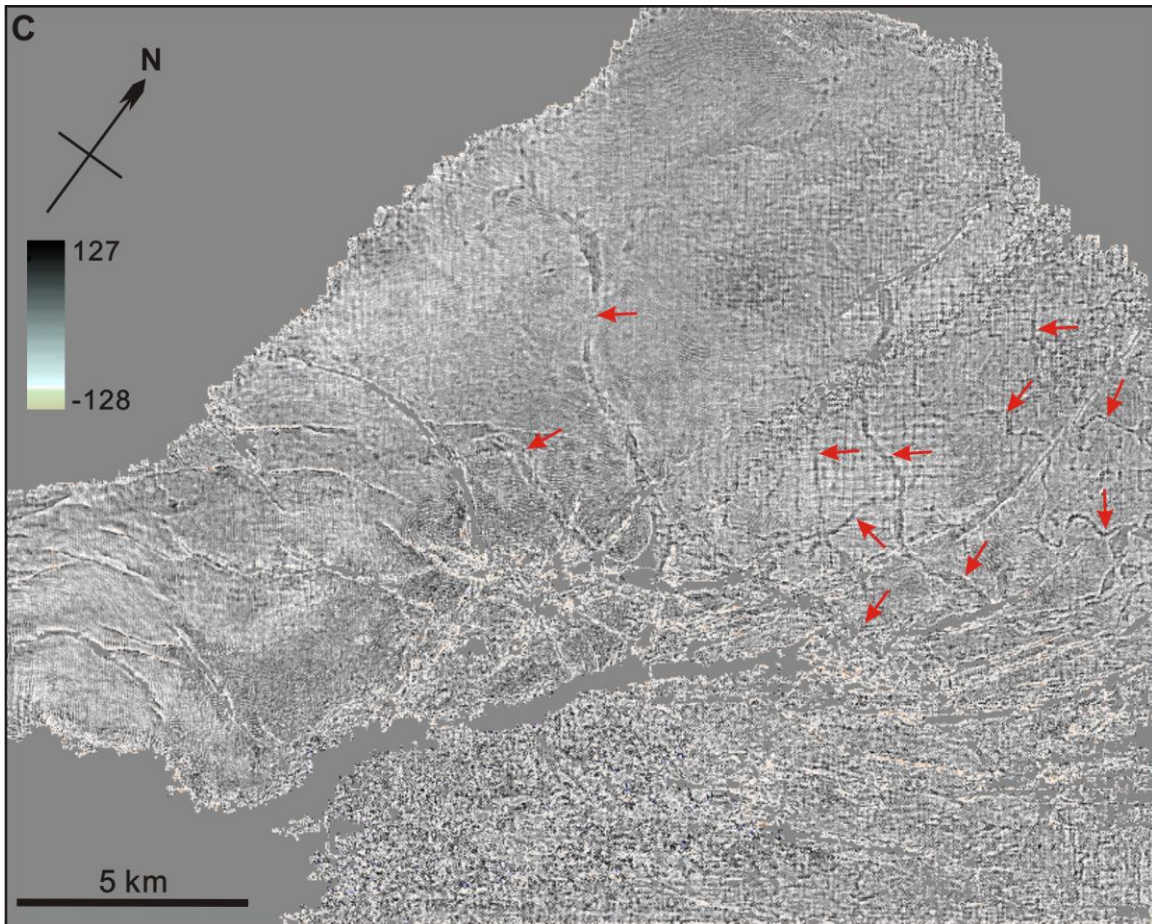
**Figure 4.** Stratigraphy of the Lake Albert rift showing the lithology log of Waki-B1 (after Karp et al., 2012), characteristic seismic facies, and inferred depositional environments.



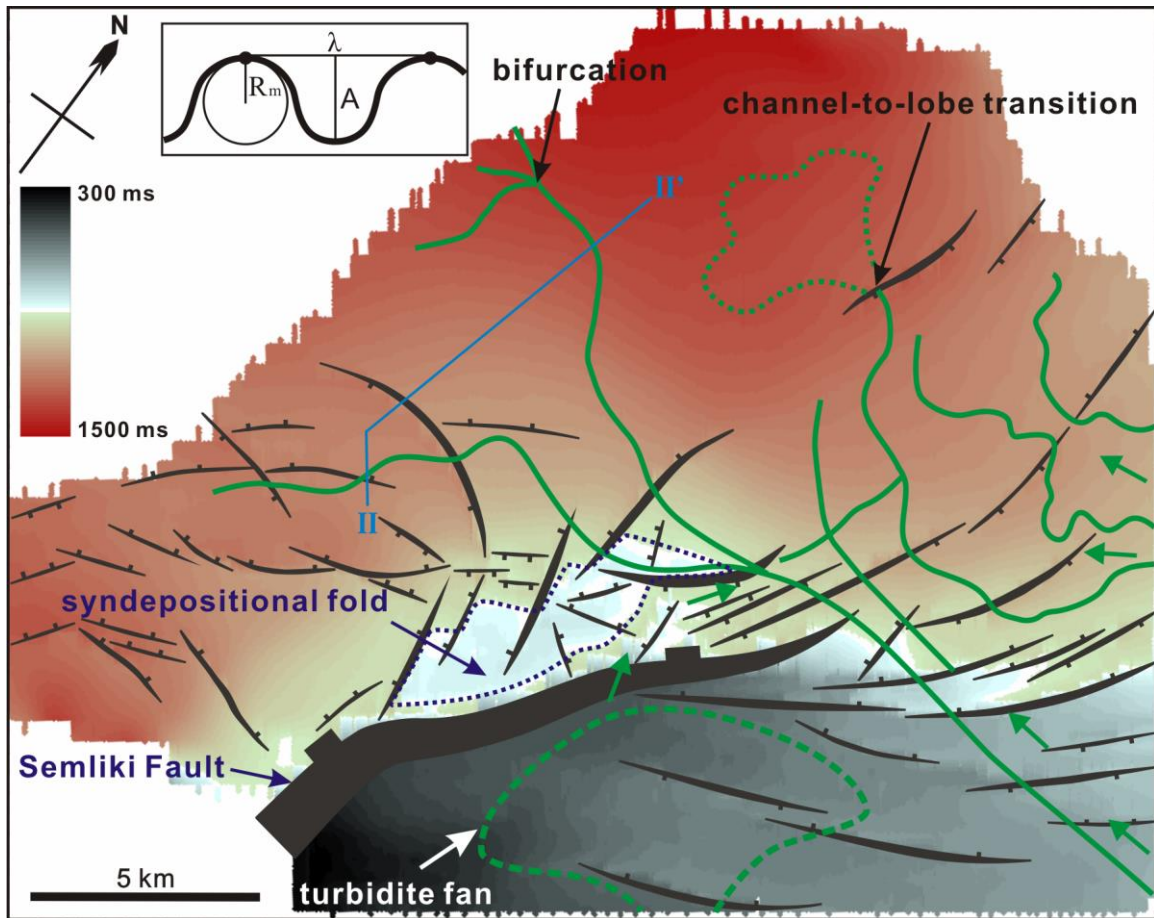
**Figure 5.** Isochron map of the interval between the ‘Green’ and ‘Purple’ seismic surfaces within the Semliki 3-D seismic survey. Intrabasinal faults are displayed with ticks indicating dip directions. The Semliki Fault and the arcuate faults striking subparallel or at low-angle to the Semliki Fault in the eastern and northeastern part of the Semliki 3-D seismic survey are syndepositional (black) to the studied interval. I-I’ is the seismic profile displayed in Fig. 3.





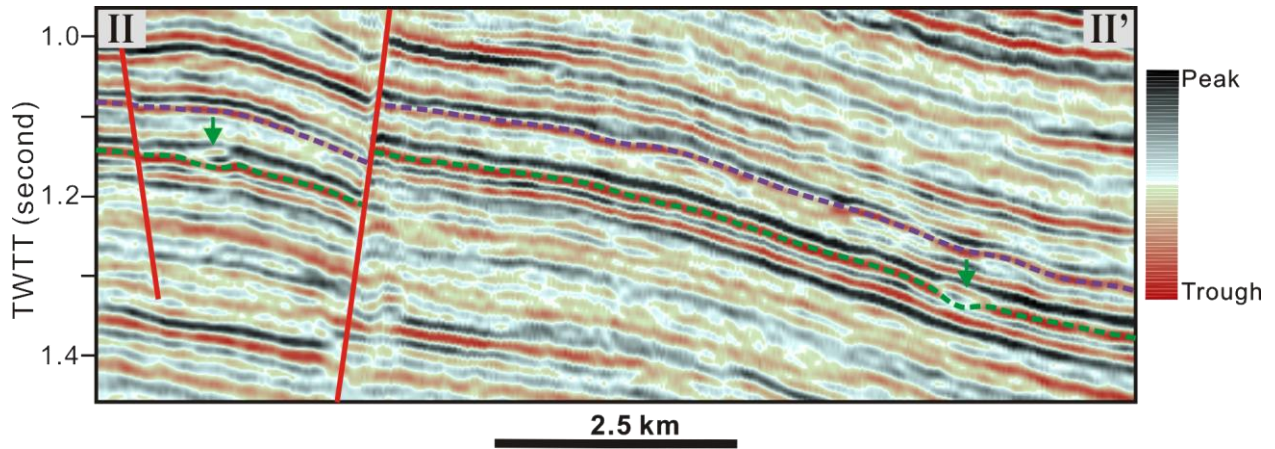


**Figure 6.** Seismic attributes extracted on the ‘Green’ seismic surface, including instantaneous amplitude (A), RMS amplitude (B), and ‘edge detection’ (C), showing the development of turbidite systems of the ‘Green’ depositional unit. Arrows indicate locations of channels. A 40 ms window, i.e. from 20 ms above to 20 ms below the ‘Green’ surface, was used for RMS attribute extraction.

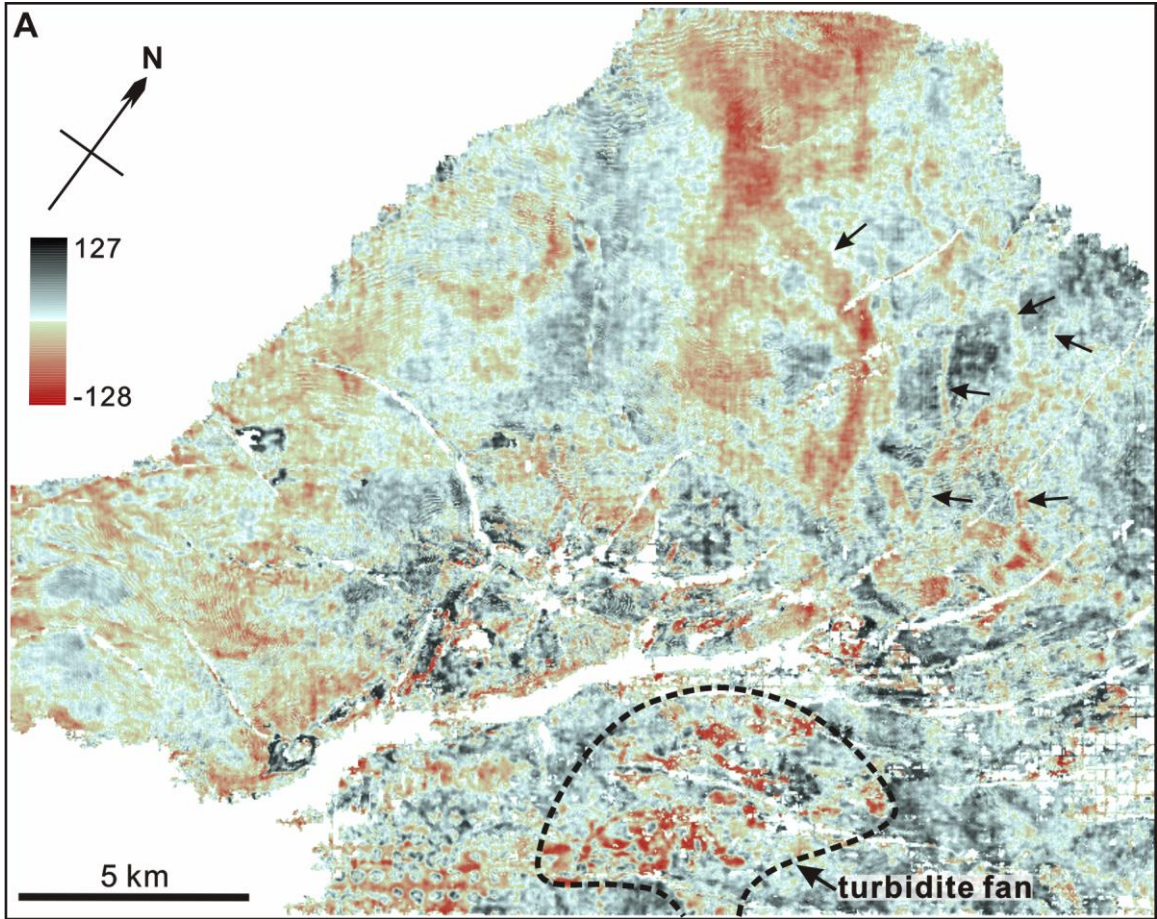


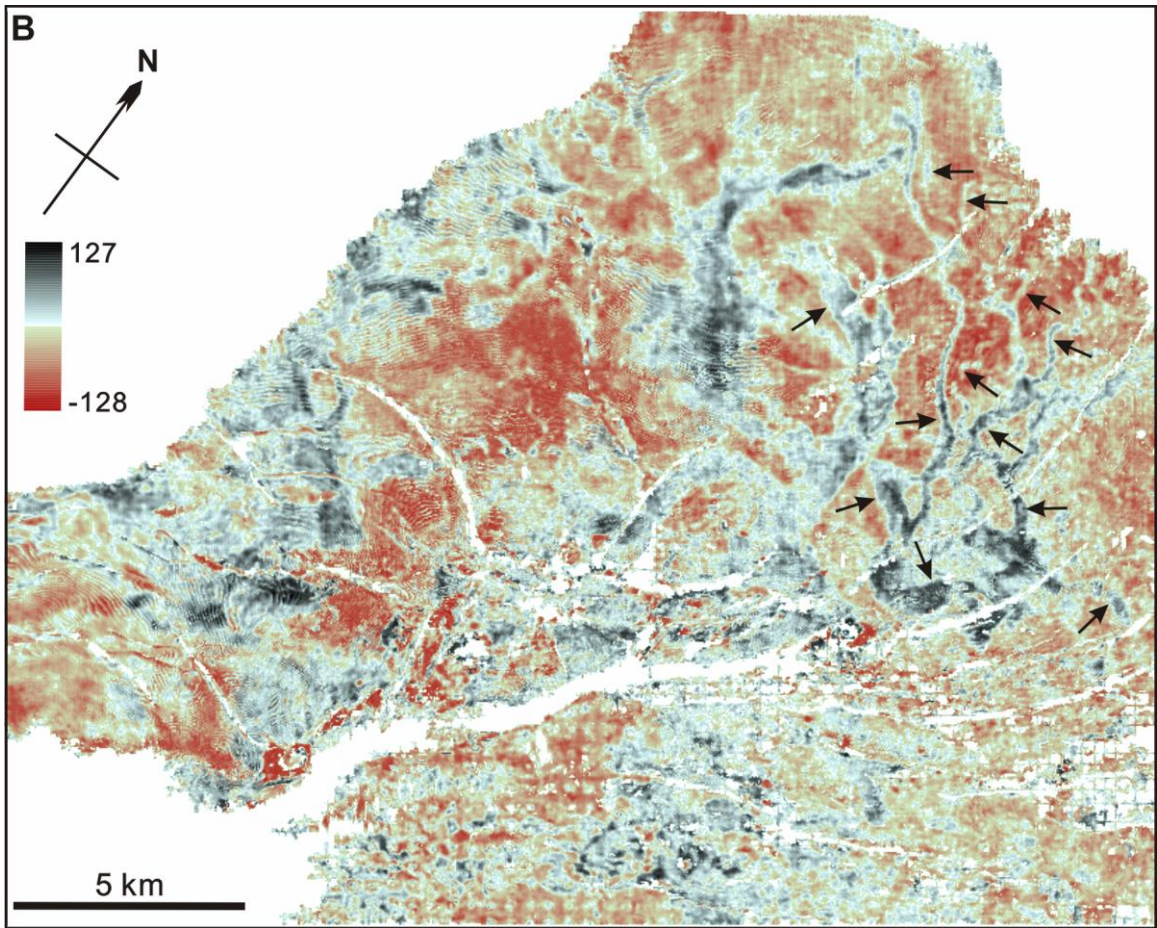
**Figure 7.** Distribution of turbidite systems of the ‘Green’ depositional unit through integrated interpretation of various seismic attributes. TWTT structural map of the ‘Green’ seismic surface is shown by color-filled contours. Intrabasinal faults are shown in black with ticks indicating dip directions. Arrows indicate predicted sediment transport pathways. Inset map defines measurements of meander wavelength ( $\lambda$ ), amplitude ( $A$ ), and radius of curvature ( $R_m$ ). II-II’ is the seismic line displayed in Fig. 8.

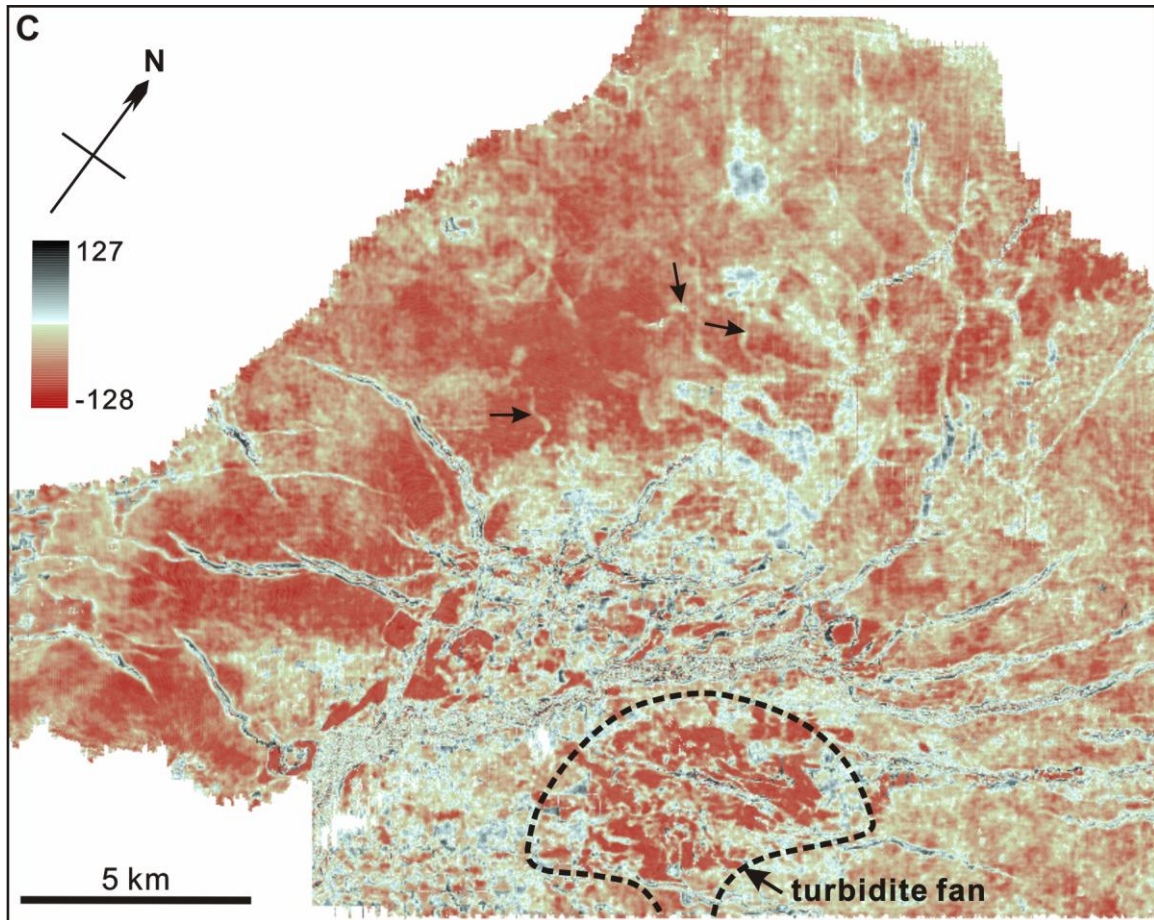




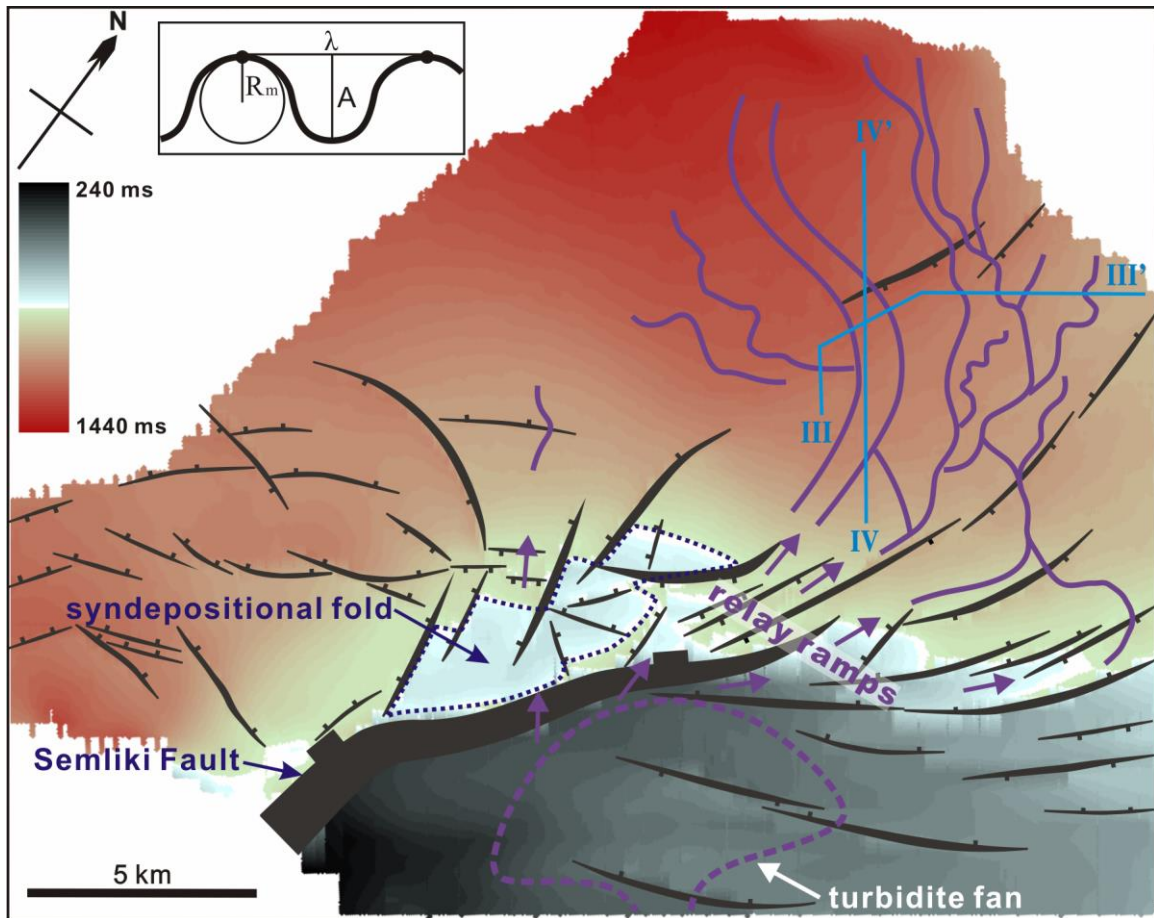
**Figure 8.** Seismic profile II-II' from the Semliki 3-D seismic survey showing the turbidite channels (indicated by arrows) of the 'Green' depositional unit. The channels are characterized by coupled flat channel-top and concave-up channel-base reflections in cross-sectional views. See the location of the seismic line in Fig. 7.



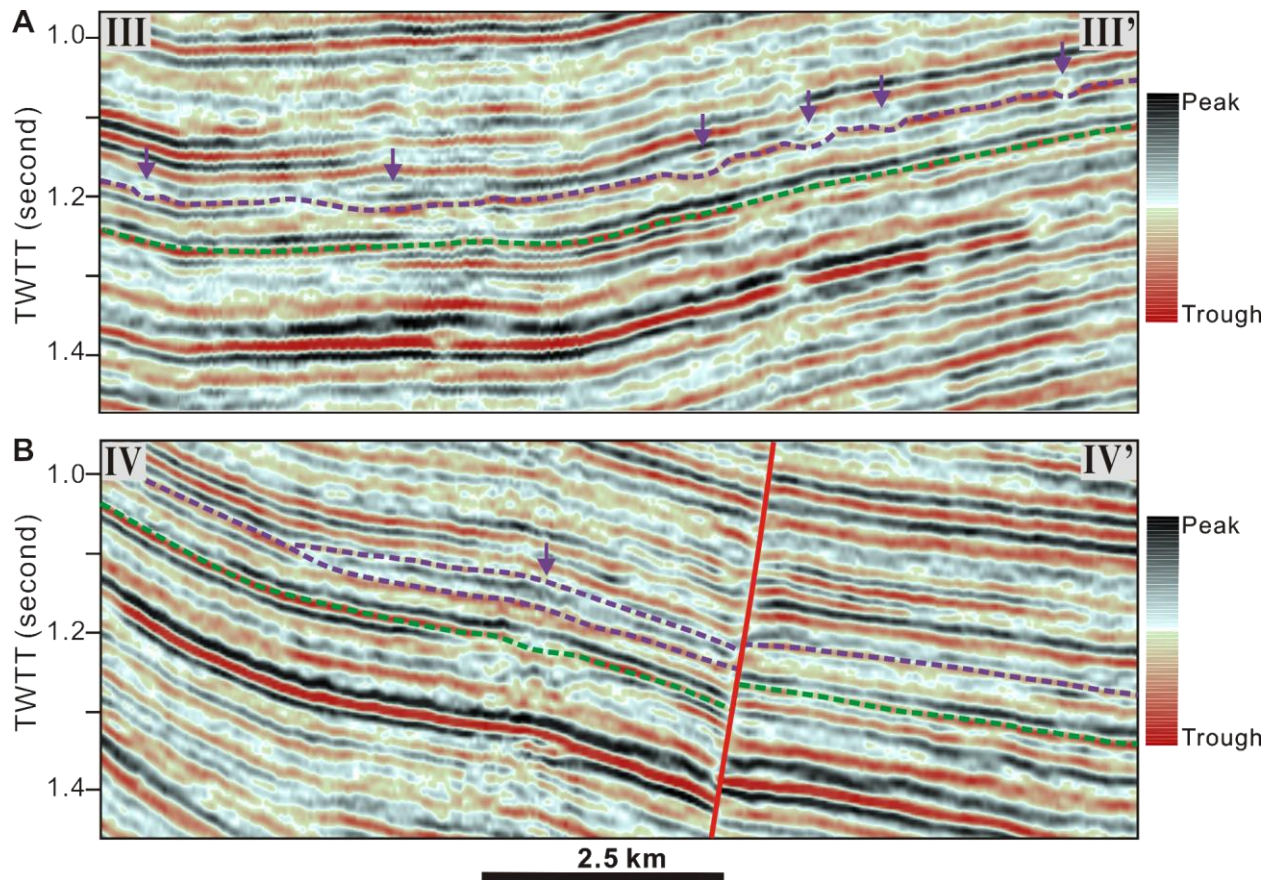




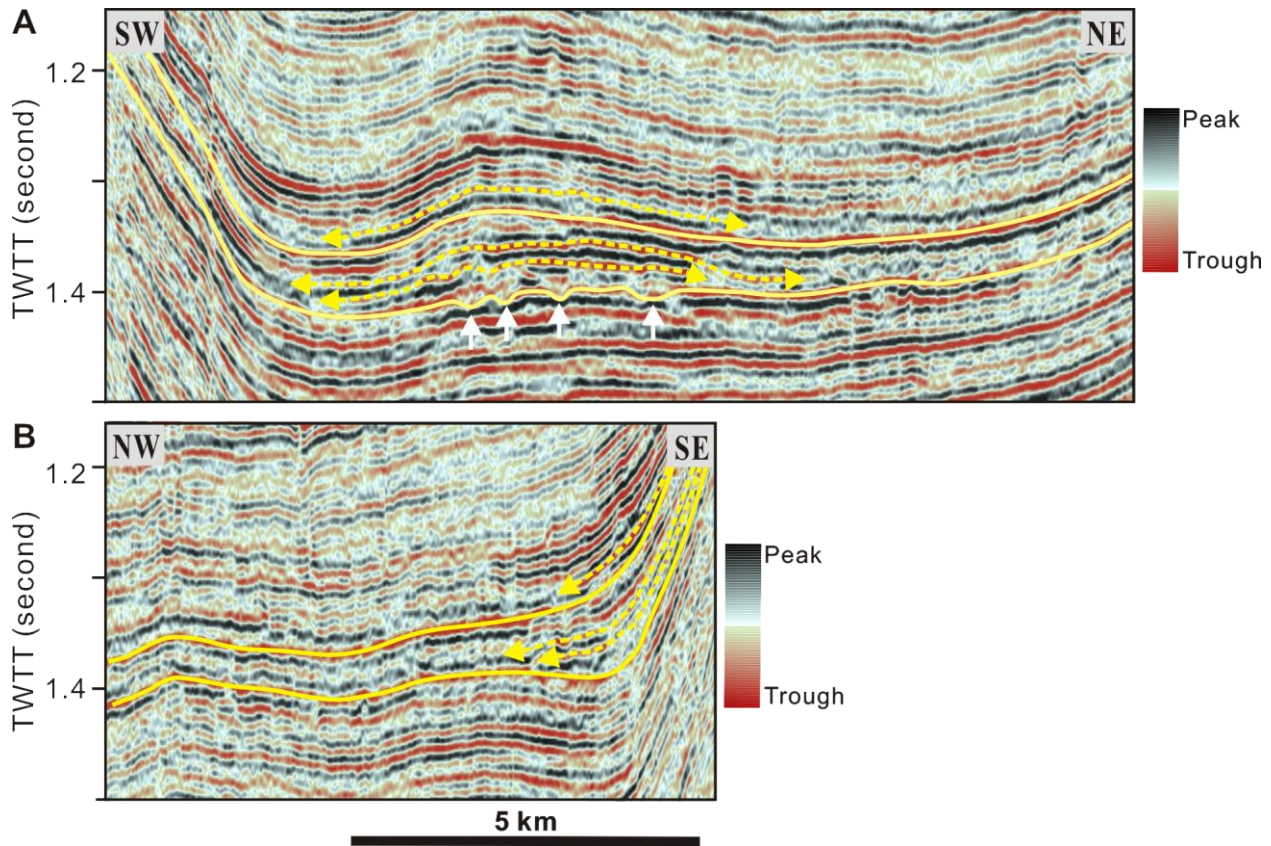
**Figure 9.** Images of horizon slices that are 44 ms (A) and 60 ms (B) above the ‘Green’ seismic surface showing later development of turbidite systems of the ‘Purple’ depositional unit. Arrows indicate locations of channels. The same channels can also be imaged on the stratal slice (C) generated by amplitude extraction on the ‘Purple’ seismic surface; more channels (indicated by arrows) are observed on the stratal slice than on the horizon slices. These channels were probably connected updip to the turbidite fan on the footwall of the Semliki Fault.



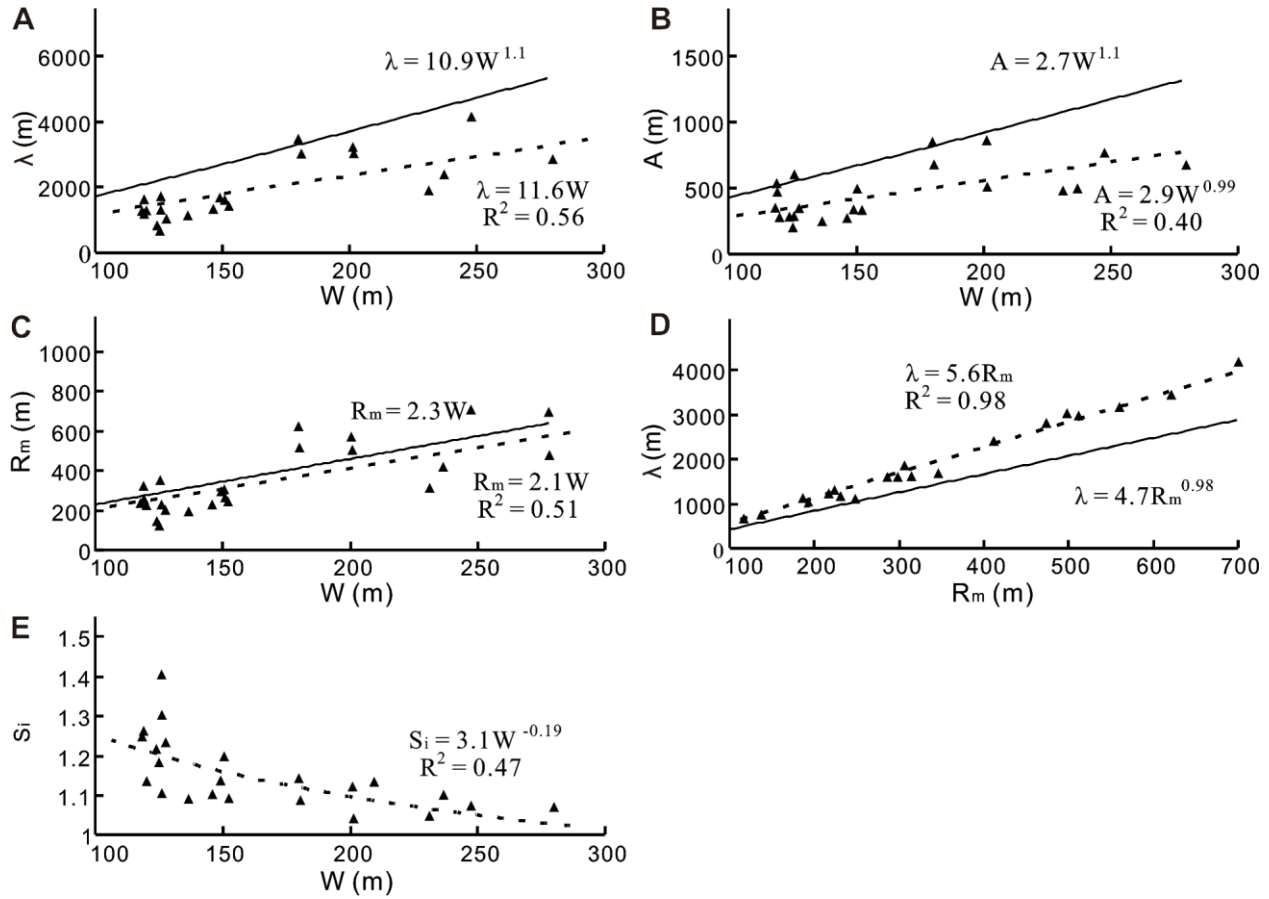
**Figure 10.** Distribution of turbidite systems of the ‘Purple’ depositional unit through integrated interpretation of various seismic attributes. TWTT structural map of the ‘Purple’ seismic surface is shown by color-filled contours. Intrabasinal faults are shown in black with ticks indicating dip directions. Arrows indicate predicted sediment transport pathways. Inset map defines measurements of meander wavelength ( $\lambda$ ), amplitude ( $A$ ), and radius of curvature ( $R_m$ ). III-III’ and IV-IV’ are the seismic lines displayed in Fig. 11.



**Figure 11.** Seismic profiles III-III' (A) and IV-IV' (B) from the Semliki 3-D seismic survey showing turbidite channels (indicated by arrows) of the 'Purple' depositional unit. See the locations of the seismic lines in Fig. 10.

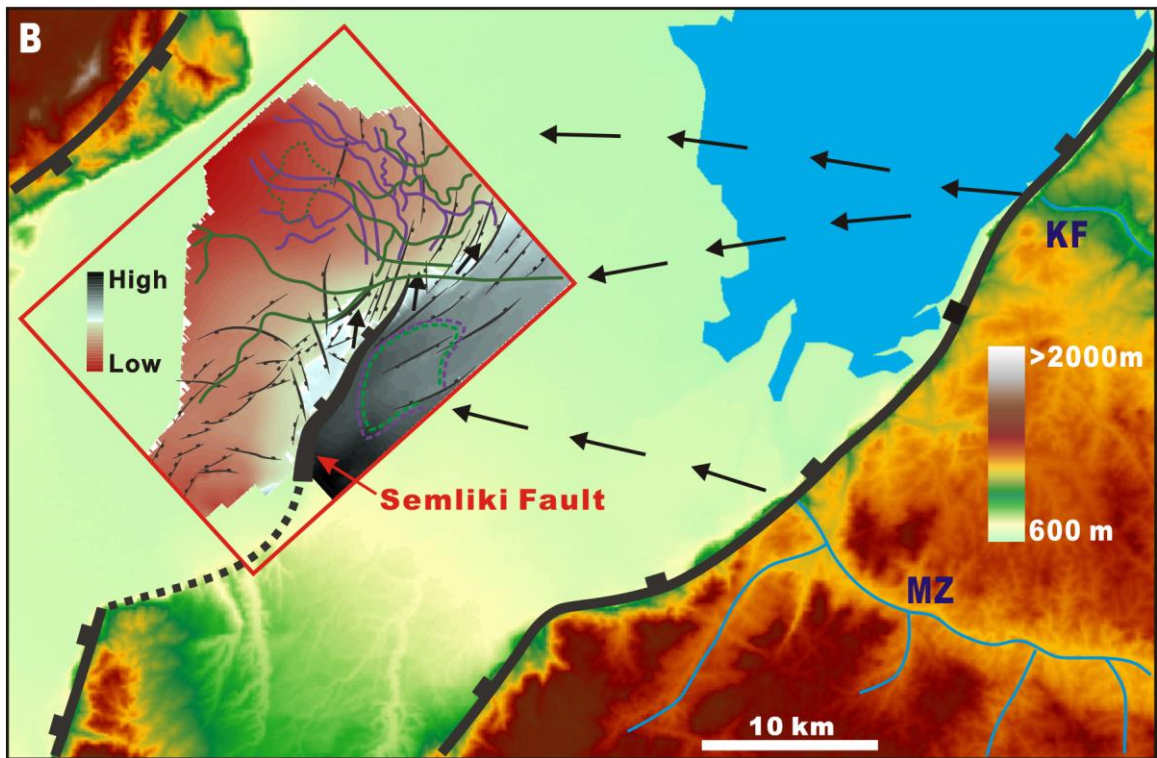
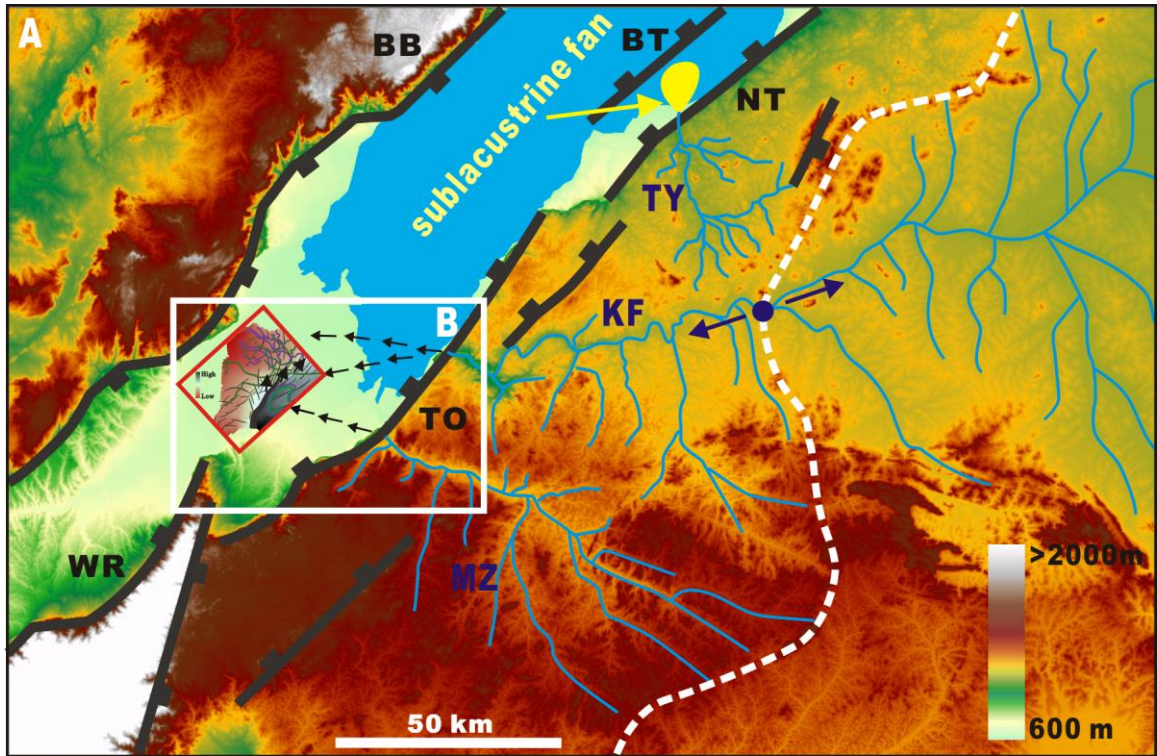


**Figure 12.** Strike (A) and dip (B) seismic lines showing sublacustrine fans deposited along the N. Toro Bunyoro Fault in the northern part of the lake. A channelized (indicated by white arrows) fan is characterized by mounded seismic reflection configuration with bi-directional downlap in the strike direction and progradational reflection configuration in the dip direction. Note the change in the lake-floor topography due to deposition and differential compaction of the fan. See the distribution of the fan in Fig. 14 and the locations of the seismic lines in Fig. 1.

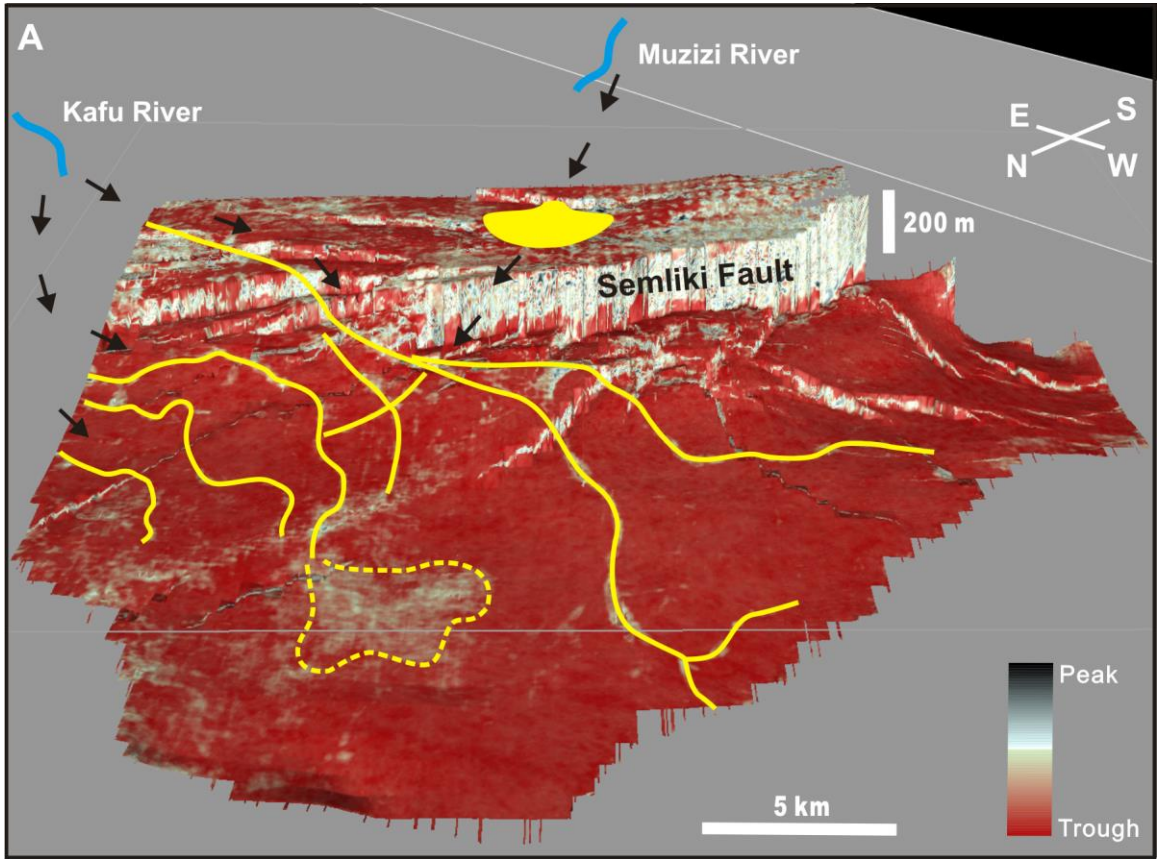


**Figure 13.** (A) - (C): Channel width (W) versus meander wavelength ( $\lambda$ ), amplitude (A), and mean radius of curvature ( $R_m$ ). (D): Mean radius of curvature versus meander wavelength. Dashed lines are regressions of the sublacustrine turbidite channels of the Lake Albert rift, and solid lines are the empirical relationships derived from river channels (Leopold and Wolman, 1957, 1960; Ritter et al., 2002). (E): Channel width versus sinuosity ( $S_i$ ).





**Figure 14.** (A): Correlations between the observed turbidite systems and onshore drainage basins. The dashed white line marks the dividing boundary between the west-flowing and the east-flowing drainages, and the blue circle indicates the location of the Kafu river reversal. Within the Semliki 3-D seismic survey, turbidite systems of the ‘Green’ and ‘Purple’ depositional units connect updip to two different drainage catchments on the eastern rift shoulder. Turbidite systems of the ‘Green’ unit were primarily fed by the Kafu catchment from northeast; later turbidite development of the ‘Purple’ unit was sourced by the Muzizi catchment from southeast. Arrows indicate predicted sediment transport pathways. The burial depth (ms TWTT) of the ‘Green’ seismic surface is displayed as color-filled contours overlapped with the turbidite systems of the two units and intrabasinal structures. See Fig. 1 for the location of the area. Lake Albert; BT = Butiaba Fault of Lake Albert; NT = N. Toro Bunyoro Fault of Lake Albert; TO = Tonya Fault of Lake Albert; and WR = West Ruwenzori Fault. (B): Magnified from Fig. 14A.



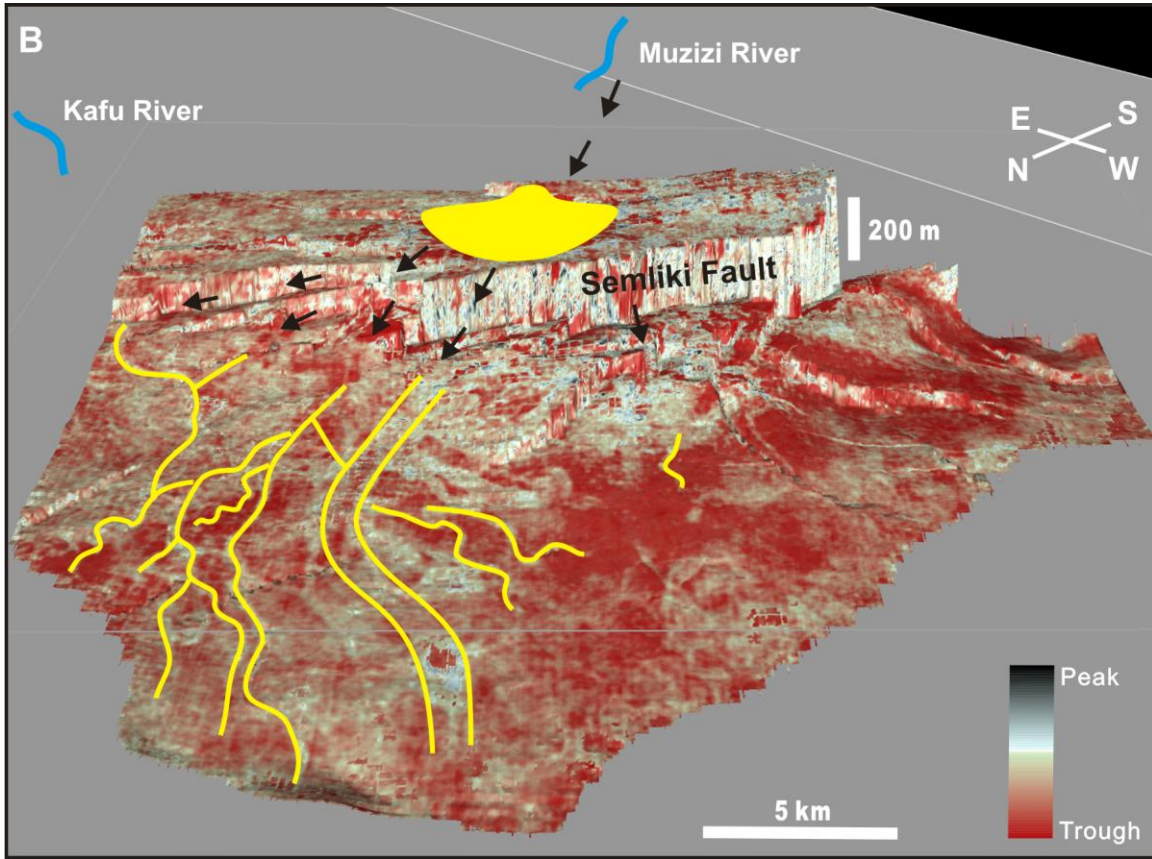


**Figure 15.** 3-D visualization of the ‘Green’ (A) and ‘Purple’ (B) seismic surfaces with observed turbidite channels and fans highlighted in yellow. Arrows indicate predicted sediment dispersal pathways.

**Table 1.** Empirical relationships derived from planform geomorphic parameters of fluvial channels. Modified after Ritter et al. (2002).

Relationship	Source
$\lambda = 10.9W^{1.1}$	Leopold and Wolman (1957, 1960)
$A = 2.7W^{1.1}$	Leopold and Wolman (1957, 1960)
$R_m = 2.3W$	Ritter et al. (2002)
$\lambda = 4.7 R_m^{0.98}$	Leopold and Wolman (1957, 1960)

$\lambda$ : meander wavelength;  $W$ : channel width;  $A$ : meander amplitude; and  $R_m$ : mean radius of curvature.

## **Biographical Data**

Name of Author: Xuewei Zhang

Place of Birth: Beijing, China

Date of Birth: December 6, 1980

### Graduate and Undergraduate Schools Attended:

China University of Geosciences (Beijing), China

Northeast Petroleum University, China

### Degrees Awarded:

M.S., 2006, China University of Geosciences (Beijing), China

B.S., 2003, Northeast Petroleum University, China

### Professional Experience:

Teaching and research assistant, Department of Earth Sciences, Syracuse University, 2009–2014

Exploration geologist, Kerr-McGee China/Anadarko Petroleum Corporation, 2006–2009